

ABSTRACT

Title of dissertation: MEASUREMENTS OF DOPING-DEPENDENT
MICROWAVE NONLINEAR RESPONSE
IN CUPRATE SUPERCONDUCTORS

Dragos Iulian Mircea, Doctor of Philosophy, 2007

Dissertation directed by: Professor Steven M. Anlage
Department of Electrical and Computer Engineering

Near-field microwave techniques have been successfully implemented in the past for the local investigation of magnetic materials and high-temperature superconductors. This dissertation reports on novel phase-sensitive linear- and nonlinear response microwave measurements of magnetic thin films and cuprate superconductors and their interpretation.

The magnetization dynamics of magnetic thin films has been studied experimentally in permalloy and media employed by the magnetic storage industry, and important material characteristics have been extracted from the data: anisotropy field, saturation magnetization, damping constant and exchange energy in good agreement with independent measurements. In magnetic media employed in hard disk drives these quantities cannot be measured effectively by other techniques due to modest signal-to-noise ratio or lack of local capabilities.

The dissertation presents microwave nonlinear measurements in high-temperature superconducting films and a theoretical model to account for the data. Previously,

such studies have been confined to scalar measurements by using spectrum analyzers where only the magnitude of the nonlinear effects was accessible. Therefore, the nonlinear response in the vicinity of the critical temperature has been attributed entirely to the Nonlinear Meissner Effect active in the superconducting state. In the thesis an additional nonlinear mechanism, active in the normal state close to the critical temperature, is proposed and this allows the estimation of the non-equilibrium Cooper pair lifetime in the pseudogap region. Its doping dependence suggests that the Cooper pairs surviving above the critical temperature alter the nonlinear electrodynamics of underdoped materials more significantly than that of their optimally-doped counterparts.

The issue related to the lack of phase information in previous harmonic measurements is resolved by proposing a novel phase-sensitive microwave nonlinear technique which employs a vector network analyzer with harmonic detection capabilities, thus allowing the disentanglement of inductive and resistive nonlinear effects. The experimental data acquired with the new instrument prompted the need for a new model of the near-field nonlinear microwave microscope which treats the nonlinear effects in a finite-frequency, field-based approach as opposed to traditional models which typically use lumped-element approximations in the regime of zero frequency.

MEASUREMENTS OF DOPING-DEPENDENT MICROWAVE
NONLINEAR RESPONSE IN CUPRATE SUPERCONDUCTORS

by

Dragos Iulian Mircea

Dissertation submitted to the Faculty of the Graduate School of the
University of Maryland, College Park in partial fulfillment
of the requirements for the degree of
Doctor of Philosophy
2007

Advisory Committee:

Professor Steven M. Anlage, Chair/Advisor
Professor Thomas Antonsen, Co-Chair
Professor Romel D. Gomez
Professor John Melngailis
Professor Richard Greene

© Copyright by
Dragos Iulian Mircea
2007

All truths are easy to understand once they are discovered; the point is to discover them.

Galileo Galilei

Dedicated to Vasile Ungureanu.

ACKNOWLEDGMENTS

The Ph.D. experience is an amazing adventure, something similar to the mythical stories with heroes who pursue their quest and learn not just how to overcome the obstacles but also how to enjoy the beauty of the world. It is a journey where one discovers oneself. I consider myself very fortunate to have the chance to learn from many people.

Professor Steven M. Anlage has been for me the ideal advisor: very knowledgeable, patient, prudent, enthusiastic. I am very grateful for his support, open mindedness, and wise guidance. He did not show me the solution of a problem, but the ways of approaching it, the path toward finding the answers, thus, preparing me to be an independent thinker and researcher. I am very grateful to Prof. Anlage also for providing a stimulating scientific environment as I have learned from each of his graduate students: Sheng-Chiang Lee, Atif Imtiaz, Sameer Hemaddy, Mike Ricci. Additionally, Hua Xu has prepared for me very high-quality YBCO thin films and I am very grateful for his help.

It is sometimes difficult to realize how much has been learned until the knowledge and skills are tested in the “world out there“. This is a typical motif in the Romanian folk tales where the young prince, after learning from the wisemen living at his father’s royal court, goes in the “world out there“ to “search for his own luck“. For me, such an opportunity arose in the summer of 2005 when I was a summer

intern at Seagate Research, Pittsburgh, PA and I realized the invaluable experience of working under Prof. Anlage's guidance.

During the summers of 2005 and 2006 I worked as a summer intern with Dr. Thomas W. Clinton and I thank him for giving me this opportunity. I am very grateful for his constant, strong interest and support in the project, encouragement and guidance, as well as his critical reading of Chapter 4 of this dissertation. I thank Prof. Carl E. Patton, Dr. T. J. Klemmer and Jason Jury for useful discussions, Alexander Litvinov for performing the B-H hysteresis measurements, Dr. Nils Gokemeijer for laboratory equipment, Labview code and technical assistance, and Dr. Julius Hohlfeld for providing some of the samples. I thank Nadjib Benatmane for working with me in the laboratory, continuing this project, performing measurements on perpendicular media and sharing his results and thoughts with me.

I am very grateful to Prof. Isaak Mayergoyz who served as my academic advisor for almost three years and introduced me into the realm of magnetics. Working in his group has been a rewarding experience for me as I learned Matlab and new experimental techniques from his graduate student Chun Tse, and programming from Andrei Petru and Mihai Dimian.

I would like to express my gratitude to Professor Romel D. Gomez for his teaching of a magnetics class and for serving on my dissertation committee. Appreciation is also due to Professors Thomas Antonsen, Richard Greene and John Melngailis for devoting their time and expertise in serving on my defense committee.

I would like to thank my parents Elena and Alexandru Mircea for their contin-

uous support and especially for encouraging me to follow my passion for the physical sciences. I am very grateful to my father-in-law, Vasile Ungureanu, “the man who died while being alive”, as the Brazilian writer Paulo Coelho wrote in one of his stories, to whom this dissertation is dedicated. I am also grateful to my mother-in-law Aurica Ungureanu. My wife, Camelia Mircea deserves my gratitude for supporting me during this endeavour, for her patience and wisdom.

Finally, I thank God for giving me life and talents, as in the biblical parable, and to my ancestors.

TABLE OF CONTENTS

List of Tables	ix
List of Figures	x
1 The superconducting state	1
1.1 Introduction to superconductivity	1
1.2 High- T_c superconductivity in cuprates	4
1.3 Dissertation Outline	11
2 The microwave response of the superconducting state	15
2.1 Linear electrodynamics of superconductors in BCS theory	15
2.2 Linear electrodynamics of superconductors in the two fluid model . .	16
2.3 Microwave nonlinear response of superconductors	21
2.3.1 Microscopic theories of the nonlinear effects in superconductors	24
2.3.2 Phenomenological theories of the nonlinear effects in superconductors	30
2.4 Prior experimental work on microwave nonlinear effects in superconductors	37
3 The nonlinear near-field microwave microscope	42
3.1 Introduction and motivation	42
3.2 The microwave probe, its near-field and the interaction with the sample	43
3.3 Numerical modeling of the probe-sample electromagnetic interaction .	48
3.4 Experimental apparatus for scalar harmonic measurements	52
3.5 Experimental apparatus for vector harmonic measurements	55
4 Near field microwave microscopy and linear response of magnetization dynamics	60
4.1 Introduction and motivation	60
4.2 Experimental set-up, samples and theoretical background	62
4.3 Theoretical background	68
4.4 Data analysis and discussion	74
4.5 Magnetization dynamics of perpendicular media	79
4.6 Conclusions and future work	85
5 Scalar measurements of the microwave nonlinear response of high- T_c superconductors	88
5.1 Introduction and motivation	88
5.2 Experimental procedure and sample description	90
5.3 Theoretical model of the microwave nonlinear response at T_c	96
5.3.1 Inductive nonlinear response below T_c	97
5.3.2 Resistive nonlinear response above T_c	99
5.4 Data analysis	109

5.5	Discussion	111
5.6	Conclusions	115
6	Vector measurements of the nonlinear response of high- T_c superconductors	117
6.1	Introduction and motivation	117
6.2	Experimental procedure, samples and data	119
6.3	Analytical treatment of the microwave nonlinear microscope	127
6.4	Discussion and Conclusions	140
7	Conclusions and future work	151
7.1	Summary	151
7.2	Future work	152
7.3	Conclusions	154
	Bibliography	165

LIST OF TABLES

5.1	Sample properties: film thickness, critical temperature and spread as determined from AC susceptibility measurements, doping level, in- and out-of-plane coherence length, and the interpolated doping-dependent resistivity parameters.	91
5.2	Fit parameters for the nonlinear resistive component $P_{3f}(T)$ in a series of $\text{YBa}_2\text{Cu}_3\text{O}_{7-\delta}$ thin film samples.	112
6.1	Sample properties: critical temperature and transition width determined from AC susceptibility measurements, the doping level, the difference between the temperatures where the extreme values of the harmonic phase and magnitude occur, and the sample substrate. . . .	124

LIST OF FIGURES

1.1	Tunneling spectra in $\text{Bi}_2\text{Sr}_2\text{CaCu}_2\text{O}_{8+\delta}$ with $T_c = 83$ K. Spectra acquired for $T < 293$ K are offset for clarity. Figure reproduced from Ref.[5]	8
2.1	Temperature- and angular dependence of the nonlinear coefficient $b_\theta(T)$ evaluated numerically for a d-wave superconductor and an s-wave superconductor [26].	28
2.2	Frequency scales describing the electrodynamics of superconductors.	33
2.3	Harmonic phase data acquired on a YBCO coplanar waveguide at 76 K from Ref.[42]	40
3.1	Schematic of the loop probe, sample and the induced microwave surface current (computed numerically with CST-MWS [59]).	44
3.2	Loop probe, the active region where high-density microwave screening currents are induced by the incoming microwave signal and the current wire approximation.	46
3.3	Top view of surface current distribution induced on the sample surface by a coaxial loop probe UT034 placed at $12 \mu\text{m}$ above the sample.	50
3.4	Schematic of the experimental apparatus for the scalar harmonic measurements.	53
3.5	Schematic of the experimental apparatus for the phase-sensitive harmonic measurements.	56
4.1	Schematic of the FMR coax micro-loop probe and the equivalent lumped-element model.	64
4.2	The measurement sequence and the orientation of the probing field h_{MW} with respect to the bias field H_{DC}	65
4.3	The magnitude of the reflection coefficient acquired on a 100 nm thick Py film: measured in the FMR-active and -free configurations.	67
4.4	Real and Imaginary parts of magnetic permeability for the case together with numerical fits	75

4.5	Field dependence of f_{FMR} and linear fit for the two orientations of the DC field. Inset: the $1/f_{FMR}$ dependence of the linewidth Δf , the numerical fit, α extracted from the fit and the approximate α	77
4.6	The imaginary part of the magnetic permeability for Py films of different thickness and the thickness-dependent PSSW frequency	78
4.7	Schematic of the perpendicular magnetic recording	80
4.8	Preliminary measurements on a perpendicular medium	82
4.9	FMR for the SUL of perpendicular disk1	84
4.10	Field dependence of the resonance frequency f_{FMR} and theoretical fit	85
5.1	Experimental data used to evaluate the doping level $7 - \delta$ and the zero-temperature in-plane coherence length $\xi_{ab}(0)$ for the samples discussed in Chapter 5	92
5.2	Experimental data and numerical fit for an underdoped $\text{YBa}_2\text{Cu}_3\text{O}_{6.84}$ thin film	94
5.3	Experimental data and numerical fit for the $\text{YBa}_2\text{Cu}_3\text{O}_{7-\delta}$ thin films	95
5.4	The product $\tau_0 \cdot T_c$ obtained from experimental evaluations of the Cooper pair lifetime $\tau_0^{exp} \cdot T_c$ and the theoretical value $\tau_0^{BCS} \cdot T_c$. . .	113
6.1	Examples of VNA-FOM traces acquired on a YBCO thin film at several temperatures	120
6.2	Phase-sensitive harmonic data acquired on a YBCO thin film	121
6.3	Ratioed magnitude and phase of harmonic voltage $U_{3f}(T)$ acquired on a YBCO thin film (STO039) for several values of input power (8, 6 and 4 dBm)	125
6.4	Schematic of the model of the near-field microwave microscope	130
6.5	Outline of calculation for the nonlinear near-field microwave microscope	134
6.6	The argument of the complex function $(1 + i\sigma_1/\sigma_2)^{-4}$ for the generic temperature dependence of σ_1/σ_2	145
6.7	Phase-sensitive harmonic data acquired on a YBCO thin film (XUH157) represented in the complex plane	146

C.1 Example of scalar harmonic data $P_{3f}(T)$ acquired with a superconducting sample with $T_c^{AC} \approx 91$ K and an inductive writer used as microwave probe 164

LIST OF SYMBOLS

$4\pi M_S$ - saturation magnetization.

\bar{a} , \bar{b} - coefficients governing the temperature dependence of the mean-field component of DC conductivity for cuprates.

$\mathcal{A}(T)$ - temperature-dependent nonlinear coefficient of the real part of conductivity in the normal state.

A_f - vector potential at frequency f generated by the loop probe.

A_1 (A_2) - nonlinear vector potential scale describing the enhancement of σ_1 (the suppression of σ_2) by the external field.

A_{NL} - nonlinear vector potential scale describing the suppression of the superfluid density by the external field.

α - phenomenological damping parameter in Landau-Lifshitz equations.

BCS Bardeen-Cooper-Schrieffer microscopic theory of superconductivity.

$b_\theta(T)$ - temperature- and angular-dependent nonlinear coefficient in the microscopic theory of nonlinear effects in superconductors.

d_0 - sample thickness.

D - exchange constant in magnetic materials.

DS Dahm & Scalapino microscopic treatment of nonlinear effects in superconductors.

δ - doping level in cuprates.

Δf - frequency linewidth in FMR measurements.

ΔH_0 - inhomogeneous broadening in the FMR profiles.

δT_c^{AC} - width of the superconducting-to-normal phase transition evaluated from temperature-dependent AC magnetic susceptibility data.

δT_c - standard deviation of the Gaussian distribution of critical temperatures.

δ_{sk} - microwave skin depth.

e_0 - electron charge ($= 1.6 \cdot 10^{-19}$ C).

E - electric field.

EA easy-axis.

E_{NL} - nonlinear electric field scale characterizing the nonlinear effects in the real part of conductivity in the normal state, associated with the nonlinear current density scale $J_{NL\rho}$.

ϵ - reduced temperature ($= (T - T_c)/T_c$).

f - frequency of the excitation microwave signal.

f_{FMR} - FMR resonance frequency.

FMR Ferromagnetic Resonance.

GE Gorkov & Eliashberg phenomenological treatment of non-stationary electrodynamics of superconductors.

GL Ginzburg-Landau theory of superconductivity.

Γ (Γ_ρ) - figure of merit for the near-field nonlinear microwave microscope evaluated in the superconducting (normal) state.

$\mathbb{G}(\overline{T}_c, \delta T_c)$ - the Gaussian distribution of critical temperatures centered on \overline{T}_c with width δT_c) of the thin film samples.

HA - Hard axis in magnetic materials.

H_{eff} - effective magnetic field.

h_{MW} - microwave excitation field in FMR measurements.

H_c - zero-temperature thermodynamic critical field for superconductors.

H_{co} - coercive field in magnetic materials.

H_{DC} - DC saturating field employed in FMR measurements.

H_K - anisotropy field in magnetic materials.

\hbar - Planck reduced constant ($1.054 \cdot 10^{-34}$ J·s).

i - imaginary unit ($= \sqrt{-1}$).

\tilde{I}_1 (\tilde{I}_2) - current in the primary (secondary) circuit.

J - current density.

J_c - zero-temperature critical current density.

J_{NL} - nonlinear current density scale characterizing the nonlinear effects in the superconducting state.

$J_{NL\rho}$ - nonlinear current density scale characterizing the nonlinear effects (electric-field-dependent real part of conductivity) in the normal state.

$\vec{K} = K_x \hat{x} + K_y \hat{y}$ - screening surface current density induced by the loop probe in the sample.

k - probe-to-sample electromagnetic coupling.

k_B - Boltzmann constant ($= 1.38 \cdot 10^{-23}$ J/K).

k_{SW} - wave vector associated with the spin wave modes.

κ - GL parameter ($= \lambda/\xi$).

l_0 - probe length.

L_0 (L_x) - inductance of the loop probe (probe electric image in the sample).

λ (λ_L) - microwave (London) penetration depth in superconductors.

$\lambda(T, J/A)$ - temperature- and current/field-dependent microwave penetration depth.

$\lambda(T, 0)$ - temperature-dependent microwave penetration depth in the absence of an external perturbation.

λ_{SW} - wavelength associated with the spin wave modes in magnetic materials.

m_e - electron mass ($= 9.1 \cdot 10^{-31}$ kg).

μ_0 (μ_r) - free-space (relative) magnetic permeability.

n - charge carrier density.

NLME - Nonlinear Meissner effect.

n_S (n_n) superfluid (normal fluid) density.

$n_S(T, J/A)$ ($n_n(T, J/A)$) - temperature- and current/field-dependent superfluid (normal) density.

$n_S(T, 0)$ ($n_n(T, 0)$) - temperature-dependent superfluid (normal) density in the absence of an external perturbation.

Ψ - superconducting order parameter in the GL theory.

$P_{3f}(T < T_c, T > T_c)$ - microwave power carried by the 3^{rd} -order harmonic $3f$ cause by the nonlinear effects in the superconducting state and the normal state, respectively.

P_{input} - microwave input power level.

PSSW Perpendicular Standing Spin Wave.

Py Permalloy.

Φ_{3f}^{sample} (Φ_{3f}^{ref}) - phase of the complex harmonic voltage at frequency $3f$ measured at port 2 (**Ref In**) of the VNA-FOM.

$\Psi(T, J/A)$ - temperature- and current/field-dependent order parameter in the GL equations.

$\Psi(T, 0)$ - temperature-dependent order parameter in the GL equations in the absence of an external perturbation.

R_S - real part of surface impedance.

$\rho(T, 0)$ - linear-response resistivity.

S_{11} - complex reflected coefficient.

$S_{11}(f, H_{DC}^\perp)$ ($S_{11}(f, H_{DC}^\parallel)$) - complex reflection coefficient measured with the DC saturating magnetic field applied perpendicular (parallel) to the microwave field h_{MW} .

$\tilde{\sigma}$ - complex conductivity of superconductors ($=\sigma_1 - i\sigma_2$).

σ_1 (σ_2) - real (imaginary) part of the complex conductivity of superconductors.

t - normalized temperature ($= T/T_c$).

T - thermodynamic temperature.

T^* - pseudogap temperature.

T_c - critical temperature indicating the onset of superconductivity.

T_c^{AC} - critical temperature evaluated from temperature-dependent AC magnetic susceptibility data.

$\overline{T_c}$ - mean of the Gaussian distribution of critical temperatures.

τ_0 - time scale of the Cooper pair lifetime in the Time-Dependent Ginzburg-Landau theory.

$\tau^G(\epsilon)$ - temperature-dependent lifetime of Cooper pairs in the normal state evaluated in the regime of Gaussian fluctuations by means of TDGL ($\tau^G(\epsilon) = \tau_0/\epsilon$).

τ_0^{BCS} - lifetime of Cooper pairs in the normal state evaluated by BCS and TDGL.

τ_0^{exp} - lifetime of Cooper pairs in the normal state evaluated from the fit of the experimental data.

τ_{qp} - quasiparticle scattering time.

τ_Δ - relaxation time of the order parameter in the superconducting state.

TDGL - Time-Dependent Ginzburg-Landau theory.

\widetilde{U}_1 (\widetilde{U}_2) - voltage at the terminals of the primary (secondary) circuit.

U_{3f}^{sample} (U_{3f}^{ref}) - complex harmonic voltage at frequency $3f$ incident on port 2

(**Ref In**) of the VNA-FOM.

\widetilde{U}_{refl} (\widetilde{U}_{inc}) - complex reflected (incident) voltage

VNA - Vector Network Analyzer.

χ - magnetic susceptibility.

x_0 - distance from origin to the points where K_y changes sign.

X_S - imaginary part of surface impedance.

$\xi_{ab}(0)$, $\xi_c(0)$ - zero-temperature in- and out-of-plane coherence length for layered materials (cuprates).

YBCO - $\text{YBa}_2\text{Cu}_3\text{O}_{7-\delta}$, high-temperature cuprate superconductor.

ω - angular frequency ($= 2\pi f$).

Ω_0 (Ω_1) - frequency scale determining the dynamics of the order parameter in the superconducting state (transition from Meissner to skin depth screening).

Z_0 - characteristic impedance of coaxial transmission line, ($= 50 \Omega$).

Z_S - complex surface impedance.

Chapter 1

The superconducting state

Know what is in front of your face and
what is hidden from you will be disclosed.

Gospel of Thomas 5

1.1 Introduction to superconductivity

Superconductivity is a very active field of research that has witnessed many revolutions over its one-century of existence. Superconductivity is perhaps the only scientific area where the words *perfect*, *zero* and *infinite* are justified by both theory and experiment. An interesting feature of the evolution of superconductivity as a field of science is that widely-accepted "myths" associated with *perfect*, *zero* and *infinite* have been constantly revised, adjusted and sometimes abandoned. For example, the *perfect* diamagnetism leading to *perfect* exclusion of magnetic fields inside the superconducting volume (*zero* magnetic field) proved to be inaccurate in type II superconductors where the magnetic field penetrates inside the bulk in the form of filaments whereas in type-I superconductors it penetrates within a thin surface layer. Similarly, the idea of *infinite* DC conductivity has been abandoned when it was realized that type-II superconductors in the vortex state exhibit ohmic losses due to the motion of vortices. In addition, at non-zero frequencies the su-

perconductors exhibit finite conductivity, which has been measured with microwave techniques. The existence of the superconducting gap Δ_p , viewed as a characteristic feature of the superconducting state and a required ingredient for macroscopic superconducting properties (persistent currents, Meissner screening, etc.) was questioned with the discovery of gapless superconductors.

Many preconceptions originating from the BCS theory have been constantly revised since the discovery of the heavy-fermion, organic and cuprate superconductors. To name just a few, the symmetry of the order parameter, the Fermi liquid approximation, the collapse of the superconducting gap at the critical temperature T_c , etc. Given this constant turmoil, it became increasingly difficult even to define the essence of superconductivity as most of the "myths" have been gradually demolished.

Since the early days of superconductivity it has been realized that the phenomenon of *zero* DC resistance involves a new thermodynamic phase characterized by a higher order. The model of Gorter and Casimir proposes the existence of two types of charge carriers (electrons) depending on their behavior: superfluid (later called the condensate in the microscopic approaches) behaving in an orderly fashion and the normal fluid exhibiting the properties of the electron gas from normal metals. In this simple two-fluid picture the temperature is the only "knob" that allows the experimentalist to modify the proportions of these two fluids one with respect to the other. The two-fluid model coupled with the Maxwell equations have allowed the London brothers to explain the *perfect* diamagnetism discovered experimentally by Meissner and Ochsenfeld in 1933. The Meissner effect proves that superconductivity

is not simply *perfect* conductivity but a new and distinct thermodynamic state, and the observation that at T_c in the absence of magnetic fields a second-order phase transition takes place has led Ginzburg and Landau to formulate a very successful phenomenological theory of the superconducting state called the Ginzburg-Landau (GL) theory. Within the GL theoretical framework, the superfluid can be suppressed not only by temperature (as was the case in the two-fluid model), but also by an external magnetic field or by a current, as was established experimentally immediately after the discovery of superconductivity. Although very successful in describing the properties of the superconducting state, the phenomenological GL theory was not formulated to address the origins of superconductivity. The answer came in 1957 with the advent of the Bardeen-Cooper-Schrieffer (BCS) theory which approached superconductivity at the microscopic level.

The BCS theory has enjoyed a tremendous success, its predictions have been confirmed by experiment and in some limiting cases its equations could be reduced to the London theory. The re-formulation of BCS in the language of Green functions has expanded its area of applicability to situations where the superfluid density n_S varies in space, to the case of strong-coupling and gapless superconductivity. By using BCS in the language of Green functions, Gorkov proved that the phenomenological GL theory is a limiting case of the microscopic BCS theory at temperatures close to the critical one T_c and together with Eliashberg formulated the time-dependent GL (TDGL) equations which will be re-visited in chapter 2. Despite its success, BCS theory poses mathematical difficulties which become obvious when finite-frequency external fields suppress superconductivity, leading to nonlinear effects, the subject

of this thesis. In such situations, phenomenological approaches, such as GL and TDGL, provide a more manageable mathematical formalism.

1.2 High- T_c superconductivity in cuprates

As described previously, the microscopic BCS and the phenomenological GL theories and their generalizations have provided a complete framework to understand superconductivity until the advent of high-temperature superconductors (HTS) in 1986. The discovery of new materials with critical temperatures above that of liquid nitrogen renewed the interest in superconductivity for two main reasons: the scientific aspect of the problem and the possibility of synthesizing materials with T_c close to room temperature, and the prospect of commercial applications involving superconducting elements that are cooled down with low-cost liquid nitrogen.

The highest critical temperatures have been obtained in cuprate materials: $T_c = 134$ K in $\text{HgBa}_2\text{Ca}_2\text{Cu}_3\text{O}_{8+\delta}$, $T_c = 95$ K in $\text{Bi}_2\text{Sr}_2\text{CaCu}_2\text{O}_{8+\delta}$, $T_c = 93$ K in $\text{YBa}_2\text{Cu}_3\text{O}_{7-\delta}$. The structural pattern common to all cuprate materials is the orthorhombic or tetragonal cell containing Cu_2O planes oriented perpendicular to the c crystalline direction and separated by layers of other atoms (Ba, La, O, \dots). This structural feature and the empirical observation that a larger number of CuO_2 planes per unit cell results in higher T_c have suggested that the seat of superconductivity are the Cu_2O planes, while the other layers act as charge reservoirs. This statement was proposed in the early days of high-temperature superconductivity and it is known as Anderson's first dogma [1]. The layered structure and

the weak coupling between the CuO_2 planes leads to strongly anisotropic properties manifested in conductivity, coherence lengths, etc. (i.e. poor conduction in the c direction compared to that along a or b directions, very different in-plane and out-of-plane coherence length, $\xi_c \ll \xi_{ab}$, [2]).

The cuprate materials are obtained by doping the so-called parent compound, which is an insulator with the Cu spins aligned in an antiferromagnetic state, below the Néel temperature T_N . Inelastic neutron- and Raman scattering experiments have shown that above T_N the correlations among the Cu spins are essentially two-dimensional [3]. In the parent compound the CuO_2 planes are made up of Cu^{2+} and O^{2-} so that the CuO_2 planes are negatively charged (a net charge of $-2e_0$ per unit cell, where e_0 is the elementary charge) which suggests that the interleaved layers must be positive to enforce the electrical neutral state [2]). By doping, the parent insulator becomes metallic and below a certain temperature T_c , superconducting. The dependence of the critical temperature on the doping concentration $T_c(p)$ represents the phase diagram and has roughly the same main features for all cuprates.

Depending on the doping element, cuprates can be hole- or electron-doped with significantly different phase diagrams and different physical properties. The present study is confined to hole-doped $\text{YBa}_2\text{Cu}_3\text{O}_{7-\delta}$ (YBCO) thin films fabricated by Pulsed-Laser Deposition with subsequent annealing in oxygen atmosphere whose parent compound has $\delta = 1$. The phase diagram of hole-doped cuprates shows that superconductivity occurs always in the vicinity of the antiferromagnetic phase and suggests that superconductivity and antiferromagnetism may have something

in common; the electron-electron pairing could be mediated by spin fluctuations, as opposed to low-temperature superconductors where the pairing is due to exchange of lattice vibration quanta (phonons) between the two paired electrons. In hole-doped YBCO the critical temperature T_c depends roughly quadratically on the hole concentration p according to the law: $T_c/T_c^{optimal} = 1 - 82.6(p - 0.16)^2$ [4] (see Fig.5.4 for a representation of the cuprate phase diagram). $T_c^{optimal}$ represents the maximum critical temperature obtained in YBCO (≈ 93 K) for $p = 0.16$ and this is commonly-labeled *optimally-doped*. For $p < 0.16$ and $p > 0.16$ YBCO is under- and over-doped respectively. Annealing in oxygen atmosphere, as employed for the samples used in the present study, results in oxygen-deficient YBCO samples (underdoped) with critical temperatures below 93 K.

Since cuprates are obtained by doping the parent insulator, they have a lower carrier concentration n than ordinary metals. As a result, the charge carriers are less screened than in metals, the Coulomb electrostatic repulsion is stronger and consequently the mechanism of electron pairing is different that in low-temperature superconductors. In addition, the low carrier concentration modifies the physics of the normal-to-superconducting phase transition with consequences that will be discussed later in this chapter. Since in underdoped cuprates n is even more reduced than in their optimally-doped counterparts, the above deviations from BCS superconductors should be even more pronounced. For this reason the investigation of hole-doped underdoped cuprates is a very active area of research both theoretically and experimentally.

A striking feature observed especially in oxygen-deficient hole-doped cuprates

is the existence of an energy gap in the quasiparticle density of states observed for temperatures between T_c and a certain temperature $T^* > T_c$. Due to the similar symmetry of this gap with that in the superconducting state and the absence of a phase transition at T^* , the normal state gap has been labeled a *pseudogap*. Another reason for this nomenclature is the disagreement of T^* estimates from different types of experiments (infrared conductivity, neutron scattering, transport properties, Raman spectroscopy, specific heat, thermoelectric power) as opposed to the general consistency in estimations of the superconducting gap. However, within the same experimental framework T^* depends on the material and doping level as discussed in the following paragraphs where tunneling data from the literature are briefly reviewed.

Tunneling measurements have been successfully used to prove the existence of the superconducting gap in low- T_c materials due to its sensitivity to the charge carrier density of states below (negative bias) and above (positive bias) the Fermi level. Essentially, the tunneling spectroscopy on superconducting samples allows one to measure directly the energy required to break a Cooper pair, irrespective of the presence or absence of macroscopic phase coherence among the Cooper pairs. The energy gap in the quasiparticle excitation spectrum shows up as a characteristic feature at zero bias $V = 0$ and by using an appropriate model for the superconducting state one can estimate the Cooper pair binding energy Δ_p . An STM-assisted tunneling experiment (characterized by a very high spatial resolution on the order of 0.1 nm and a sensitivity on the order of $k_B T$) carried out by Renner and co-workers reveal the existence of an energy gap below and above the critical

temperature $T_c = 83$ K in the hole-doped cuprate $\text{Bi}_2\text{Sr}_2\text{CaCu}_2\text{O}_{8+\delta}$ (Bi2212) single crystals (see Fig. 1.1) [5].

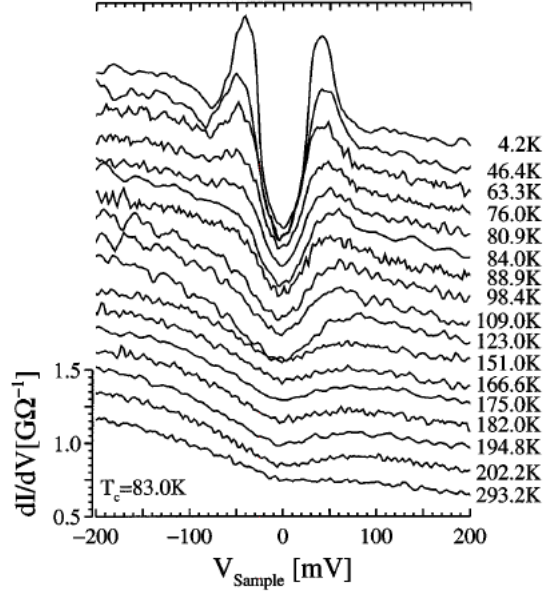


Figure 1.1: Tunneling spectra in $\text{Bi}_2\text{Sr}_2\text{CaCu}_2\text{O}_{8+\delta}$ with $T_c = 83$ K. Spectra acquired for $T < 293$ K are offset for clarity. Figure reproduced from Ref.[5]

One of the observations of Renner and co-workers is that the tunneling spectra acquired on samples with different doping levels are consistent with a d-wave symmetry of the order parameter in the superconducting state. A striking feature of the data reproduced in Fig. 1.1 is that the energy gap observed below T_c (the superconducting gap) is roughly temperature independent up to T_c and it does not close at this temperature as one would expect for a BCS superconductor: it seems that the superconducting gap evolves into the pseudogap at T_c . Since tunneling experiments measure *only* the energy $2\Delta_p$ required to break a Cooper pair, one can think that the onset of the macroscopic superconducting properties (zero DC

resistance, Meissner effect, etc.) at T_c is governed not only by the electron-electron binding energy (roughly given by Δ_p) as is the case in the BCS superconductors, but by another energy scale Δ_c . This energy scale has been associated with the establishment of macroscopic phase coherence between the paired charge carriers [6] since the superconducting state requires paired carriers as well as macroscopic phase coherence among the pairs. The phenomenological analysis from Ref. [5] (the only possible analysis since a model for the gap function and the density of states in cuprates is not yet available) shows that the gap magnitude Δ_p increases in the underdoped samples despite the suppression of T_c .

The question of measuring the other energy scale governing T_c , Δ_c associated with the macroscopic phase coherence, has been addressed by Deutscher [7] by analyzing normal-to-superconducting tunneling measurements. Andreev reflection and the Josephson effect are both manifestations of macroscopic quantum coherence [7], so tunneling measurements in a normal-to-superconductor configuration can be used as a tool to investigate the energy scale Δ_c . Such tunneling experiments on hole-doped cuprates with various doping levels from underdoped to overdoped have shown that the two energy scales converge in overdoped materials indicating BCS-like behavior, and diverge in the underdoped region of the phase diagram [7]. In agreement with the results of Ref.[5], Δ_p exceeds Δ_c in underdoped materials suggesting that underdoped cuprates deviate significantly from the BCS behavior.

Another experimental framework that has provided non-BCS signatures is the Nernst effect in hole-doped cuprates. The **Nernst effect** consists of the appearance of a transverse electric field in response to a temperature gradient in the presence

of a perpendicular magnetic field under open circuit conditions [8]. In the superconducting state, the perpendicular magnetic field drives the sample into the mixed state and the resulting vortices move against the temperature gradient leading to a significant electric field transverse to the flow. In a conventional BCS picture, by warming up the sample above its critical temperature the vortices are destroyed and the Nernst voltage, carrying information about the quasiparticles, becomes very small. This conventional picture is not valid in hole-doped cuprates as shown by the data of Ong *et al.*, who found an unusual high Nernst voltage above T_c [9]. The deviations from the BCS-expected behavior have been interpreted as evidence for the existence of vortices (or "vortex-like excitations" as other authors have labeled the microscopic elements responsible for the observed effect [10]) above T_c [9]. Another line of thought attributed the strong Nernst signal above T_c to the superconducting fluctuations and quantitative evaluations showed that data in optimally- and overdoped $\text{La}_{2-x}\text{Sr}_x\text{CuO}_4$ (LSCO) can be explained within this theoretical framework. In order to reproduce experimental data acquired with underdoped samples, the theoretical model required suppressed T_c values as compared to the mean-field ones. An alternative scenario has been proposed by Tan and Levin who showed that pre-formed Cooper pairs could be responsible for the anomalous Nernst effect observed by Ong and co-workers [11].

1.3 Dissertation Outline

The thesis is organized based on a chronological progress that has been achieved during this project of investigating microwave nonlinear effects in cuprate thin films. Chapter 1 introduces the fundamental properties of the superconducting state with emphasis on the properties of high-temperature superconductors that make them different from their low-temperature counterparts. Results from tunneling and Nernst effect experiments are briefly reviewed where it is shown that the cuprates behave in a non-BCS fashion. At the end of Chapter 1 an outline of the dissertation is given.

Chapter 2 discusses the linear- and nonlinear electrodynamics of the superconducting state in more detail. The main features of the microscopic BCS theory are presented followed by a simple and mathematically accessible description in a two-fluid model based on the phenomenological picture of the London brothers. The theoretical treatments of the microwave nonlinear effects are reviewed in the context of microscopic BCS-based theories and the phenomenological approaches constructed from the GL theory and its finite-frequency extension TDGL. Chapter 2 ends with a literature review of experimental work concerning the nonlinear effects in low- and high-temperature superconductors. It will be shown that temperature-dependent phase-sensitive harmonic measurements at microwave frequencies have not been performed until now, despite the availability of commercial Large-Signal Network Analyzers.

Since the experimental set-ups employed for these investigations have some common features, Chapter 3 is dedicated to their detailed description. The mi-

crowave probes and their electromagnetic interaction with the sample under investigation is discussed both at qualitative and quantitative level. Various physical quantities that are relevant for the evaluations from Chapter 5 are calculated. Next, the experimental apparatus used for the scalar- and vector harmonic measurements reported in Chapter 5 and 6 are presented.

Chapter 4 presents a successful implementation of the near-field microwave microscopy in the area of magnetization dynamics in magnetic materials. Although these are linear-response measurements, this work has revealed aspects that are useful for the improvement of the nonlinear version of this experiment. In the first stage of this work, the Ferromagnetic Resonance (FMR) and spin wave dynamics have been investigated in permalloy thin films. After validating the technique on permalloy, several disks employed in Perpendicular Magnetic Recording (PMR) have been FMR-characterized and signatures of the Soft Underlayer (SUL) have been detected. Currently, work is in progress at Seagate Research, Pittsburgh, PA, to extend the applicability of the near-field microwave microscope to the investigation of magnetically hard materials that make up the storage layer of PMR disks.

A more complete model of third harmonic power data $P_{3f}(T)$ acquired previously on $\text{YBa}_2\text{Cu}_3\text{O}_{7-\delta}$ (YBCO) thin films by means of near-field microwave microscopy is the subject of Chapter 5. It is shown that not only inductive nonlinear effects below T_c cause the peak of $P_{3f}(T)$ at T_c , as was considered before, but also resistive nonlinear effects, which are active above T_c . Previously, only the inductive nonlinear effects were considered to model the harmonic data acquired with the microwave microscope, with model-data disagreements in underdoped samples

[45]. The model of Gaussian superconducting fluctuations proposed by Mishonov and co-workers [29] is re-formulated in the language of superconducting nonlinear effects adopted in microscopic BCS-like [26, 27] and phenomenological models [41, 43], where the strength of nonlinear effects is described in terms of a nonlinear current density scale.

The model proposed in Chapter 5 assumes a *sharp* transition from an inductively-dominated regime at temperatures below T_c to a resistively-dominated one above T_c . The nonlinearities in the normal state are associated with non-equilibrium Cooper pairs whose effect is more substantial in the oxygen-deficient samples. From the fit of harmonic data acquired on YBCO thin films with various doping levels, estimates of the lifetime of Cooper pairs in the normal state are extracted and their doping dependence reveals that underdoped cuprates deviate more significantly from the predictions of the microscopic BCS theory.

The model presented in Chapter 5 has some limitations. First it is a DC treatment, although the measurements are performed at microwave frequencies. However the approximation is valid to a certain extent. Second, both the inductive and resistive nonlinear effects are "packed" in discrete circuit elements, i.e. inductive/resistive nonlinear effects are treated in terms of current-dependent inductor/resistor, similar to most of the models from the literature that describe nonlinear effects in superconducting transmission lines or resonators.

In order to overcome these issues, in Chapter 6 a finite-frequency, field-based description of the near-field microwave nonlinear microscope is proposed. Instead of treating the nonlinear effects in a lumped-element picture, as in Chapter 5, the

nonlinear effects are approached in a more natural way, as deviations of the complex conductivity from its low-power, linear-response regime.

The main reason for developing the model in Chapter 6 was the acquisition of a vector network analyzer with harmonic detection capabilities; it was the experimental data that prompted the need for a finite-frequency description since the model presented in Chapter 5 covers the extreme cases of "*inductive only*" and "*resistive only*" nonlinear regimes below and above T_c respectively. For this reason the dissertation was constructed in a chronological fashion: as experimental data accumulated, after using the new instrument, it became obvious that a more general theoretical model is required for the understanding of the new harmonic data.

At this point it has to be emphasized that phase-sensitive microwave harmonic data reported in this thesis are a novelty: the only similar data have been reported in the literature by a group at NIST, Boulder, CO, but the data is restricted to the temperature of 76 K only. Only the power dependence has been investigated but this is not very revealing since at $T=76$ K a superconductor with $T_c = 93$ K behaves in a predictable fashion. The drawback of this situation is that at this moment there is no theoretical framework that can be implemented to interpret in detail the phase-sensitive data presented here. For this reason, the data analysis is restricted to a semi-quantitative level.

Summary, conclusions and directions for future work are outlined in Chapter 7.

Chapter 2

The microwave response of the superconducting state

E finalmente altro non si inferisce [...] da *vinum*,
che VIS NUMerorum, dai quali numeri essa Magia dipende[†].

Cessare della Riviera, *Il Mondo Magico degli Eroi*

Mantova, Osanna, 1603.

2.1 Linear electrodynamics of superconductors in BCS theory

The microscopic theory of superconductivity called BCS [12] after the names of its founders (Bardeen, Cooper and Schrieffer) has been proposed in 1957 as a generalization of the concept of Cooper pairing [13]. Within this theoretical framework, it is shown that an arbitrarily weak attraction between two electrons above the Fermi sea results in a bound state of the two electrons called a Cooper pair. The Cooper pairs are responsible for the dissipationless current in the DC regime, which in a two-fluid picture is attributed to the superfluid. Quasiparticles, which are the rough equivalent of the normal fluid, are created by breaking Cooper pairs and their effect in electrical conduction is to add a negative contribution, called *quasiparticle backflow*, to the superfluid flow.

The electrodynamics of isotropic weak-coupling superconductors described by

[†]And finally nothing is [...] inferred from *vinum* save VIS NUMerorum, upon which numbers this Magia depends.

BCS has been discussed by Mattis and Bardeen [14] together with expressions for the real and imaginary parts of the complex conductivity $\sigma_{1,2}(T)$. For $T > 0$ K numerical integration is required[†] but at $T = 0$ K $\sigma_{1,2}(T)$ can be written in terms of elliptic integrals \mathfrak{E} and \mathfrak{K} .

Although a microscopic theory, BCS does not describe accurately the microwave linear response of cuprates in the sense that the temperature dependence of real part of conductivity $\sigma_1(T)$ measured in cuprates does not exhibit the features predicted by BCS[‡]. Concerning the nonlinear effects, the complicated mathematical apparatus of the BCS theory does not allow for a finite-frequency description in simple mathematical form. The two-fluid model, despite its limitations, provides a semi-quantitative picture, and for this reason the electrodynamics of the two-fluid model is briefly presented below.

2.2 Linear electrodynamics of superconductors in the two fluid model

At finite temperature, the charge carriers in a superconductor are described in terms of two fluids: the normal fluid, which in a microscopic picture is associated with the quasiparticles, and the superfluid, associated with the Cooper pairs

[†]A FORTRAN computer code to evaluate the temperature-and frequency-dependence of the complex conductivity is given in W. Zimmerman, E. H. Brandt, M. Bauer, E. Seidel, and L. Genzel, **Optical conductivity of BCS superconductors with arbitrary purity**, Physica C 183, 99 (1991)

[‡]For a review on the microwave linear response of cuprate single crystals see Ref[15]. Temperature-dependent complex conductivity is typically fitted by the modified two-fluid model where the quasiparticle scattering time is assumed temperature-dependent.

(the condensate). The normal fluid has the properties of electrons from a normal metal, exhibiting finite conductivity, while the superfluid is characterized by infinite conductivity at zero-frequency ($\omega = 0$) and otherwise finite conductivity. This description becomes more transparent if the electrodynamics of the superconducting state is examined in the framework of the two-fluid model.

As shown in most superconductivity textbooks, if one considers a sinusoidal time variation for the external field (here the electric field, $E \sim \exp(i\omega t)$) and solves the equations of motion for carriers (superfluid and normal fluid), a Drude-like complex conductivity is obtained:

$$\tilde{\sigma} = \sigma_1 - i \cdot \sigma_2 \quad (2.1)$$

with σ_1 given by the normal fluid only (in the case of non-zero frequencies):

$$\sigma_1 = \frac{n_n e_0^2}{m_e \omega} \cdot \frac{\omega \tau_{qp}}{1 + (\omega \tau_{qp})^2} = \frac{n_n e_0^2}{m_e \omega} \cdot \mathfrak{F}(\omega \tau_{qp}) = \frac{2}{\mu_0 \omega \delta_{sk}^2} \quad (2.2)$$

where the function $\mathfrak{F}(\omega \tau_{qp}) \equiv \omega \tau_{qp} / (1 + (\omega \tau_{qp})^2)$ has been introduced to simplify the equations. n_n represents the normal fluid density, ω is the angular frequency of the external field, τ_{qp} is the quasiparticle scattering time (average time between two consecutive collisions with the solid lattice) and m_e and e_0 are the electron mass and electric charge, respectively. At microwave frequencies ($\omega \sim \text{GHz}$), the product $\omega \tau_{qp}$ is much smaller than 1 [15]. Similar to the case of electrodynamics of normal metals, one can introduce a length scale δ_{sk} representing the penetration depth of external electromagnetic fields, called the skin depth.

The imaginary part of conductivity contains contribution from both the su-

perfluid and the normal fluid:

$$\sigma_2 = \frac{e_0^2}{m_e \omega} \left(n_S + n_n \cdot \frac{(\omega \tau_{qp})^2}{1 + (\omega \tau_{qp})^2} \right) = \frac{e_0^2}{m_e \omega} (n_S + n_n \mathfrak{G}(\omega \tau_{qp})) = \frac{1}{\mu_0 \omega \lambda^2} \quad (2.3)$$

with n_S the superfluid density and $\mathfrak{G}(\omega \tau_{qp}) \equiv (\omega \tau_{qp})^2 / (1 + (\omega \tau_{qp})^2)$. One can define a length scale λ describing the penetration of electromagnetic fields in a superconductor, similar to the skin depth introduced previously. One of the fundamental properties of superconductors is the Meissner effect. It is the spontaneous expulsion of external fields from the bulk interior of a superconductor (perfect diamagnetism) and is characterized by λ which represents the length scale of exponential decay of external fields in a bulk superconductor. Due to the large conductivity associated with the superfluid $n_S (T < T_c)$, the superconducting state is characterized by very small values of λ ($\sim 10^2$ nm for HTS), much smaller than the skin depth associated with the real part of the conductivity at microwave frequencies. Equation 2.3 shows that the diamagnetic screening is achieved by *both* the superfluid n_S and the normal fluid n_n . In the limit of zero-frequency $\omega = 0$ there is no contribution from the normal fluid to the screening process and the London penetration depth λ_L is recovered $\lambda_L = \sqrt{m_e / (e_0 \mu_0 n_S)}$. At finite frequencies and at temperatures below T_c the main contribution to the screening process comes from the superfluid component of σ_2 and λ can be approximated by λ_L . This is the limiting case usually encountered in the literature when it can be safely assumed that $n_n \mathfrak{G}(\omega \tau_{qp}) \ll n_S$ and the second component of the imaginary part, representing ballistic screening by the normal fluid, can be neglected. In this case, or equivalently, at low frequency of the external field (when $\mathfrak{G}(\omega \tau_{qp}) \rightarrow 0$), the penetration depth λ approaches the

London penetration depth λ_L .

The electric field-to-current density constitutive equation for a superconductor ($\vec{J} = \tilde{\sigma}\vec{E}$), used together with the Maxwell equations leads to the wave equation for the electric/magnetic field inside a superconductor. For the case of sinusoidal time variation, the Maxwell equations read:

$$\nabla \times \vec{E} = -i\omega\vec{B} \quad (2.4)$$

$$\nabla \times \vec{H} = \vec{J} + i\omega\vec{D} \quad (2.5)$$

$$\nabla \cdot \vec{B} = 0 \quad (2.6)$$

$$\nabla \cdot \vec{E} = 0 \quad (2.7)$$

where $\vec{B} = \mu\vec{H}$ and $\vec{D} = \epsilon\vec{E}$. By applying the $\nabla \times$ operator to the Faraday law Eq.(2.5) and using Ampere's law Eq.(2.4) along with the constitutive equation one obtains the wave equation for the electric field:

$$\Delta\vec{E} = i\omega\mu(\tilde{\sigma} + i\omega\epsilon)\vec{E} \quad (2.8)$$

where the coefficient of \vec{E} is the complex propagation constant $\gamma^2 = i\omega\mu(\tilde{\sigma} + i\omega\epsilon)$ and the solution has a spatial dependence $\sim e^{-\gamma z}$ if the plane wave propagates along the z direction. A similar equation can be obtained for \vec{H} and \vec{A} if one applies the $\nabla \times$ operator to the Ampere's law Eq.(2.4), the constitutive equation $\vec{J} = \tilde{\sigma}\vec{E}$ and uses Faraday law Eq.(2.5):

$$\Delta\vec{H} = i\omega\mu(\tilde{\sigma} + i\omega\epsilon)\vec{H} \quad (2.9)$$

Some limiting cases are useful to discuss since it will become obvious that the propagation constant γ deduced above is a generalization of similar expressions used in

the literature. For example, if the displacement current is neglected with respect to the conduction current (reasonable assumption at microwave frequencies) one obtains:

$$\gamma^2 = i\omega\mu(\sigma_1 - i\sigma_2 + i\omega\epsilon) \approx i\omega\mu\sigma_1 + \omega\mu\sigma_2 \quad (2.10)$$

By taking into account the relationship between conductivity and the length scales introduced previously, the penetration depth λ and the skin depth δ_{sk} , the propagation constant can be recast in the form:

$$\gamma^2 \approx i\omega\mu\sigma_1 + \omega\mu\sigma_2 = \frac{2i}{\delta_{sk}^2} + \frac{1}{\lambda^2} \quad (2.11)$$

This is the generalization of the London screening to finite frequencies as used frequently in the literature (see, for example [16], [17]). In the limit of zero-frequency, the wave equation Eq.2.9 reduces to the London equation $\Delta\vec{H} = \gamma^2\vec{H}$ with $\gamma = 1/\lambda_L$. If the propagation constant γ is written in terms of conductivity for the case of negligible displacement currents:

$$\gamma \approx \sqrt{i\omega\mu\sigma_1 + \omega\mu\sigma_2} = \sqrt{\omega\mu\sigma_1 \left(i + \frac{\sigma_2}{\sigma_1} \right)} \quad (2.12)$$

the limit $T > T_c$ (in the normal state), $\sigma_2/\sigma_1 \rightarrow 0$ and a power expansion of the above equation, where only the first term is retained shows that γ reduces to the propagation constant $(1+i)/\delta_{sk}$ for the normal skin depth effect.

In the London theory, it was shown that the superfluid is set in motion by a magnetic field (London's first equation) while the normal fluid by a time-varying electric field (Ohm's law). In the case of an external DC magnetic field, only the superfluid will respond and provide the Meissner screening characterized by the

length scale introduced by London (the London penetration depth λ_L). In the presence of a time-varying magnetic field, the normal component responds to the time-varying electric field $\vec{E} = -\partial\vec{A}/\partial t$ and provides a certain degree of screening quantified by the microwave skin depth δ_{sk} . At temperatures not too close to T_c (when $n_n \ll n_S$) and at frequencies in the range of microwaves, the superfluid diamagnetic screening dominates ($\lambda \rightarrow \lambda_L$), $\lambda \ll \delta_{sk}$ and consequently the normal fluid screening can be safely neglected. Intuitively, one would expect that for a fixed temperature and an increasing frequency of the external field the normal fluid starts to contribute more significantly to the screening (as the terms $\mathfrak{F}(\omega\tau), \mathfrak{G}(\omega\tau) \rightarrow 1$ in the Drude-like expression for $\sigma_{1,2}$). For a fixed frequency ω and the temperature approaching T_c , $T \rightarrow T_c$, the skin depth δ_{sk} decreases and becomes comparable to the penetration depth λ . At a given temperature there is a frequency scale Ω_1 when $\delta_{sk} = \lambda$ that marks a transition point between the Meissner screening, described by λ , and the skin depth screening, described by δ_{sk} . This cross-over frequency Ω_1 is a characteristic time scale of the electrodynamics of superconductor. The other fundamental time scale is related to the ability of the superconducting order parameter to adiabatically follow the time variation of the external field and is linked to the nonlinear response of superconductors to external fields.

2.3 Microwave nonlinear response of superconductors

The Drude-like equations from the previous section describing the complex-valued conductivity $\tilde{\sigma}$ were derived with the tacit assumption that the external field

does not perturb the two fluids, n_S and n_n . Investigating the properties of the superconducting system (for example conductivity $\tilde{\sigma}$) with a probing field whose magnitude is gradually increased should lead to the same results if the system is not altered during the measurement. This is called linear approximation since the response of the system, "normalized" by the excitation is an invariant quantity, characteristic of the system properties. In most, if not all, real-life systems, this is not true; for case treated here, an external perturbation increases the free energy of the superconductor, driving it toward the normal state.

In a two-fluid picture, this corresponds to a suppression of the superfluid density n_S , or equivalently, of the superconducting order parameter (in the extreme case, a "probing" magnetic field of magnitude H_c or a current density J_c destroys superconductivity all together). Strictly speaking, any perturbation, no matter how small, alters the superconducting state; however, the induced changes can be insignificant. When the external field approaches a well-defined threshold, which is associated with the critical field H_c , the equilibrium between the superfluid and the normal fluid is modified and the electromagnetic properties depart from the low-field, linear response, non-perturbed values.

The first observation of nonlinear effects in superconductors dates back to 1950 when Pippard observed significant deviations from the behavior predicted by the London linear-response theory: the penetration depth λ increases with the applied magnetic field and the effect is more pronounced near the critical temperature T_c [18]. The experimental findings could not be explained by using the London theory and the two-fluid model of Gorter and Casimir, the only theoretical frameworks

available at that time.

The first theory to consider the suppression of superconductivity by an external field or current was proposed by Ginzburg and Landau (GL) in 1950 [19]. In the GL theory the superconducting state is described by introducing a complex function, called the order parameter Ψ , which is zero in the normal state and finite in the superconducting one.

By using the BCS formalism and its conceptual framework, Parmenter approached the nonlinear effects from a microscopic point of view [20]. In parallel with the development of microscopic models, the phenomenological GL theory was extended to non-stationary phenomena, leading to the Time-Dependent Ginzburg-Landau theory (TDGL): whereas GL is a zero-frequency approach, TDGL takes into account the effect of the finite frequency and introduces two time scales that govern the electrodynamics of superconductors in external fields.

Experimental work has investigated the current-dependent reactance/resistance of superconducting films [21], superconducting-to-normal state switching effects [22] and the harmonic generation [23], and the data have been successfully interpreted by using GL and its time-dependent versions, and Parmenter's model.

After the discovery of high- T_c superconductors, the interest in the microwave nonlinear response has been revitalized: the first experimental harmonic investigation concluded that the phenomenological TDGL equations that describe accurately the low- T_c materials do not reproduce the nonlinear data acquired on YBCO single crystals. Consequently modifications have been implemented in the original TDGL equations to fit the data [24]. On the other hand, microscopic treatments taking into

account the d-wave symmetry of the order parameter have been proposed starting in 1992 [25, 26]. Since then, various refinements of the theory have been proposed to account for the effect of gap suppression due to the superfluid flow [27] and that of fluctuations above T_c [28, 29, 30].

Experimental work employing microwave resonant techniques have explored the harmonic generation and intermodulation distortion processes and confirmed predictions of the microscopic models in various temperature ranges [31, 32, 33].

In the following, a brief review of theoretical approaches to the problem of nonlinear effects in superconductors is presented. As shown in this short chronological overview, the theoretical models employ either a phenomenological description, a GL-type or a microscopic BCS-type theory. Each approach has advantages and disadvantages. Despite their differences the pictures should, in principle, describe the same underlying physics.

2.3.1 Microscopic theories of the nonlinear effects in superconductors

Since a microscopic theory of high- T_c superconducting materials is not on hand yet, the only available approach to the problem of microwave nonlinear effects is to use a BCS-like formalism (with the appropriate order parameter symmetry, shape of the Fermi surface, dimensionality, anisotropy, etc) and evaluate the current-dependent conductivity at finite-frequency. Unfortunately, this task has not been achieved due to mathematical difficulties even in a "pure" BCS framework adequate for low- T_c superconductors [34] and approximations were used to obtain

predictions that can be compared with experiment. For this reason, at present, all microscopic treatments of the nonlinear response in conventional and unconventional superconductors consider the DC case only, which in some cases is a good approximation.

The first attempt to solve the problem of nonlinear effects in a microscopic model belongs to Parmenter [20]. By extending BCS to regimes of current densities comparable to the critical one J_c , it was shown that at finite temperatures, $T > 0$, when the Cooper pairs are set in motion (superflow), quasiparticles are created and tend to counteract the effect of the superflow. This effect was called *quasiparticle backflow* and constitutes the starting point of most microscopic calculations. Parmenter's model has been confirmed in measurements of nonlinear reactance/resistance of superconducting films [21].

With the discovery of high- T_c superconductors and the debate concerning the symmetry of the order parameter, investigations of the field-dependent penetration depth λ in cuprates were proposed as a powerful tool for detecting the structure and symmetry of the order parameter, as suggested by Xu, Yip and Sauls [25] in their treatment of the Nonlinear Meissner Effect (NLME). The theory predicted measurable changes in the field- and angular dependence of the penetration depth due to the presence of nodes in a d-wave order parameter. For this reason the traditional NLME experiments have been done by measuring very small changes in large linear-response background quantities (e.g. penetration depth). Due to the nonlinear processes associated with generation and motion of magnetic vortices many of these experiments were considered inconclusive and raised questions about

the validity of the theory [35, 36, 37, 38, 39, 40]. Vortices often penetrate a sample from a weak spot on an edge or corner, and single crystal samples are particularly prone to this problem because of the large Meissner screening currents at those locations. It was recognized by our group that edges and corners must be eliminated from the NLME measurement to effectively exclude this extrinsic process.

Overall in the community it was realized that a new approach was required to measure nonlinear effects in high-temperature superconductors. Given the inconclusiveness of the traditional NLME experiments, Dahm & Scalapino (DS) recommended a different experimental approach with a higher sensitivity: microwave harmonic and intermodulation distortion measurements [26] where nonlinear signals with zero background are measured.

The starting point of the DS model is the equation of current density, viewed as a competition between the superfluid flow and the quasiparticle backflow, as in the early treatment of Parmenter. At temperatures $T \approx 70$ K, typical for the operation of high-temperature superconducting filters, the quasiparticles are in thermodynamic equilibrium with the condensate[†] which is tacitly assumed to oscillate in phase with the external field. By writing a BCS-type equation for the quasiparticle backflow and expanding it in power series of J/J_c , the 3rd order nonlinear effects on the superfluid density have been characterized quantitatively by introducing a coefficient which depends on temperature and the orientation of the superfluid flow

[†]In this framework the quasiparticle scattering time is much smaller than the period of the microwave current $\tau_{qp} \ll \omega^{-1}$.

with respect to the crystalline axes a and b , $b_\theta(T)$:

$$\frac{n_S(T, J)}{n_S(T, 0)} = \frac{\lambda^2(T, 0)}{\lambda^2(T, J)} \approx 1 - b_\theta(T) \left(\frac{J}{J_c}\right)^2 + \dots \quad (2.13)$$

where $n_S(T, J)$ ($\lambda(T, J)$) is the superfluid density (penetration depth) at temperature T in the presence of the current density J while $n_S(T, 0)$ and $\lambda(T, 0)$ represent the same quantities in the absence of current (low-power, linear-response), θ is the angle between the superflow and the CuO bonds, as defined in the DS treatment, and J_c is the zero-temperature critical current density ($b_\theta(T)$ is explained in detail below).

The microscopic model has been formulated to predict nonlinear effects in high- T_c superconducting microwave filters employed by the wireless industry, where the intermodulation distortion IMD products must be minimized. For this reason, the authors took into account only the first J -dependent term, $(J/J_c)^2$, in the power series of the quasiparticle backflow current density. This is the term responsible for the IMD products at angular frequencies $2\omega_1 - \omega_2$ and $2\omega_2 - \omega_1$ generated when ω_1 and ω_2 are the input signals, and the 3^{rd} order harmonic if the single-tone ω is applied at the input.

$b_\theta(T)$ is the nonlinear coefficient that carries information about the intrinsic physics of the system: the shape of the Fermi surface and the nature of the superconducting gap. Consequently, nonlinear measurements are aimed at determining the temperature and angular dependence of the coefficient $b_\theta(T)$. Eq.2.13 shows explicitly that the current density J suppresses the superfluid density n_S and enhances the penetration depth λ , as observed in the early experiments of Pippard [18]; this

constitutes the nonlinear Meissner effect.

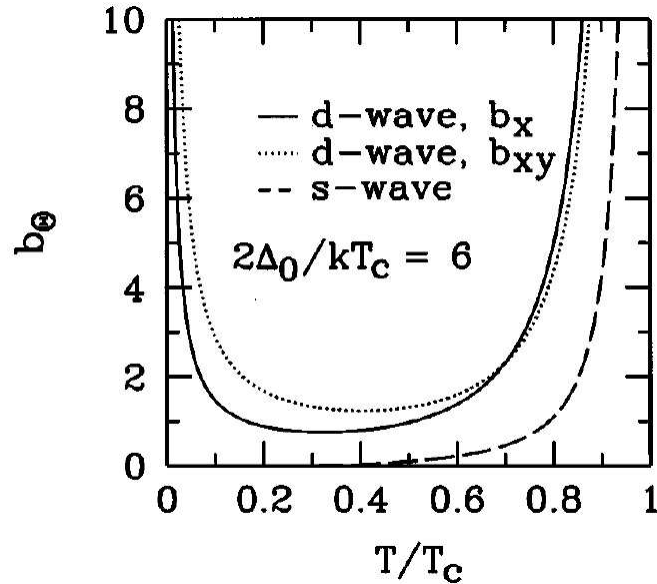


Figure 2.1: Temperature- and angular dependence of the nonlinear coefficient $b_\theta(T)$ evaluated numerically for a d-wave superconductor (solid line $b_x(T)$ and dotted line $b_{xy}(T)$) and an s-wave superconductor (dashed line) for $2\Delta_p/k_B T_c = 6$ [26].

The DS model provides the angular- and temperature dependence of the magnitude of nonlinear effects as shown in Fig.2.1. The divergence of $b_\theta(T)$ at T_c is a general characteristic of the superconducting state and is caused by the superfluid density being extremely sensitive to external fields, in agreement with the phenomenological picture of the GL theory. At low temperatures, in d-wave superconductors, the divergence of $b_\theta(T)$ is caused by the existence of nodes of the order parameter on the Fermi surface and constitutes a signature of the d-wave symmetry.

Through the nonlinear coefficient $b_\theta(T)$ the DS microscopic model assesses the changes in the populations of the superfluid and that of the normal fluid, followed by evaluations of the real and imaginary parts of the complex conductivity $\sigma_{1,2}$.

The next step for DS is to model the microwave resonator or transmission line in a lumped-element approximation and study its response to an excitation consisting of two tones with angular frequencies ω_1 and ω_2 . This is the step where the results of the zero-frequency microscopic analysis are introduced in the finite-frequency model of the resonator or transmission line.

Due to the dependence of $\sigma_{1,2}$ (through the coefficient $b_\theta(T)$) on the input power, a microwave current at angular frequencies $2\omega_1 - \omega_2$ and $2\omega_2 - \omega_1$ is generated in the device and the microwave power at these mixed frequencies, P_{IMD} , is evaluated. Due to the dependence $P_{IMD}(T) \sim b_\theta^2(T)$, measurements of the intermodulation power give access to the nonlinear coefficient $b_\theta^2(T)$, thus making the IMD (and similarly the harmonic generation) measurements a powerful tool to investigate the physics of the superconducting state at a microscopic level. Some experimental results from the literature that use this formalism are briefly presented in section §2.4.

A refinement of the DS model consists of taking into account the suppression of the superconducting gap by the superfluid flow. Within this model it is shown that the approximation of a superflow-independent gap, as assumed in the DS treatment, is strictly accurate only at low temperatures up to $t = 0.2$ [27].

One limitation of the above DC microscopic treatment is the divergence of the nonlinear response at T_c ($P_{3f,IMD}(T \rightarrow T_c) \rightarrow \infty$), feature which is not observed experimentally. Several reasons for the unphysical result at T_c are:

1. the approximate nature of the power expansion from Eq.2.13. Very close to

and at T_c other terms in the power expansion of the quasiparticle backflow might be essential and limit the divergent behavior;

2. the suppression of the superconducting gap by the superflow, as considered in Ref.[27];
3. the finite-frequency effects that are not considered in the microscopic analysis.

In the DS formulation it is not explicitly stated that the order parameter is assumed to oscillate in phase with the external field, i.e. the time scale associated with the inertial properties of the order parameter (called the relaxation time of the order parameter τ_Δ) is much smaller than the inverse of the microwave current frequency. However, for $T < T_c$ (for example at ~ 70 K where the DS analysis is applicable, compared to $T_c = 92$ K for YBCO for example), the above assumption is valid at microwave frequencies. According to the Time-Dependent Ginzburg-Landau TDGL theory, reviewed in the next section, in close proximity to T_c the order parameter cannot adiabatically follow the external excitation ($\tau_\Delta \rightarrow \infty$) and the divergent behavior of $P_{IMD,3f}$ at T_c is eliminated.

2.3.2 Phenomenological theories of the nonlinear effects in superconductors

Mean-field approaches

The first successful theory explaining nonlinear effects in superconductors was the phenomenological zero-frequency Ginzburg-Landau theory proposed in 1950. The GL equations for a sample infinite in the horizontal plane and with a thickness

smaller than the penetration depth λ ("one-dimensional" problem) can be solved analytically in some limiting cases and the suppression of the order parameter by the external field becomes obvious. The problem of a superconducting slab with thickness $d_0 \ll \lambda$ is solved in detail in Appendix A.

Various versions of GL-like equations describing the nonlinear effects are used in the literature. For example the suppression of the superfluid density n_S and the enhancement of the penetration depth due to a current density J is typically written by introducing a phenomenological temperature-dependent characteristic nonlinear current density scale, $J_{NL}(T)$, that quantifies the strength of the nonlinear effects [41, 42, 43, 44, 45]:

$$\frac{n_S(T, J)}{n_S(T, 0)} = \frac{\lambda^2(T, 0)}{\lambda^2(T, J)} \approx 1 - \left(\frac{J}{J_{NL}(T)} \right)^2 + \dots, J \ll J_{NL}(T) \quad (2.14)$$

The nonlinear current density scale $J_{NL}(T)$ is a material parameter, does not depend on sample geometry or magnetic field configuration, and can be approximated in the GL picture by $J_{NL}(T) = J_c(1 - t^2)(1 - t^4)^{1/2}$ for intrinsic effects. Here $t = T/T_c$ is the normalized temperature and this expression for $J_{NL}(T)$ has been obtained by solving the one-dimensional GL equations for a superconducting slab [21]. For other types of nonlinearities (vortex motion, Andreev Bound States, weak links, etc.), one has to use an appropriate functional dependence for $J_{NL}(T)$. From this point of view, the phenomenological picture gives a certain amount of freedom: often experimentalists extract the nonlinear current density scale from data without making any assumptions on the mechanism that generates the observed nonlinear behavior [41, 42, 43].

The suppression of the superfluid density by the current, and the corresponding enhancement of the penetration depth as quantified by the phenomenological Eq.2.14, is similar to its microscopic counterpart Eq.2.13 from the previous section.

Both the microscopic and the GL-based phenomenological approaches presented so far do not include any frequency-dependent effects, being essentially DC treatments. For temperatures very close to T_c the situation is different because the inertial properties of the order parameter become significant. This has been shown at the end of 1960's by Gor'kov and Eliashberg (GE) who modified the original GL equations to adapt them to non-stationary processes.

In the GE picture, a time-varying external field of angular frequency ω "modulates" the order parameter with a period equal to that of the field, as long as the response time of the order parameter is shorter than $2\pi/\omega$. In this case, the order parameter "sees" the instantaneous value of the external field and oscillates in-phase with the field. In a two-fluid picture the superfluid undergoes periodic suppressions and recoveries and so does the normal fluid in conditions of thermodynamic equilibrium with the superfluid. As the angular frequency ω is increased (or equivalently the temperature approaches T_c) there will be a threshold frequency $\omega = \Omega_0$ above which the order parameter cannot adiabatically follow the external field and instead, it experiences the effect of the time-averaged external field. Ω_0 represents a fundamental time scale characterizing the dynamics of the superconducting order parameter and diverges at T_c [16, 23, 24, 47, 48].

Due to the vanishing of the frequency scale Ω_0 at T_c , in a harmonic generation experiment with a fixed frequency ω and an increasing temperature T , harmonic

generation should shut down at a normalized temperature t^0 where $\Omega_0(t^0) \sim \omega$, as shown in Ref.[16] and Ref.[48]. An estimation of the temperature t^0 for YBCO single crystals at $\omega = 2\pi \cdot 6.5$ GHz (employed in the harmonic generation experiments reported here) is given later in this section and is based on experimental data and modeling from Ref.[24]. An interesting feature of the GE theory is that the nonlinear behavior of superconductors at very high frequencies (or very close to T_c) still manifests itself in intermodulation distortion effects [16, 48].

This qualitative discussion suggests that the investigation of the microwave nonlinear response has the potential of providing estimates for the time scale Ω_0 . For this reason, the traditional harmonic generation experiments were aimed at determining the timescale Ω_0 [22, 23, 24].

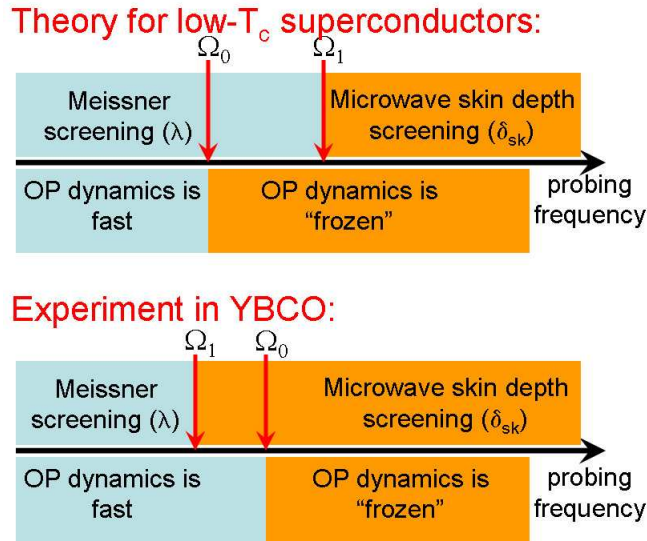


Figure 2.2: Frequency scales describing the electrodynamics of superconductors. Comparison between Gor'kov & Eliashberg theory and observations from experiments on YBCO single crystals of Leviev *et al.*.

Investigations of the microwave linear-response of superconductors give access to another fundamental time scale characterizing the superconducting state: Ω_1 which represents the frequency cross-over between Meissner screening, at low frequencies ($\omega < \Omega_1$, characterized by the length scale λ) and the skin depth screening where the superconductor behaves like a normal metal ($\omega > \Omega_1$, characterized by the length scale δ_{sk}).

The original GE theoretical treatment was formulated for gapless superconductors with a large concentration of paramagnetic impurities where $\Omega_0 = \Omega_1$ [47]. Later calculations for dilute alloys (low- T_c superconductors) by Wohlman revealed that $\Omega_0 < \Omega_1$ [17].

The situation in high- T_c single crystals is different, as observed in the experiments of Leviev and co-workers [24], where the two time scales are reversed $\Omega_0 > \Omega_1$. A schematic of the GE theory predictions and the experimental findings of Leviev *et al.* is shown in Fig.2.2 and suggests that the physics of high- T_c superconductors is different than that of their low- T_c counterparts.

From the experiment and a fit of the data with a modified GE theory, it was concluded that $\Omega_0(t)[Hz] \sim 1.8 \cdot 10^{14}(1-t)$ while $\Omega_1(t)[Hz] \sim 1.6 \cdot 10^{13}(1-t)$ showing that close to T_c the order parameter responds slowly to the external field and the skin depth screening dominates [24]. The estimations for $\Omega_{0,1}$ suggest that the DC approximation inherent to the microscopic approaches is valid up to temperatures extremely close to T_c if the probing excitation has frequencies in the GHz range. For example, for frequencies used in the experiments reported in this dissertation ($f \approx 6.5$ GHz), the reduced temperature where the order parameter relaxation time

becomes comparable to $1/f$ is about $t^0 \approx 0.99996$ and that where the Meissner screening is replaced by skin depth screening is $t^1 \approx 0.9996$.

A feature unique to the finite-frequency GE model compared to the DC microscopic ones is that at T_c the harmonic response P_{3f} is finite and experimentalists have been able to numerically fit $P_{3f}(T)$ data even at T_c without introducing cut-off parameters [23, 24].

The models reviewed so far are all mean-field approaches, where the effect of fluctuations is neglected. The TDGL theory and its variations have been implemented to investigate the effects of order parameter fluctuations on the macroscopic properties of superconductors starting with the end of 1960's.

Fluctuation effects

Fluctuations are an additional source of electrodynamic nonlinearity in superconductors. They lead to an enhancement of the real part of the conductivity σ_1 . The enhancement is electric field-dependent because the field tends to destroy the fluctuation (non-equilibrium) Cooper pairs. Initially the linear-response effect has been examined theoretically by Schmidt by means of TDGL below and above T_c [49]. The linear-response treatment of Schmidt for $T > T_c$ has been extended to describe the nonlinear effects by Hurault [50] and Schmid [51]. Within this theoretical model, spontaneous fluctuations of the order parameter that are described by TDGL, can be qualitatively pictured as 'droplets of Cooper pairs' above T_c [50, 51, 52].

A temperature-dependent electric field scale has been introduced, $\widetilde{E}_0(T)$ which defines the regime of low ($E < \widetilde{E}_0(T)$) or high electric field ($E > \widetilde{E}_0(T)$). The value

for the characteristic electric field $\widetilde{E}_0(T)$ in the case of isotropic materials depends on the zero-temperature coherence length ξ_0 and the reduced temperature $\epsilon = (T - T_c)/T_c$ as $\widetilde{E}_0(\epsilon) = E_0\epsilon^{3/2} = [16\sqrt{3}k_B T_c/(\pi e_0 \xi_0)]\epsilon^{3/2}$ where k_B is the Boltzmann constant and e_0 is the electron charge [28].

For the case of an isotropic superconductor, in the limit of low electric field ($E < \widetilde{E}_0(T)$), the critical and Gaussian fluctuation regimes involve an E^2 correction to the zero-field conductivity:

$$\sigma_1(T, E)/\sigma_1(T, 0) - 1 \sim (E/\widetilde{E}_0(T))^2 \quad (2.15)$$

while in the case of high-field ($E > \widetilde{E}_0(T)$) the Gaussian fluctuation regime (the only regime experimentally accessible in low- T_c materials) leads to the dependence:

$$\sigma_1(T, E)/\sigma_1(T, 0) \sim (E/\widetilde{E}_0(T))^{-(4-d)/3} \quad (2.16)$$

where d represents the dimensionality of the sample under study [28]. This electric field dependence of the conductivity has been confirmed in experiments on low- T_c materials: thin films with $d = 2$ [53] and wires with $d = 1$ [54].

In cuprates, characterized by high critical temperatures T_c and short coherence lengths, the effects of fluctuations is more accessible from the experimental point of view and for this reason the interest in this field was re-vitalized. The modern mathematical treatment of superconductors above T_c consists in solving the TDGL equations with an external noise term to model the effect of fluctuations [28]. This way, the critical and Gaussian fluctuations and their effect on the electric field-dependent DC conductivity have been studied theoretically [28, 30].

An alternative approach was proposed by Mishonov and co-workers who evaluated the nonlinear effects on the DC conductivity in layered materials (cuprates). Their approach is to solve a Boltzmann-type equation for the fluctuation Cooper pairs and provides predictions for the electric-field dependent σ_1 [29].

Concerning the frequency-dependent response, the TDGL equations with a noise term allowed the analytical estimation of linear complex conductivity $\tilde{\sigma}$ for arbitrary dimensionality [28] and for layered cuprates [55]. The nonlinear response involves mathematical difficulties that do not allow for closed-form equations [28, 29]. For this reason, in Chapter 5 where resistive nonlinear effects are investigated experimentally, the DC value of the cross-over electric field evaluated for layered materials in Ref.[29] has been used.

2.4 Prior experimental work on microwave nonlinear effects in superconductors

Microwave experimental techniques have been used extensively to study the physics of the superconducting state. The traditional approach dating back from the studies of Pippard [18], is to insert the superconducting sample into a resonator and monitor the resonant frequency and the quality factor as the temperature or the input power is varied.

For harmonic microwave studies, bimodal resonators tuned at the fundamental and at the 3^{rd} order harmonic have been used (see, for example, Ref.[23] and [24]). In order to generate measurable nonlinear effects, the sample must be subject to

high microwave screening currents, a situation which is achieved if the sample is placed inside the resonator at a location of maximum magnetic field. Experimental data consist of the magnitude of the harmonic power $|P_{3f}(T)|$ and exhibit a peak in the vicinity of the critical temperature, as observed also in the measurements reported in this dissertation (see Chapters 5 and 6).

Traditionally, the main motivation for the studies of nonlinear effects in superconductors was to gain access to information which otherwise cannot be extracted from linear-response measurements: the relaxation time of the order parameter in the superconducting state Ω_0^{-1} . Harmonic measurements acquired on the low- T_c superconductor $\text{La}_{1-x}\text{Gd}_x\text{Sn}_3$ ($x = 0.1$, $T_c \approx 3K$ and $x = 0.08$, $T_c \approx 3.9K$) have been interpreted by using the GE formalism, described in the previous section. The order parameter relaxation time varies as $\Omega_0^{-1} \sim (1 - t^2)$ close to T_c with the proportionality constant on the order of 10^{12} Hz [23].

The interest in the microwave nonlinear behavior of superconductors has been renewed after the discovery of the high- T_c materials and is driven by its twofold aim: the investigation of the fundamental physics governing the superconducting state (the spectroscopy of the superconducting gap, the nature and location of the nodes of the $d_{x^2-y^2}$ wave gap [25], and the detection of possible phase transitions between superconducting phases with different symmetries of the order parameter [56]) and the optimization of high- T_c superconducting microwave filters used in the wireless industry.

The first harmonic measurements on cuprates reported in the literature belong to Leviev and co-workers in 1989. Harmonic data $|P_{3f}(T)|$ acquired on YBCO single

crystals have been numerically fitted by using a GE-like mathematical formalism and both timescales $\Omega_{0,1}^{-1}$ have been estimated, as mentioned in the previous section[†].

With the advent of high- T_c superconducting microwave filters, harmonic generation and intermodulation distortion measurements were performed in experimental set-ups where the superconducting sample acts as a resonator. These studies have provided experimental support for the microscopic models of nonlinear effects in cuprates proposed by Xu, Yip and Sauls [25] and Dahm and Scalapino [26]. The Nonlinear Meissner effect at low temperatures in d-wave superconductors, enhanced by the presence of nodes of the order parameter on the Fermi surface has been detected by measuring the magnitude of the IMD microwave power [31, 32].

The theoretical studies of Dahm & Scalapino addressing the operation of high- T_c superconducting microwave resonators have shown that under certain specific circumstances, the dominant nonlinear mechanism in these devices has an inductive origin due to the enhancement of the penetration depth λ by the current (or applied magnetic field) [26]. For this reason and due to the lack of harmonic phase information, data acquired on YBCO thin films in the vicinity of T_c have been considered mainly inductive in nature. However, an experimental investigation of harmonic effects in YBCO thin films with various doping levels suggested that such a picture is accurate in optimally-doped samples, but significant deviations have been observed in underdoped samples [44, 45]. A novel interpretation of these data is provided in Chapter 5.

[†]At the time when these studies were performed, the microscopic theory of Xu, Yip and Sauls [25] was not available.

Phase-sensitive measurements of the harmonic response of cuprates at microwave frequencies have been performed by a group at NIST, Boulder, CO by using a YBCO coplanar waveguide and a nonlinear vector network analyzer (NVNA) [42, 43]. Harmonic data have been acquired at the fixed temperature of 76 K for various input power levels (2 to 16 dBm) and analyzed by using a lumped-element model of the transmission line.

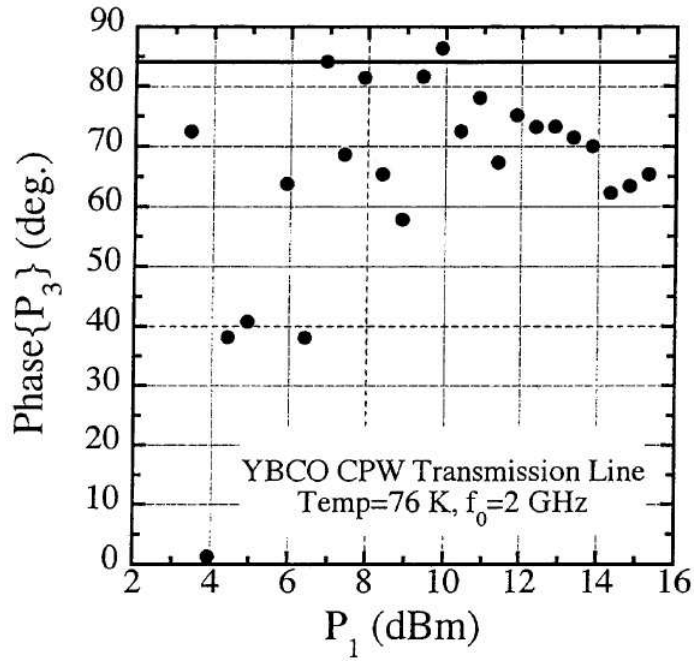


Figure 2.3: Harmonic phase data acquired on a YBCO coplanar waveguide at 76 K from Ref.[42].

The analysis of the harmonic phase reveals that at 76 K the inductive nonlinear behavior dominates the resistive one in magnitude, leading to a harmonic phase of roughly $\pi/2$ at low power levels, as shown in Fig.2.3. The effect of increasing the input power manifests itself in an apparent decrease of the harmonic phase below $\pi/2$ (see the experimental points acquired with 12 to 16 dBm input power in Fig.2.3) and

is somewhat equivalent to raising the temperature[†]. This is in qualitative agreement with the temperature-dependent harmonic phase data reported in this dissertation in Chapter 6.

[†]From thermodynamic considerations, the external field increases the free energy of the superconductor driving it toward the normal state.

Chapter 3

The nonlinear near-field microwave microscope

Wee haue divers curious Clocks; and other like Motions of Returne:
and some Perpetuall Motions [...] These are the Riches of Salomons House.

Francis Bacon, *New Atlantis*, London, 1627

3.1 Introduction and motivation

In this chapter two versions of the nonlinear near-field microwave microscope are described. In the present study, these instruments have been used for the characterization of harmonic effects in cuprate thin films, at temperatures close to T_c . The experimental apparatus employed for the linear-response measurements on magnetic materials reported in Chapter 4 as well as the experimental procedure are discussed therein due to the particular nature of magnetic measurements.

The first instrument, the scalar nonlinear near-field microwave microscope, has been used in the past to image nonlinear effects from an artificially-created bicrystal boundary, thus proving its local imaging capabilities [57]. Additionally, the nonlinear Meissner effect at T_c has been investigated in homogeneous YBCO thin films with various doping levels by means of this experimental apparatus [44].

The second instrument, the vector nonlinear near-field microwave microscope,

has phase-sensitive harmonic detection and inherits the local capabilities of the first one since it employs the same type of microwave probe. Therefore, the first section of this chapter presents in detail the microwave probe and its interaction with the sample under investigation with emphasis on the issue of probe sensitivity, i.e. the probe ability to induce screening currents in the sample and to pick up the reflected signal. The discussion of probe sensitivity is raised to a quantitative level in section §3.2 by introducing the concepts of *figure of merit* and *probe-to-sample electromagnetic coupling*. The experimental apparatus for the scalar and vector microwave harmonic measurements is described in detail in sections §3.4 and §3.5.

3.2 The microwave probe, its near-field and the interaction with the sample

The essential component that gives local capabilities to the microwave measurements reported in this thesis is the microwave probe. In the original set-up, the probe, called UT034, was fabricated by soldering the inner conductor to the outer one of a commercial coaxial transmission line UT034 in order to create a short circuit [44, 57, 58]. The loop created this way represents the field-concentrating feature that provides the magnetic field serving as the excitation for the sample placed in its proximity. This robust design allows one to reliably use the probe in a cryogenic environment whose temperature can be varied from 300 K down to 4 K. A $12\ \mu\text{m}$ thick Teflon sheet is placed between the probe and the sample to avoid direct electrical contact and to maintain a fixed probe-to-sample geometric separation.

Due to sample's interaction with the near-field of the probe, microwave screening currents are generated whose spatial distribution in the sample surface is dictated by the probe design and its geometric separation to the sample. An example is shown in Fig.3.1 where the electromagnetic field of the simple magnetic probe described above has been computed numerically with a commercially-available electromagnetic solver, CST-Microwave Studio [59]. The numerical simulation reveals that the magnetic field generated by this microwave probe is similar to that created by an ideal circular current loop[†].

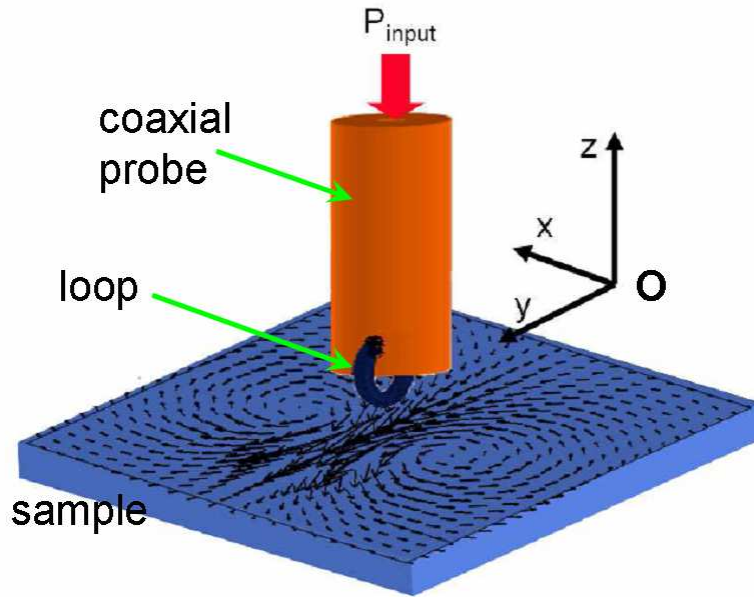


Figure 3.1: Schematic of the loop probe, sample and the induced microwave surface current (computed numerically with CST-MWS [59]).

The numerical simulations reveal that the current distribution in the sample peaks at a point below the loop (see Fig.3.1); consequently, if the probe is

[†]For a comparison between the field of a real loop probe and that of an ideal circular current loop, see Ref.[45]

placed far from the edges/corners of the superconducting sample, vortex entry at edges/corners where the microwave current vanishes is insignificant. Therefore, the local capabilities of this probe allow the investigation of sample's intrinsic physics. At an operating microwave power level of +10 dBm evaluated at the probe, the maximum microwave surface current induced in the sample is about 25 A/m as computed by using an electromagnetic solver [59] (see Fig.3.3). The sample is assumed to begin in the vortex-free Meissner state when zero-field cooled below T_c . Inside the cryostat the microwave probe is mounted on an arm whose position can be X-Y-Z controlled from outside, thus conferring scanning capabilities.

Since the UT034 probe has been utilized in microwave nonlinear response measurements, it is useful to analyze the factors that limit the probe sensitivity and to identify possible ways of resolving them. In a qualitative picture, one can imagine that when the electromagnetic wave traveling through the dielectric of the coaxial cable hits the surface of the inner conductor making up the loop it gets reflected and induces microwave screening currents in a thickness on the order of the skin depth in copper (the typical metal employed in coaxial transmission lines). According to this picture one would expect that the active region of the UT034 probe, where the microwave current peaks, is a thin layer located at the inner radius of the loop. This qualitative picture has been confirmed by numerical simulations and is illustrated schematically in Fig.3.2.

The above reasoning suggests that by mechanically removing material from the loop at the outer radius, the active region of the probe could be brought closer to the sample surface, thus enhancing the probe sensitivity. For the measurements

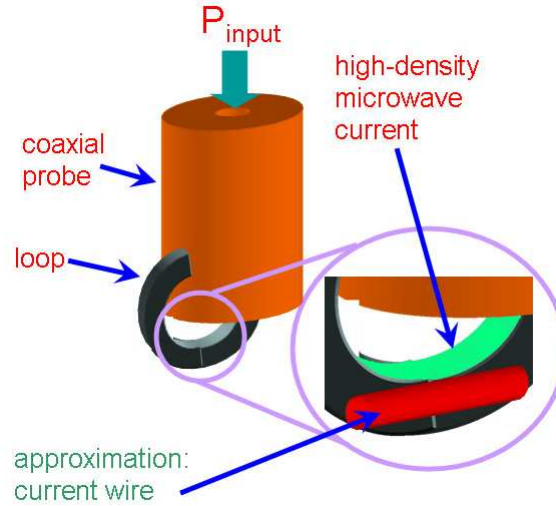


Figure 3.2: Loop probe, the active region where high-density microwave screening currents (shown with green) are induced by the incoming microwave signal and the current wire approximation (shown with red).

reported in Chapter 6 a UT034 probe has been modified by polishing the inner conductor making the loop at its outer radius. With the modified probe the overall sensitivity of the experimental set-up increases, leading to a P_{3f} higher by +13 dB compared to the one acquired in similar conditions with the original UT034 probe.

Since measurements reported in Chapter 4 have been performed at room temperature, issues related to thermal contraction of materials from the coaxial cable making the probe are not relevant. Thus, a more radical solution could be adopted to enhance the probe-sample electromagnetic interaction. In a first effort, the loop was replaced by a thin wire bond directly between the inner and outer conductors while keeping the probe in physical contact with the sample. Since the wire diameter ($\sim 25\mu\text{m}$) is much smaller than that of the inner conductor of UT034 coaxial cable ($\sim 0.2\text{ mm}$) the probe-to-sample electromagnetic interaction was enhanced and a

vector network analyzer could be used in frequency-swept mode for the first FMR measurements with such a technique [60].

For room-temperature measurements the sensitivity was further enhanced with a novel probe design and fabrication process. A 500-nm thick Cu film (with resistivity $\rho \approx 2.1 - 2.3 \mu\Omega cm$) was deposited directly on a cross-sectional cut of the coaxial cable UT085 in an e-beam evaporator. In a second fabrication step, the Cu film was patterned into a narrow bridge connecting the inner and outer conductors to create the short-circuit for the incoming microwave signal. This Cu bridge ("micro-loop") has a length of about 500 μm with widths in the range 100-300 μm and generates a highly-localized and unidirectional magnetic field h_{MW} . Since for the operating frequencies ($f \sim 0.1 - 20$ GHz) the microwave skin depth in Cu is larger than the Cu film thickness (500 nm), the induced microwave current generating the probe's excitation field h_{MW} , is uniform in the 500 nm thickness. This constitutes a field-enhancing feature of the novel probe and, depending on the capabilities of the probe-to-sample positioning system, can be brought very close to the sample surface. For the measurements reported in Chapter 4 the probe-to-sample separation was on the order of tens of microns.

The room-temperature microwave probe can be further improved by depositing the Cu film on coaxial transmission line of smaller dimensions (for example UT020) with the Cu "micro-loop" patterned by using focused ion beam (FIB), which ultimately would allow a reduction of the probe width to a nm scale and result in higher sensitivity and improved spatial resolution.

3.3 Numerical modeling of the probe-sample electromagnetic interaction

The previous section presented three designs for the microwave probe which have been implemented for the experiments reported in this dissertation. The topic of this section is the numerical modeling of the induced current distribution; this step is of great importance for understanding the absolute harmonic power measurements from Chapter 5. The main advantage of the numerical modeling consists in its capability to reproduce accurately the field and current distribution from the real-life experimental configuration. With the advent of commercially-available electromagnetic solvers optimized for microwave frequencies this task has been simplified tremendously. However, in some cases it is instrumental to rely on an analytical approach in order to gain some insight into the problem. For this reason, at the end of this section, starting from an intuitive picture of the current distribution induced in the inner radius of the loop by the incident microwave signal (see Fig.3.2), a simplification of the probe geometry is presented, which is later used in an analytical model in Chapter 6.

In order to relate the *absolute* harmonic power measured with a spectrum analyzer, quantitative information about the probe's near-field and the corresponding current distribution induced in the sample is required. In the past, the sensitivity of the nonlinear near-field microwave microscope has been quantified by introducing the *figure of merit*, Γ , defined for the superconducting state [45]. In the limit of films thinner than the penetration depth λ , the figure of merit is determined by the

surface current distribution in the sample [45]:

$$\Gamma = \frac{\int \int K^4 dx dy}{\int_{-x_0}^{x_0} K_y dx} \quad (3.1)$$

where $\vec{K} = K_x \hat{x} + K_y \hat{y}$ and $I_0 = \int_{x_0}^{x_0} K_y dx$ are the screening surface current density and the total screening current induced by the near-field of the probe in the sample. The surface current distribution $\vec{K}(x, y)$ has been computed numerically by using two electromagnetic solvers (CST Microwave Studio, CST-MWS [59] and Ansoft High Frequency Structure Simulator, HFSS [61]). The superconducting sample has been defined as a perfect (lossless) conductor and the computed surface current distribution has been exported in order to evaluate the integrals in Eq.(3.1). A top view of the surface current distribution is shown in Fig. 3.3 and it exhibits the main features of a current distribution induced by the magnetic field of an ideal circular current loop on a perfectly conducting surface. The integral in the denominator of Eq.3.1 is evaluated for $x = -x_0 \dots + x_0$ where x_0 is the distance from origin up to the X location where K_y changes sign (in this figure it corresponds to the location of the current vertexes). The integral in the numerator is evaluated over the sample surface.

For the evaluations from Chapter 5 a similar computation must be performed to evaluate the figure of merit for a film in the normal state Γ_ρ . To accomplish this goal in the electromagnetic solver a finite-resistivity sample is defined, with $\rho \approx 100 \mu\Omega \cdot cm$ (typical for YBCO in the normal state immediately above T_c) and the induced surface current distribution is computed numerically.

The figure of merit Γ was evaluated for a coaxial magnetic probe located above

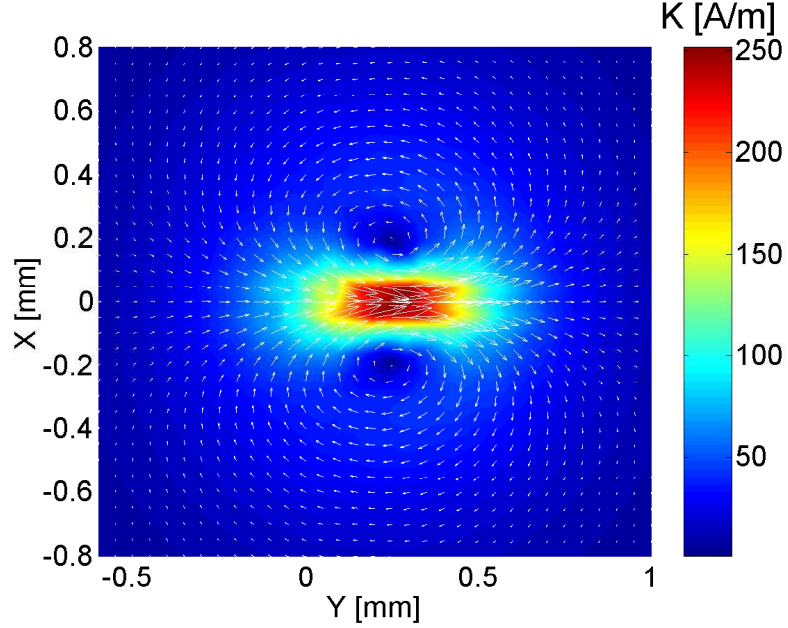


Figure 3.3: Top view of surface current distribution $\vec{K} = K_x\hat{x} + K_y\hat{y}$ induced on the sample surface by a coaxial loop probe UT034 placed at $12 \mu\text{m}$ above the sample. The computations have been performed with CST-Microwave Studio for an input power of 1 W.

a perfectly conducting sample and the result of integration is $\Gamma = 7.7 \text{ A}^3\text{m}^2$ for an input power of 10 dBm. Similarly, for the finite-conductivity sample the figure of merit is $\Gamma_\rho = 7.6 \text{ A}^3\text{m}^2$ evaluated at the same power level. In principle both figures of merit Γ and Γ_ρ depend on the input frequency through the spatial distribution of the near-field. However in the range of frequencies used for this experiment (6.5 to 19.5 GHz) and due to the near-field configuration where all spatial dimensions involved in the problem are much smaller than the wavelength of the probing signal, it can be assumed that the frequency dependences of Γ and Γ_ρ are very weak. In terms of power dependence, both figures of merit scale with the input power as

$P_{input}^{3/2}$ as suggested by Eq.3.1.

Another issue to be considered is that only a fraction of the microwave power injected into the probe reaches the sample, and similarly only a fraction of the harmonic power generated at the sample surface couples back into the probe. This situation is modeled by using a transformer model with the primary coil represented by the microwave probe, and the secondary coil by the probe's image in the sample. The coupling coefficient k representing the voltage at the secondary terminals when the primary is biased with 1 V has been evaluated numerically for a perfectly conducting sample by using the method of images and it was found $k \approx 3\%$ as shown in detail in [45]. Intuitively, one can imagine that the coupling coefficient k varies between 0 and 1: for an ideal probe-to-sample coupling $k = 1$ while as the probe is moved further away from the sample k decreases to 0.

For purposes of evaluating the absolute harmonic power, in Chapter 5, the coupling coefficient k must be evaluated both in the superconducting and the normal state. For a sample in the normal state the problem is more complicated since the classical method of images may not be applicable. However, since numerical simulations performed with a finite-resistivity sample showed that the screening current distribution induced on the sample surface does not differ significantly from that evaluated for a perfectly conducting sample one can safely assume that the coupling coefficient k is similar. This assumption is confirmed also by the similar values for the figures of merit Γ and Γ_ρ , as shown previously.

In order to model analytically the probe-sample interaction, the coaxial loop probe can be replaced by an idealized circular current loop and its magnetic field

can be expressed in terms of the complete elliptic integrals \mathfrak{E} and \mathfrak{K} [46]. In such a situation the mathematical details could obscure the fundamental physics of the problem and for this reason a simpler approach is used in the thesis: since most of the microwave current that generates the antenna's field is "crowded" at the surface of the inner radius of the loop, as shown in Fig.3.2, it is reasonable to model the loop as a wire parallel to the sample surface. By implementing this approximation the electromagnetic problem of probe-sample interaction has been solved analytically in Chapter 6.

3.4 Experimental apparatus for scalar harmonic measurements

In the harmonic generation experiments presented in this dissertation the objective is to locally stimulate a superconducting thin film with microwave currents and measure the reflected harmonic power or voltage. The microwave signal at the fundamental frequency $f \approx 6.5$ GHz is generated by a microwave source (see Fig.3.4) and low-pass filtered in order to suppress its higher-order harmonics. This excitation signal is coupled locally to the sample by means of the magnetic loop probe described previously and labeled UT034 which is located in close proximity of the sample.

In the absence of nonlinear effects in the sample, the reflected microwave power coupled back to the probe has only one Fourier component at the frequency of the incident signal f . However, due to sample's nonlinear properties, the spectral content of the reflected microwave power includes higher-order harmonics $2f, 3f, \dots$

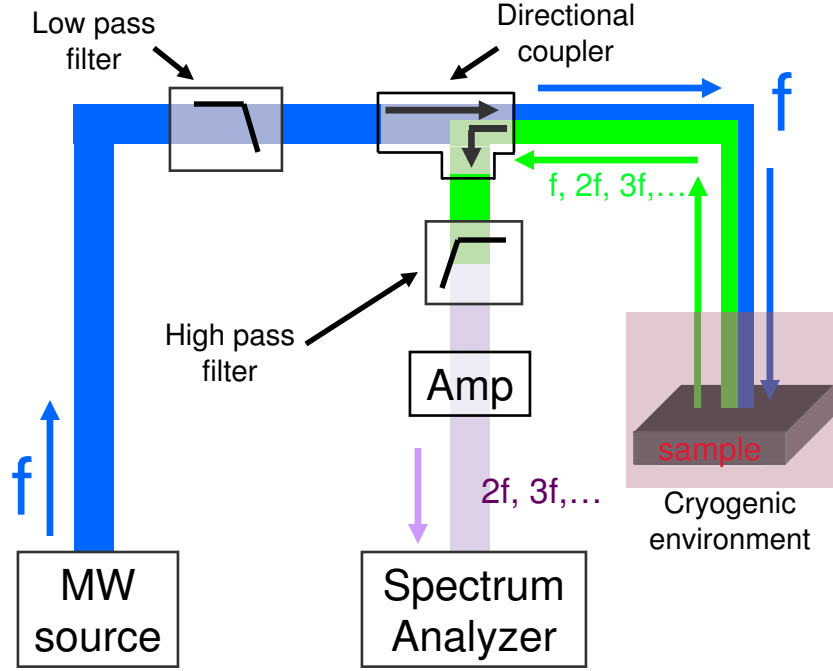


Figure 3.4: Schematic of the experimental apparatus for the scalar harmonic measurements.

with the $3f$ component representing the signal of interest in the measurements reported in the thesis[†]. The reflected signal is coupled back to the microwave probe and propagates on the same path as the incident wave until the directional coupler whose purpose is to provide separate paths for the incident and the reflected power (see Fig.3.4).

Since the detection system is typically a nonlinear device (spectrum analyzer

[†]Note that 2^{nd} order harmonic measurements $P_{2f}(T)$ on superconductors have been extensively studied by Sheng-Chiang Lee [45]. Here $P_{2f}(T)$ was not considered because the focus of this work is on the intrinsic NLME rather than Time-Reversal Symmetry Broken (TRSB) effects near T_c . $P_{2f}(T)$ signals are orders of magnitude lower than $P_{3f}(T)$ signals and could not be detected reliably with the novel experimental set-up.

or vector network analyzer) it is necessary to suppress the microwave power at the fundamental frequency, which represents the dominant component of the power reflected from the sample. Suppression is accomplished by means of two high pass filters that ensure a rejection of about 80 dB up to a frequency of about 11 GHz. In the absence of the high-pass filtering, the microwave signal at the fundamental frequency f would generate harmonics in the detection system which could mask the harmonics originating from the sample.

In order to boost the power carried by the harmonic power after the high-pass filtering, two broadband microwave amplifiers are inserted into the microwave circuit. A measurement with a vector network analyzer showed that the two amplifiers provide a gain of about 52 dB at the 3rd harmonic $3f \approx 19.5$ GHz [45].

For the scalar harmonic measurements presented in Chapter 5 the source for the probing signal was a microwave synthesizer model HP 83620B while a spectrum analyzer Agilent model E4407B was employed as the detection device. The experiment consists in controlling the temperature in the cryostat and monitoring the reflected power carried by the third-order harmonic signal $P_{3f}(T)$ with the spectrum analyzer. The sample is placed in a magnetically-shielded environment (external fields are attenuated by roughly 90 dB) whose temperature is controlled between 20 and 100 K with an accuracy of 0.1 K by using a Lakeshore model 340 temperature controller. Since the detection instrument is a spectrum analyzer, the harmonic power is measured in absolute units, dBm, representing power relative to 1 mW on a logarithmic scale.

3.5 Experimental apparatus for vector harmonic measurements

The experimental set-up presented in the previous section, employing a spectrum analyzer, is a powerful tool to measure absolute power levels reflected from a nonlinear sample, however, it has no sensitivity to the phase of the harmonic power. In order to overcome this limitation, the detection system has been replaced by a vector network analyzer (VNA) Agilent model E8364B with harmonic capabilities.

In the new configuration, the VNA internal microwave source provides the excitation signal on port 1 at a fixed frequency $f \approx 6.5$ GHz in the continuous-wave (CW) mode, while the reflected signal is measured on port 2 (see Fig. 3.5). The VNA is equipped with the *frequency offset mode* (FOM) option which allows the user to tune the receiver on port 2 to a different frequency range than that of the microwave source on port 1[†].

One limitation of this set-up is that the microwave power incident on the sample cannot be varied in a large range as was the case for the previous set-up ($P_{input} = -20 \dots +20$ dBm). The VNA can reliably generate microwave power levels only up to +8 dBm. This limitation has been mitigated by using a more sensitive probe, the modified UT034 probe, described in section §3.2. The microwave amplifiers used for scalar harmonic measurements have been eliminated since the modified probe UT034 has an enhanced sensitivity compared to its predecessor.

In order to perform phase-sensitive detection of the harmonic voltage incident

[†]In a typical VNA, as the one used for the measurements reported in Chapter 4, the source and the receiver are locked on the same frequency.

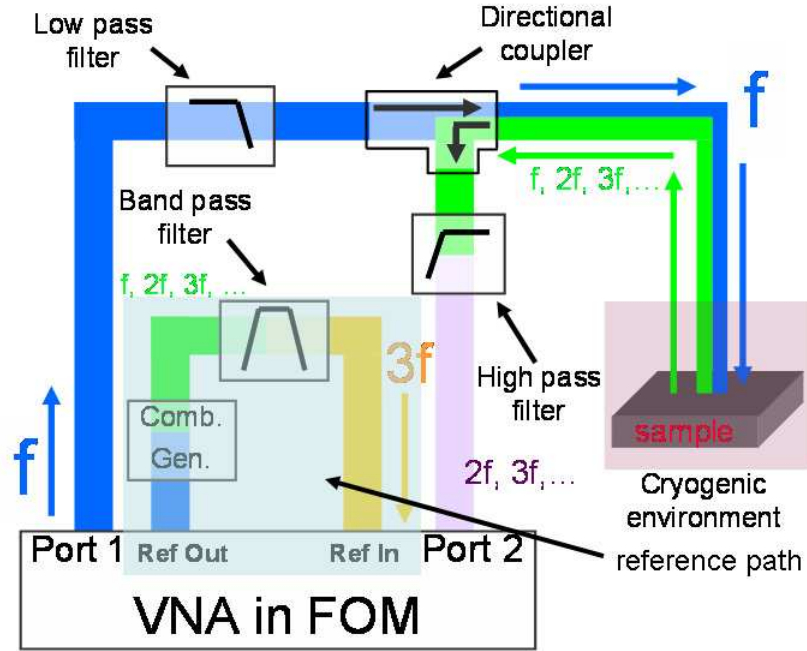


Figure 3.5: Schematic of the experimental apparatus for the phase-sensitive harmonic measurements.

on port 2, the VNA needs a reference signal at the same frequency as the signal to be analyzed namely $3f$. For this reason, an additional microwave circuit is required, the *reference path*, shown in Fig. 3.5. Some microwave power generated by the internal VNA source[‡], and available at the port **Ref Out** (see Fig. 3.5), is delivered to a comb (harmonic) generator (Herotek, model number GCA 2026A-12) that produces several higher-order harmonics (for this Herotek model, about 10 harmonics are generated). Since the measurement of interest is performed at frequency $3f$, two band-pass filters providing an attenuation of 80 dB, are inserted in the reference path

[‡]Measurements of the microwave power at port 1 and at the **Ref Out** with a power meter show that the reference path is excited with a signal carrying a power of about 20 dB below the power available on port 1.

immediately after the comb generator to suppress the fundamental and all harmonics except for $3f$. The band-pass filtered microwave signal is incident on the **Ref In** port, and serves as reference, U_{3f}^{ref} , for the phase-sensitive measurements. The data acquired from the VNA in the frequency-offset mode (VNA-FOM) represents the complex ratio of the voltage from the sample, U_{3f}^{sample} , to that of the reference U_{3f}^{ref} .

In an experiment, the reference path is operated at constant room temperature[†] while controlling the temperature of the sample inside the cryostat. The measured complex harmonic voltage $U_{3f}^{sample}(T)/U_{3f}^{ref}$ contains information about the sample and the microwave circuit (coaxial cables, filter, directional coupler, etc) as well as about the reference path (comb generator, band-pass filters, coaxial cable, etc). Because the reference path and most of the microwave circuit are at room temperature (only about 10 cm of coaxial cable is inside the cryostat, however not in physical contact with the cold plate), it is legitimate to assume that the temperature dependence of the measured harmonic voltage $U_{3f}^{sample}(T)/U_{3f}^{ref}$ originates entirely from the temperature-dependent nonlinear effects in the sample.

In order to perform VNA-FOM measurements a *power calibration* is required. The power calibration has been performed with a power meter according to the instructions of the manufacturer [62]. After the power calibration, the VNA-FOM instrument is able to measure the absolute power level incident on port 2 similar to a spectrum analyzer.

The VNA-FOM is not designed for measurements of *absolute phase*, as is

[†]Before each experiment the comb generator was turned on at least four hours prior to starting the data acquisition to make sure that stable operating conditions are reached.

the case with the Large Signal Vector Network Analyzer (LSNA), but for *relative* phase measurements in order to compare the nonlinear characteristics of *different* microwave devices[†]. Consequently, the phase information provided by the VNA in FOM operation is *relative* in the sense that it only indicates how the phase *changes* from one device to another, or more appropriately formulated for the situation reported here, how the device-under-test (the sample) changes from one temperature to another. This implies that the temperature-dependent phase data $\Phi_{3f}^{sample}(T) - \Phi_{3f}^{ref}$ acquired from the VNA (see for example Fig.6.2), are offset by an unknown amount. This phase shift originating from the phase winding in the components of the microwave circuit (coaxial cables and filters) and the phase relationship between the fundamental and the harmonics generated by the comb generator cannot be eliminated through a linear-response calibration with standards (open, short, 50 Ω load and through) since the excitation and the response have different frequencies (f vs. $3f$). A number of attempts were made to define an absolute nonlinear phase reference (see Appendix B).

A phase-sensitive harmonic measurement consists in exciting the superconducting sample with a single-tone microwave signal at frequency f generated from VNA's port 1 and tuning the receiver on port 2 in a narrow frequency range (1 or 2 Hz) centered on $3f$. This procedure is similar to the one performed with the spectrum analyzer, where one acquires traces representing the absolute power incident on the input port (in dBm units) vs. frequency. The VNA-FOM outputs a string

[†]The author acknowledges useful conversations on nonlinear phase measurements with Mario Mule & O. J. Danzy from Agilent.

of complex numbers (trace) representing the $U_{3f}^{sample}/U_{3f}^{ref}$ ratio evaluated at the frequency points scanned by the receiver. At each temperature a trace is acquired and stored on the acquisition PC for further processing.

The two experimental set-ups have been used to measure harmonic data on cuprate thin films, as reported in Chapter 5 and 6.

Chapter 4

Near field microwave microscopy and linear response of magnetization dynamics

nature does not call for long recipes.

Paracelsus

4.1 Introduction and motivation

In the last 30 years there has been tremendous progress in the area of magnetic recording. The areal recording densities have increased remarkably while the cost per bit has dropped due to advances in magnetic recording technologies: the introduction of thin-film read-write heads, giant-magnetoresistance read heads and more recently the perpendicular magnetic recording (PMR). Similarly, the data rate has increased significantly, exceeding the gigabit per second (Gbps) threshold and driving bandwidth requirements as high as several GHz for the magnetic elements that make up hard drives and magnetic random access memory (MRAM). Due to the dynamic response of magnetic materials, frequencies of this scale encroach on the ferromagnetic resonance (FMR) of the soft magnetic layers integral to the sensors and storage layers of these technologies. In particular, the frequency characteristics of the soft underlayer, SUL (an essential component of the PMR media), might become

a limiting factor in further progress of magnetic recording technologies. With this in mind, it is essential to elucidate the magnetization dynamics of these devices and materials, both independently and in their system-dependent environment. Thus, high-frequency characterization of the structured heads and disks that incorporate these materials is instrumental to the continued advance of data-storage technology, and perpendicular recording in particular. Fundamental to the dynamics are physical parameters like damping α and frequency linewidth Δf , the understanding of which is influenced by sample geometry and measurement technique [63].

Therefore, it is desirable to expand the spectrum of FMR characterization tools in order to better explore this parameter space. Traditionally, FMR is measured using microwave cavities or striplines [63, 64, 65], where the sample size and geometry is constrained by the measurement apparatus.

In this chapter a novel high-bandwidth local FMR probe is presented, where there is no constraint on the sample size or geometry, thus enabling high-frequency measurements on a multitude of materials in their actual operating conditions [60, 66]. The work presented in this chapter has been done at Seagate Research, Pittsburgh, PA during the summers of 2005 and 2006 under the supervision of Dr. Thomas W. Clinton. The experimental set-up and the measurement procedure is presented in section §4.2 followed by the theoretical model describing the operation of the near-field microwave microscope and the relevant physics of magnetic materials in section §4.3. Section §4.4 presents measurements on several permalloy (Py) samples with various thicknesses with quantitative results that are in good agreement with those obtained from independent measurements (B-H hysteresis loops).

Since the ultimate goal is to FMR characterize realistic materials and devices, the next step was to study two disks employed in PMR; FMR results have been compared with Magneto-Optic Kerr Effect (MOKE) and Vibrating-Sample Magnetometry (VSM) results and the agreement is good. These results are reported in section §4.5.

A similar instrument with electric sensitivity (NeoMetriK) has been designed and fabricated by Neocera Inc., Beltsville, MD and the University of Maryland. It is a near-field microwave microscope equipped with an electrical probe capable of characterizing low-permittivity materials, which are of interest for the semiconductor industry [67].

4.2 Experimental set-up, samples and theoretical background

The main idea of the experimental approach is simple: if a microwave signal is incident on the magnetic system (sample) under investigation, the sample will absorb electromagnetic energy when the frequency of the incoming signal f coincides with the magnetic system's resonance frequency (ferromagnetic resonance frequency f_{FMR}). Thus, if the reflected microwave power is monitored in a frequency-swept experiment, the reflected-to-incident power ratio should exhibit a minimum at $f = f_{FMR}$. Such an experimental configuration is realized in a near-field microwave microscope where the sample is placed in close proximity to the field-enhancing feature of a magnetic microwave probe.

A scanning microwave probe with magnetic sensitivity has been demonstrated

by Lee *et al.*, [58]. The probe excites a small sample area and picks up the electromagnetic response by using a coaxial transmission line resonator terminated with a loop probe acting as an electrical short circuit [58]. The probe is fabricated by soldering the inner conductor to the outer, therefore the probe dimensions depend on those of the coaxial cable. The magnetic sample interacting with the probe near-field changes the boundary conditions at the end of the resonator as shown by a shift of the resonant frequency and a reduced quality factor [58].

A convenient and precise instrument for a reflection measurement at microwave frequencies is a vector network analyzer (VNA): the VNA provides the excitation signal (whose power and frequency can be accurately controlled) that propagates through a coaxial transmission line down to the microwave probe. In the absence of the sample, if the probe acts as a short circuit, a calibrated VNA measurement outputs a reflection coefficient $S_{11} = \widetilde{U}_{refl}/\widetilde{U}_{inc} = e^{i\pi} = -1$, where \widetilde{U}_{refl} and \widetilde{U}_{inc} represent the complex reflected and incident voltage, respectively. From transmission line theory it is known that the reflection coefficient characterizes the amount of mismatch between the impedance of the transmission line Z_0 and that of the load Z_T : $S_{11} = (Z_T - Z_0)/(Z_T + Z_0)$. As the sample is brought in close proximity to the probe and interacts with the incoming microwave signal, the reflection coefficient S_{11} deviates from -1. By using standard transmission line theory, S_{11} , is converted into total (load) impedance by using the relation $Z_T(f) = Z_0(1 - S_{11})/(1 + S_{11})$, where $Z_0 = 50 \Omega$ is the characteristic impedance of the coaxial transmission line. It is the total impedance $Z_T(f)$ that captures the information about the sample electromagnetic properties, as will be shown in the next section.

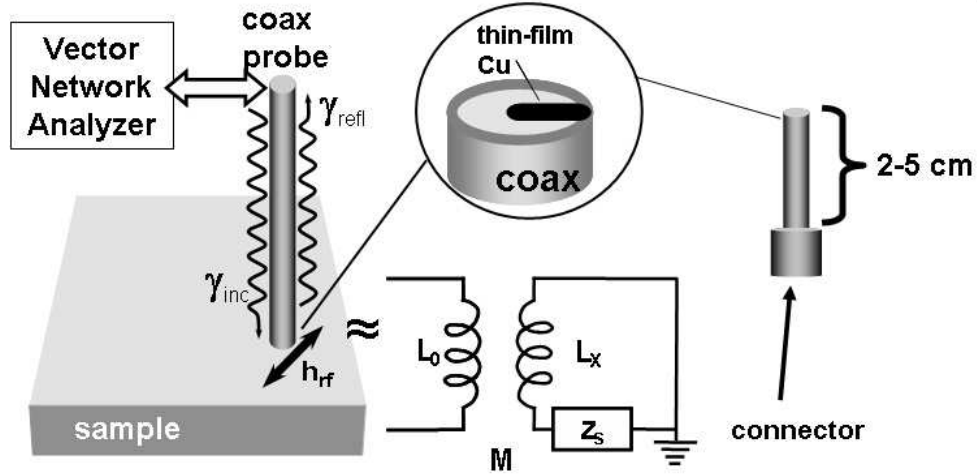


Figure 4.1: Schematic of the FMR coax micro-loop probe and the equivalent lumped-element model.

The goal of obtaining a high signal-to-noise ratio in local near-field microwave measurements is accomplished by enhancing the probe-to-sample electromagnetic interaction. This can be achieved by fabricating a probe whose field-enhancing feature (active volume), where microwave currents are induced under the influence of the incoming microwave signal, can be brought as close as possible to the sample surface. Two such designs that have been implemented for the measurements reported here are discussed in Chapter 3.

The microwave probe functions both as an emitting and as a receiving antenna to pick-up the sample response, captured in the reflected signal, γ_{ref} . The probe thin-film design minimizes the spacing between the microwave current and sample, maximizing their electromagnetic coupling, and the sheet-film geometry generates a highly unidirectional microwave field, as suggested by measurements on permalloy samples (see Fig.4.3).

In the experimental set-up, the coaxial cable terminated with the magnetic probe is fixed and the sample is loaded on an $x - y - z - \theta$ stage with sub-micron step resolution. By moving the sample with respect to the probe any point on the sample can be accessed and the sample can be brought in such close proximity that spacing loss is negligible. Additionally, the stage can be rotated in order to perform measurements with various orientations of the sample's easy-axis (EA) with respect to the applied magnetic fields.

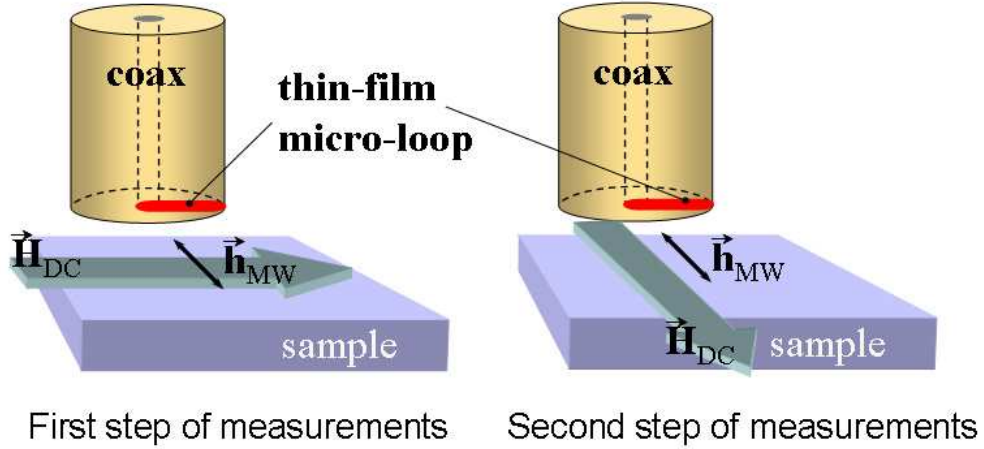


Figure 4.2: The measurement sequence and the orientation of the probing field h_{MW} with respect to the bias field H_{DC} .

The first step of the measurements is to perform a one-port calibration at the connector where the probe is inserted. This is accomplished by attaching standard short-circuit, open-circuit and 50Ω load [68]. Since the probe has a length of 2-5 cm from the connector to the active area that excites and picks up the electromagnetic response of the sample (see Fig.4.1), numerical de-embedding is performed to account for this length of the coaxial cable.

A four-coil system generates DC magnetic fields oriented in the plane of the sample. The measurement sequence consists of a saturating DC field, H_{DC} , applied **perpendicular** to the microwave magnetic field, h_{MW} , (see Fig.4.2) and the reflection coefficient $S_{11}(f, H_{DC}^\perp)$ is measured with the VNA. Next, a saturating DC magnetic field of the same magnitude is applied **parallel** to the probe's microwave magnetic field h_{MW} (see Fig.4.2), and the reflection coefficient $S_{11}(f, H_{DC}^\parallel)$ is measured with the VNA. Since the sample is saturated, the parallel orientation of the microwave field ($h_{MW} \parallel H_{DC}$) does not excite the precessional motion of the magnetization, and consequently FMR will be absent. Thus, this data set captures the background since it measures the nonmagnetic properties of the probe, its electrical image and sample substrate. Subsequent sets of data are acquired by modifying the magnitude of the applied DC magnetic field and repeating the above procedure.

To validate the experimental technique and the implementation of the theoretical model a 100 nm thick uniaxial permalloy (Py) film deposited on a 6" Si wafer was FMR characterized. A B-H looper was used to measure the saturation magnetization ($4\pi M_S \approx 10789$ Oe), the coercive field ($H_{co} \approx 6$ Oe) and the anisotropy field ($H_K \approx 4.5$ Oe).

Several sets of reflection coefficient magnitudes $|S_{11}(f, H_{DC})|$ are shown in Fig.4.3: the data from the main plot $|S_{11}(f, H_{DC}^\perp)|$ have been acquired with the sample oriented with its easy axis perpendicular to the microwave field ($H_{DC} \perp h_{MW}$, $h_{MW} \perp EA$): the magnitude of the reflection coefficient exhibits a small absorption dip which shifts to higher frequencies as the magnitude of the DC magnetic field is increased. Since the magnitude of the reflection coefficient is related to the

reflected-to-incident power ratio ($P_{reflected}/P_{incident} = |S_{11}|^2$), the dip from Fig.4.3 and its behavior with the applied DC field constitutes the signature of the ferromagnetic resonance. The slope of $|S_{11}(f)|$ represents the attenuation of the microwave power in coaxial cable of the probe.

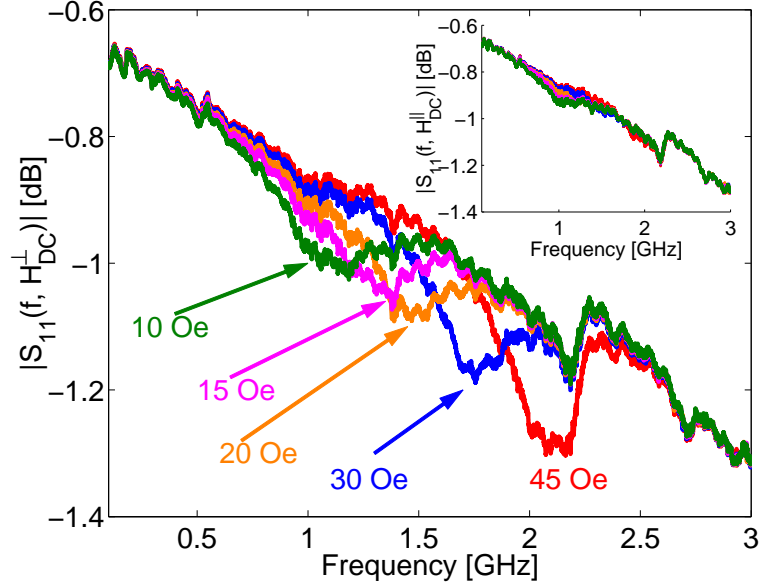


Figure 4.3: The magnitude of the reflection coefficient acquired on a 100 nm thick Py film: $|S_{11}(f, H_{DC}^{\perp})|$ measured in the FMR-active configuration ($H_{DC} \perp h_{MW}$, $h_{MW} \perp EA$). Inset: FMR-free background data.

When the saturating DC field is applied parallel to the microwave field ($H_{DC} \parallel h_{MW}$), there should be no magnetization response and consequently, the reflection coefficient S_{11} should not depend on H_{DC} . Such a behavior is observed in the experimental data shown in the inset of Fig.4.3: there is overlap of the $|S_{11}(f, H_{DC}^{\parallel})|$ curves measured with the H_{DC} magnitudes from the main plot. This qualitative observation suggests that the microwave probe generates a unidirectional field. Some deviations from this expected behavior occur for low H_{DC} magnitudes (below 15 Oe)

and could be caused by an incomplete saturation of the sample which is absent in the presence of a larger saturating DC field.

4.3 Theoretical background

This section presents a theoretical modeling of the near-field microwave microscope that establishes the relationship between the reflection coefficient S_{11} measured with the VNA and sample properties captured in the surface impedance. Next, the relevant theory of the magnetization dynamics, in particular ferromagnetic resonance and perpendicular spin wave modes, in magnetic thin films is given.

For the case of the near-field microwave configuration, where all geometrical dimensions are smaller than the probing wavelength, a lumped element approach is legitimate (see Fig.4.1). In this framework, the probe-sample system can be viewed as an electrical transformer whose primary coil is represented by the loop probe (modeled as an inductance L_0) and secondary coil is the electrical image of the loop probe in the sample (modeled as an inductance L_X). The mutual inductance between the two coils is M while the secondary circuit is loaded with $Z_S = R_S + iX_S$, which models the sample surface impedance, having a loss component (R_S) and a dispersion one (X_S). For sinusoidal time dependences, in complex phasor notation, the microwave probing signal is represented by the voltage \widetilde{U}_1 applied to the primary coil (loop probe) with the resulting current \widetilde{I}_1 . The equations for this lumped-element model are:

$$\widetilde{U}_1 = i\omega L_0 \widetilde{I}_1 + i\omega M \widetilde{I}_2 \quad (4.1)$$

$$0 = i\omega L_X \tilde{I}_2 + i\omega M \tilde{I}_1 + Z_S \tilde{I}_2 \quad (4.2)$$

\tilde{I}_2 is extracted from from Eq.4.1 and inserted into Eq.4.2. The resulting equation is:

$$0 = (i\omega L_X + Z_S) \tilde{U}_1 - i\omega L_0 \tilde{I}_1 (i\omega L_X + Z_S) - \omega^2 M \tilde{I}_1 \quad (4.3)$$

The complex ratio \tilde{U}_1/\tilde{I}_1 represents the total impedance at the terminals of the primary coil and can be obtained from the reflection coefficient S_{11} in a calibrated measurement with the VNA, $Z_T(f)$:

$$Z_T(f) = \frac{\tilde{U}_1}{\tilde{I}_1} = i\omega L_0 + \frac{\omega^2 M^2}{i\omega L_X + Z_S} \quad (4.4)$$

The same expression has been obtained by Anlage *et al.*, [69]. This equation can be re-written:

$$Z_T(f) = i\omega L_0 + \frac{\omega^2 \frac{M^2}{L_X}}{i + \frac{Z_S}{\omega L_X}} \quad (4.5)$$

In the approximation $|Z_S| \ll \omega L_X$, valid at microwave frequencies, the second term in Eq.4.5 can be expanded in power series and if one retains only the first two terms the load impedance seen by the VNA reads [66]:

$$Z_T(f) \approx i\omega L_0 (1 - k^2) + Z_S k^2 \frac{L_0}{L_X} \quad (4.6)$$

Here $k = \sqrt{M^2/L_X L_0}$ is a dimensionless coefficient ($0 < k < 1$) describing the probe-to-sample coupling. The magnetic measurement of interest is captured in the surface impedance, Z_S , which, in the thin-film limit with sample thickness d_0 much smaller than the microwave skin depth δ_{sk} ($d_0 < \text{skin depth}, \delta_{sk}$), has the form $Z_S = i\omega \mu_0 d_0 \mu_r$. μ_0 is the free-space permeability, and $\mu_r = \mu_1 - i\mu_2$ is the complex

magnetic permeability of the sample carrying information about the magnetization dynamics [70].

The critical parameter for the measurements is the coupling coefficient k which quantifies the amount of microwave power transferred from the probe to the sample. In the limit of poor coupling, when the sample is far away from the probe, $k = 0$ and the total impedance $Z_T(f)$ is reduced to that of the probe alone $i\omega L_0$. As the probe-to-sample coupling k is increased, the probe contribution to $Z_T(f)$ decreases while the sample contribution becomes more significant. In the limit of ideal coupling ($k = 1$), only the sample "signature" Z_S is present in the measured total impedance $Z_T(f)$.

Since an ideal coupling $k = 1$ cannot be achieved in a realistic experimental environment, one has to devise a subtraction procedure to eliminate the contribution of the probe and that of its electrical image in the sample from the total impedance detected in VNA reflection measurements; mathematically this corresponds to eliminating the first term in Eq.4.6. Several subtraction schemes have been proposed in the literature. For example, some authors have used the "high-field" subtraction where one acquires the background data while applying a high DC magnetic field in order to shift the FMR resonance peak to high frequencies [60, 71]. Another possibility is to apply a DC magnetic field of the same magnitude but oriented parallel to the microwave field, so that magnetization precession is not excited and the measured response captures everything but FMR [65, 71]. The latter subtraction algorithm has been implemented for the data presented in this chapter. The second term in Eq.4.6 is isolated by subtracting the total impedances measured with H_{DC}

perpendicular and parallel to h_{MW} :

$$\begin{aligned}\Delta_Z(f, H_{DC}) &= Z_T(f, H_{DC}^\perp) - Z_T(f, H_{DC}^\parallel) = k^2 \frac{L_0}{L_X} Z_S^{FMR} = \\ &= k^2 \frac{L_0}{L_X} [R_S^{FMR}(f, H_{DC}) + iX_S^{FMR}(f, H_{DC})] = k^2 \frac{L_0}{L_X} i\omega d_0 \mu_0 \mu_r\end{aligned}\quad (4.7)$$

The relative magnetic permeability μ_r is extracted from the measurement by using the surface impedance expression in the thin film limit:

$$\mu_r \approx \frac{1}{k^2} \frac{L_X}{L_0} \frac{1}{\omega d_0 \mu_0} (Im(\Delta Z) - iRe(\Delta Z)) \quad (4.8)$$

According to Eq.4.8 the real and imaginary parts of the relative magnetic permeability can be evaluated up to the proportionality constant $L_X/(L_0 k^2)$. The theoretical FMR form for the complex magnetic susceptibility and its relationship to the complex permeability ($\chi = \mu_r - 1$) [71] can be used to estimate the resonant frequency, f_{FMR} , and the frequency linewidth, Δf , from experimental data:

$$\chi \propto \frac{1}{f_{FMR}^2 - f^2 + i\Delta f} \quad (4.9)$$

In order to evaluate the resonance frequencies associated with magnetic excitations (spin waves), the magnetic system Hamiltonian is written as a sum of exchange, Zeeman and dipole-dipole interaction terms. In the next step the Holstein-Primakoff diagonalization method is utilized and the Hamiltonian is cast in a form mathematically similar to that of the quantum harmonic oscillator. The resulting energy-wave vector relation reads [72]:

$$f_{SW} = \frac{|\gamma|}{2\pi} \sqrt{\left(\frac{Dk_{SW}^2}{\hbar|\gamma|} + H_{eff}\right) \cdot \left(\frac{Dk_{SW}^2}{\hbar|\gamma|} + H_{eff} + 4\pi M_S \sin^2\theta_k\right)} \quad (4.10)$$

where $|\gamma/2\pi|$ is the gyromagnetic ratio (the theoretical free-electron value is $|\gamma/2\pi| = 2.8$ MHz/Oe), k_{SW} is the wave vector associated with the spin wave mode, D

is the exchange constant, \hbar is Planck's reduced constant, $4\pi M_S$ represents the saturation magnetization and θ_k is the angle between the \vec{k} vector and the effective internal magnetic field \vec{H}_{eff} experienced by the microscopic spins: $H_{eff} = H_{DC} \pm H_K - 4\pi N_z M_S$ where H_{DC} is parallel (+) or perpendicular (-) to the sample easy axis EA, H_K is the anisotropy field and N_z is the demagnetizing factor. For the particular geometry of this experiment with all magnetic fields in the sample plane, the demagnetizing effects are insignificant, $N_z = 0$.

The ferromagnetic resonance is the uniform mode with $k = 0$ and $\theta_k = \pi/2$ ($f_{FMR} = f_{SW}$ for $k_{SW} = 0$). In the limit of small H_{DC} and anisotropy field H_K compared to the saturation magnetization $4\pi M_S$ ($H_K, H_{DC} \ll 4\pi M_S$), Eq.4.10 can be simplified and the Kittel formula for the resonance frequency, f_{FMR} , is recovered [73]:

$$f_{FMR}^2 \approx |\gamma|/2\pi|^2 4\pi M_S (H_{DC} \pm H_K) \quad (4.11)$$

With estimates of f_{FMR} extracted from numerical fits of the real and imaginary parts of μ_r acquired at various H_{DC} fields, the above linear relationship $f_{FMR}^2(H_{DC})$ allows the evaluation of H_K from the intercepts and $4\pi M_S$ from the slope of the linear fits if $|\gamma/2\pi|$ is known. Conversely, $|\gamma/2\pi|$ can be evaluated if $4\pi M_S$ has been determined from independent measurements (for example B-H hysteresis loops, as is the case here).

The experimental data acquired with the near-field microwave microscope and discussed in the next section, exhibit a feature at higher frequencies, above 5 GHz, besides the uniform mode $k = 0$ (FMR). A similar feature has been observed in

coplanar-waveguide measurements [65] and has been attributed to a perpendicular standing spin wave (PSSW) mode. The resonant frequency associated with the n^{th} order PSSW mode can be evaluated from Eq.4.10 for $\theta_k = \pi/2$, $H_{eff} = H_{DC} \pm H_K$, depending on the orientation of H_{DC} with respect to the easy axis; the spinwave vector, k_{SW} , and wavelength, λ_{SW} are related to film thickness d_0 through $k_{SW} = 2\pi/\lambda_{SW} = n\pi/d_0$. It will be shown in the next section that experimental data acquired on Py films of various thickness deposited in similar conditions can be analyzed by implementing Eq. 4.10 to yield an estimate for the exchange constant D .

The frequency linewidth Δf obtained from numerical fits based on Eq. 4.9 is typically interpreted as a combination of microwave losses and inhomogeneous broadening. The microwave losses are described by the phenomenological Landau-Lifshitz magnetic damping α while the inhomogeneous broadening, characterized by ΔH_0 , is considered the effect of magnetic inhomogeneities (spatially non-uniform anisotropy field and/or exchange interaction) [71, 74]:

$$\Delta f = \left(\frac{|\gamma|}{2\pi} \Delta H_0 + 2\alpha f_{FMR} \right) \sqrt{1 + \left(\frac{|\gamma|}{2\pi} \cdot \frac{4\pi M_S}{2f_{FMR}} \right)^2} \quad (4.12)$$

A common approach used in the literature is to neglect the effect of inhomogeneous broadening ($\Delta H_0 = 0$) and use the approximate form $\alpha \approx \Delta f / (|\gamma|/2\pi |4\pi M_S|)$.

The mathematical model for the near-field microwave microscope has been used to interpret VNA reflection data (S_{11}) and the equations describing the magnetization dynamics were implemented to fit the experimental data and extract relevant quantities.

4.4 Data analysis and discussion

The experimental set-up and the theoretical model presented in the previous sections have been used to measure and interpret data acquired with permalloy (Py) samples of various thicknesses ranging from 15 to 300 nm. First, a 100 nm thick uniaxial Py film deposited on a 6" Si wafer was FMR characterized. As mentioned previously, B-H hysteresis loops were measured with the applied field oriented parallel and perpendicular to the easy axis in order to evaluate the saturation magnetization ($4\pi M_S \approx 10789$ Oe), the coercive field ($H_{co} \approx 6$ Oe) and the anisotropy field ($H_K \approx 4.5$ Oe).

The frequency-dependent complex reflection coefficient S_{11} has been measured with the VNA in two field configurations for several values of H_{DC} as described in section §4.2. The reflection coefficient is converted into total impedance by using the standard transmission line equation:

$$Z_T(f, H_{DC}^{\parallel, \perp}) = Z_0 \frac{1 + S_{11}(f, H_{DC}^{\parallel, \perp})}{1 - S_{11}(f, H_{DC}^{\parallel, \perp})} \quad (4.13)$$

with Z_0 the coaxial cable characteristic impedance ($Z_0 = 50\Omega$). In order to separate the FMR contributions to the sample complex surface impedance, the background subtraction procedure outlined in the previous section was implemented (see Eq.4.7) and the real and imaginary components of the relative magnetic permeability μ_r have been evaluated up to a proportionality constant as shown in Eq.4.8. The theoretical form for the frequency-dependent magnetic susceptibility χ , exhibiting resonance at frequency f_{FMR} with a frequency linewidth Δf (see Eq.4.9), allows one to adjust the two fit parameters (f_{FMR} and Δf) and reproduce the experimental curves.

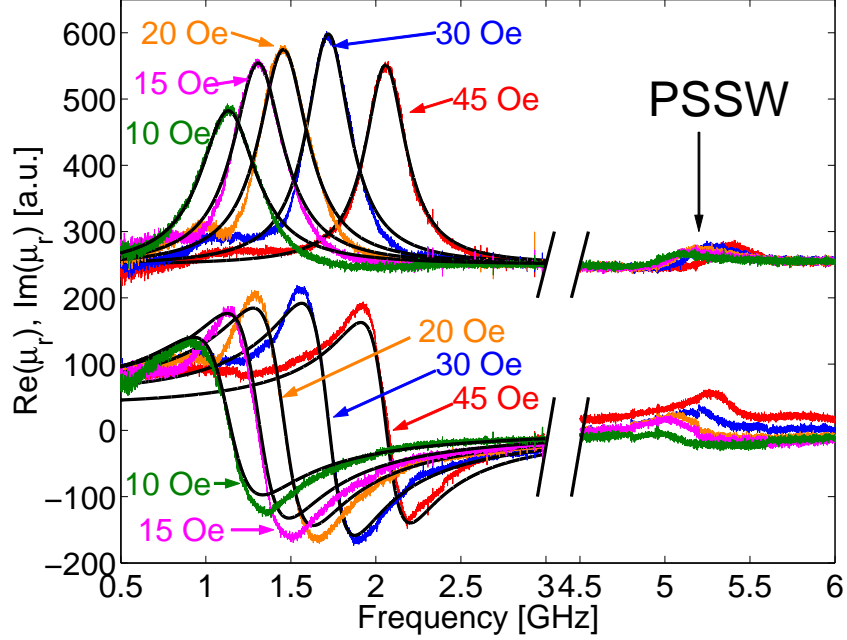


Figure 4.4: Real (bottom) and Imaginary (top) parts of magnetic permeability for the case $H_{DC} \parallel EA$ together with numerical fits (black traces). The imaginary parts have been offset for clarity [66].

Frequency-dependent relative magnetic permeability $\mu_r(f, H_{DC})$ data acquired on the 100 nm thick Py film at various magnitudes of DC field are shown in Fig.4.4. For this set of data the applied DC field was parallel to the easy axis $H_{DC} \parallel EA$. Since the proportionality constant $k^2 L_X / L_0$ from Eq.4.8 could not be determined from independent measurements or numeric simulations, the magnetic permeability data from Fig.4.4 are given in arbitrary units. The imaginary parts have been offset for clarity. Both the real and the imaginary parts resulting from experimental data have been fit with the same adjustable parameters (f_{FMR} and Δf) and the corresponding theoretical curves calculated with Eq.4.9 are shown as black traces.

The minor resonance observed at higher frequencies (above 5 GHz) is con-

sistent with measurements on similar samples by Ding et al. using a coplanar-waveguide technique and it has been associated with a perpendicular standing spin wave PSSW mode [65]. A more detailed analysis involving several samples with different thickness will be given later in this section. The results of Fig.4.4 are evidence of the sensitivity and high utility of this experimental approach to investigate a broad spectrum of magnetization dynamics.

Similar results $\mu_r(f, H_{DC})$ have been obtained when the DC magnetic field is perpendicular to the easy axis $H_{DC} \perp EA$. From the numerical fits the resonance frequencies f_{FMR} have been extracted for the two field configurations ($H_{DC} \parallel EA$ and $H_{DC} \perp EA$) and plotted in Fig.4.5 as $f_{FMR}^2(H_{DC})$ in order to fit Kittel's approximate linear formula (see Eq.4.11).

From the slope of the linear fits and the value of $4\pi M_S$ measured with the B-H loopers the gyromagnetic ratio was found, $|\gamma/2\pi| \approx 2.78$ MHz/Oe, in good agreement with the free electron value of 2.8 MHz/Oe and values for Py published in the literature [75]. From these fits, the anisotropy field H_K can be determined from the intercepts. There is a field offset in each trace that is removed by taking the difference of the data for the two field orientations. The resulting anisotropy field ($H_K = 4.78$ Oe) is within 6% of the value obtained from the B-H loopers.

The other fit parameter of the $\mu_r(f, H_{DC})$ data, the frequency linewidth, Δf , is shown in the inset of Fig.4.5 as a function of $1/f_{FMR}$. The approximate relationship $\alpha = \Delta f / (|\gamma/2\pi|4\pi M_S)$, leads to the dependence $\alpha(1/f_{FMR})$ also plotted in the inset of Fig.4.5 with green squares. Since this set of data implies a significant dependence of α on f_{FMR} , contrary to α definition as an intrinsic material-dependent parameter,

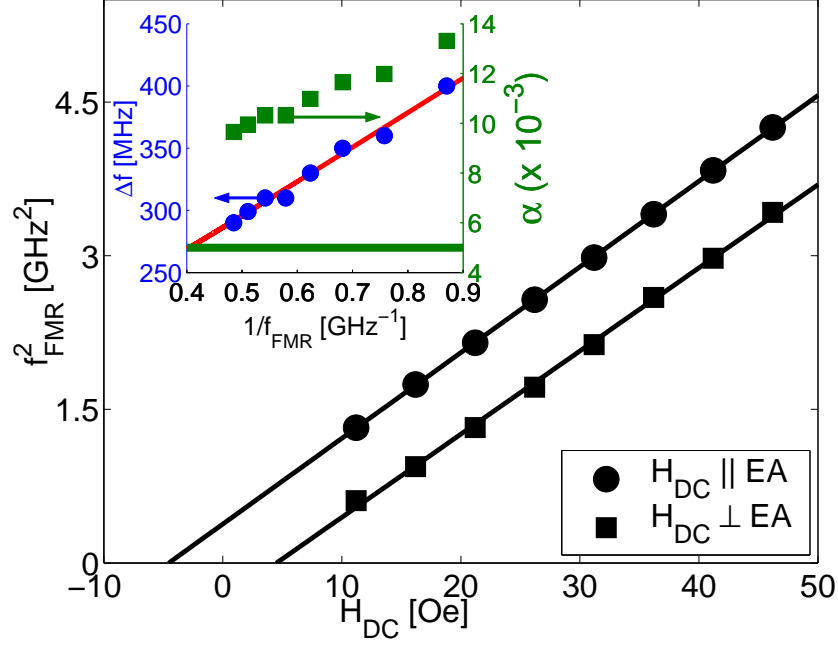


Figure 4.5: Field dependence of f_{FMR} and linear fit for the two orientations of the DC field. Inset: the f_{FMR}^{-1} dependence of the linewidth Δf , the numerical fit, α extracted from the fit (solid green line) and α extracted from $\alpha = \Delta f / (|\gamma/2\pi|4\pi M_S)$ [66].

it is concluded that the above approximation for α is not legitimate for this range of f_{FMR} . Consequently, Eq.4.12 describing the combined effect of the Landau-Lifshitz magnetic damping and that of inhomogeneous broadening has been used to evaluate α : from the fit it was found $\Delta H_0 = 6.7$ Oe and $\alpha = 0.005$ (shown in the inset of Fig.4.5 with solid green line), consistent with published results [71].

To further assess the sensitivity of the experimental setup and its applicability to realistic materials and devices, several Py films with thickness ranging from 300 to 15 nm have been FMR characterized. The samples have been deposited in similar conditions and for the microwave measurements the probe-to-sample geometric sep-

aration was roughly the same. Intuitively, one would expect that in thinner samples, the signal-to-noise ratio decreases since the microwave excitation probes a smaller sample volume. This expectation is confirmed by experiments: the imaginary part of μ_r at $H_{DC} = 50$ Oe and $H_{DC} \perp EA$ is shown in the main plot in Fig.4.6 for films as thin as 15 nm.

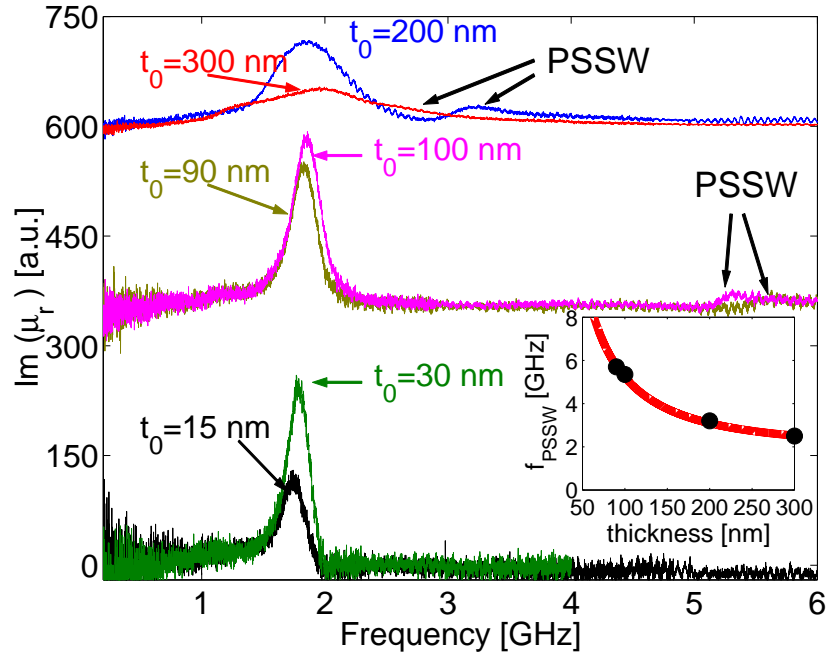


Figure 4.6: The imaginary part of the magnetic permeability for $H_{DC} = 50$ Oe, $H_{DC} \perp EA$ for Py films of different thickness (curves offset for clarity). Inset: PSSW frequency versus sample thickness and fit to theory [66].

The results of Fig.4.6 show that the signal is strong even for samples as thin as 15 nm. This suggests that the current experimental set-up can be used to investigate the magnetization dynamics in the magnetic layers of media employed in hard disk drives. Additionally, the data plotted in Fig.4.6 exhibit a minor resonance above 5 GHz also observed in the 100 nm Py disk discussed before (see the PSSW resonance

from Fig.4.4). The PSSW mode shifts to higher frequencies as the film thickness decreases so that in films with thickness $d_0 = 30$ and 15 nm it is above 6 GHz, outside the bandwidth of the vector network analyzer.

The frequency associated with the PSSW mode, f_{PSSW} , is plotted vs. film thickness in the inset of Fig.4.6. The PSSW frequency given by Eq.4.10 with $n = 1$ ($\lambda_{SW} = 2d_0$), $\theta_k = \pi/2$, and $H_{eff} = H_{DC} - H_K$ (for $H_{DC} \perp EA$), is used to fit the data of Fig.4.6 (shown in the inset) with the exchange constant D as the *only* fit parameter. The exchange constant $D \approx 5 \cdot 10^{-29}$ erg·cm² ($D/\hbar|\gamma| \approx 2.8 \cdot 10^{-9}$ Oe·cm²) estimated from the numerical fit (shown as the solid red curve in the inset of Fig.4.6) is in reasonably good agreement with other measured values on Py [76].

The FMR peak acquired on thick films $d_0 = 200$ and 300 nm (see Fig.4.6) exhibit a broadening due to the eddy currents and the availability of other spin-wave modes. This effect becomes more obvious in situations where for the operating frequencies, the microwave skin depth δ_{sk} approaches the sample thickness d_0 [77].

In summary, the near-field microwave microscope and the new microwave probe described here proved to be an appropriate tool to investigate a broad range of magnetization dynamics in Py samples as thin as 15 nm.

4.5 Magnetization dynamics of perpendicular media

With the advent of perpendicular magnetic recording, there is increased interest in developing a nondestructive instrument for media characterization both independently and in realistic settings. The technique described in this chapter and

validated on Py films has been utilized to investigate the magnetization dynamics in media from commercial hard disk drives.

The media for perpendicular recording contain a magnetically soft layer located underneath the storage layer called soft underlayer SUL (see Fig.4.7).

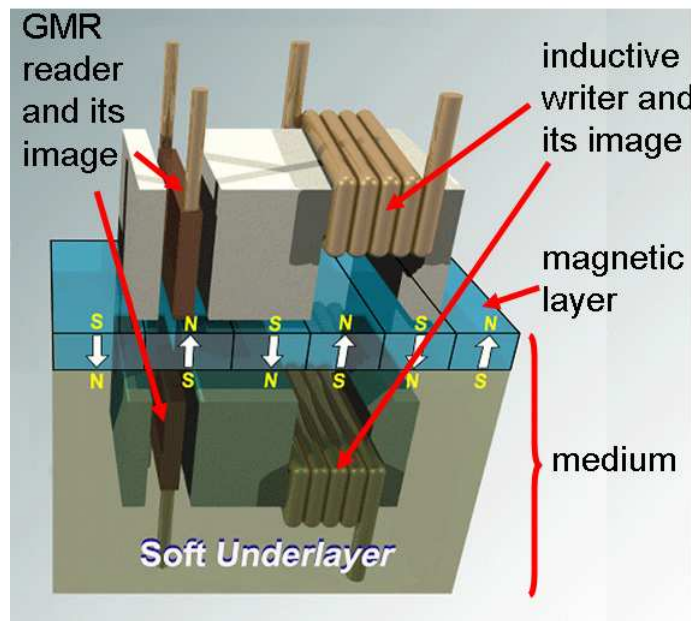


Figure 4.7: Schematic of the perpendicular magnetic recording. The magnetic layer retains the magnetization due to its high anisotropy field H_K while the soft underlayer serves as a return path for the magnetic flux emanating from the writer. [78].

Having a high magnetic permeability, the SUL provides a return path for the magnetic flux emanating from the write head. Additionally, if the magnetic permeability of the SUL is assumed infinite, the currents in the write head are "mirrored" in the SUL and are modeled by a second write head (see Fig.4.7) [78, 79]; therefore the storage layer is subject to a write field almost double in magnitude

as compared to the situation encountered in longitudinal magnetic recording. For more details on magnetic recording the reader is referred to [79].

In the absence of external magnetic fields and shape anisotropy, a soft magnetic material has an associated FMR frequency in the low GHz range (see Eq.4.11) which suggests that with the current data rates in magnetic recording exceeding the Gbps threshold, the frequency response of the SUL may become an issue for the future advance of perpendicular recording. Since the SUL in a PMR medium is subject to magnetic fields emanating from the media layer, it is important to characterize its frequency behavior by measuring FMR in a real PMR medium.

Such a characterization cannot be performed optimally with a Magneto-Optic Kerr Effect (MOKE) instrument, which is the only local nondestructive probing technique, because the optical penetration depth ($\delta_{optical} \ll 50$ nm) is relatively small and consequently its probing range hardly extends beyond the storage layer (typically with thickness in the range of 10-30 nm). However, since the microwave penetration depth in the materials of interest ($\delta_{sk} > 100$ nm) is large enough, the near-field microwave microscope is a promising tool to measure physical parameters that cannot typically be measured on disk.

The experimental set-up used to investigate the magnetization dynamics in permalloy thin films has been utilized to measure FMR effects on disks employed in perpendicular recording. While at Seagate Pittsburgh I started to perform measurements on several disks in order to detect FMR signatures of the SUL. A set of preliminary data is shown in Fig.4.8 and exhibits clear indications of resonance shifting to higher frequencies as the applied DC field is increased, in qualitative

agreement with Kittel's formula.

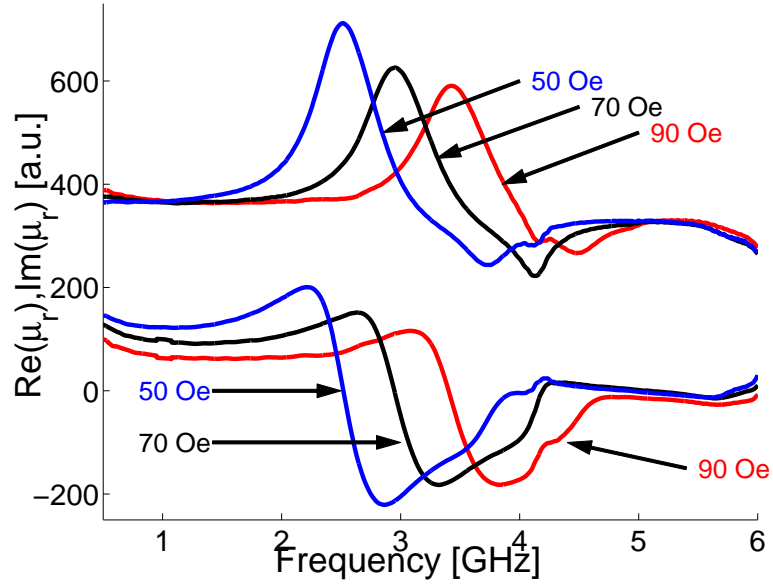


Figure 4.8: Preliminary measurements on a perpendicular medium for various values of $H_{DC} \parallel EA$. The imaginary parts have been offset for clarity.

Measurements on perpendicular media have been continued by Nadjib Benatmane[†] with an Anritsu 37369D vector network analyzer with 40 GHz bandwidth. In this section, data acquired on two PMR disks are reported. The SUL of disk1 is an 88 nm thick FeCo alloy, with $H_K \approx 10$ Oe (measured by MOKE), and $4\pi M_S \approx 1.1$ T (measured by Vibrating-Sample Magnetometer, VSM), while the SUL of disk2 is a 240 nm thick FeCo alloy, with $H_K \approx 30$ Oe, and $4\pi M_S \approx 1.8$ T.

The experimental procedure and data processing follow the steps outlined previously: the reflection coefficient S_{11} is measured with the VNA for the two orientations of the external DC magnetic field ($H_{DC} \parallel h_{MW}$ and $H_{DC} \perp h_{MW}$),

[†]PhD student in the Department of Physics, Georgetown University, Washington DC, also working with Dr. Thomas W. Clinton at Seagate Research, Pittsburgh PA.

where the background signal is acquired for $H_{DC} \parallel h_{MW}$. (referred in this section as *field-nulled* background). An additional background subtraction algorithm has been introduced, where the reflection coefficient S_{11} is measured in the FMR-active field configuration ($H_{DC} \perp h_{MW}$) but with a disk that has been prepared identically except that the SUL is left out (referred in this section as *disk-nulled* background).

The measurements have been performed over a large range of DC fields applied parallel and perpendicular to the easy-axis of the SUL which is oriented in the radial direction in a PMR medium from a hard disk drive. The real and imaginary parts of the magnetic permeability measured with $H_{DC} \parallel EA$ on disk1 are shown in Fig.4.9. To obtain the data represented in the main plot the disk-nulled subtraction scheme has been used.

The disks for the measurement were DC-erased (uniformly magnetized) in order to ensure a uniform magnetization in the magnetic layer and to facilitate data interpretation. FMR measurements have been performed also after AC-erasure (demagnetized), where the magnetization in the magnetic layer is randomly oriented. The effect of the erasure type on the FMR data will be investigated in a future work.

A comparison of the two subtraction algorithms is shown in the insets of Fig.4.9: the field-nulled subtraction results in a 25 % smaller signal. This has been attributed to a possible misalignment between the sample easy axis and the two DC field orientations [80]. Similar measurements and analysis have been done for disk2.

The real and imaginary parts of the magnetic permeability shown in Fig.4.9 have been both fitted with the same set of adjustable parameters f_{FMR} and Δf , as explained in detail in the previous section, and the Kittel linear dependence

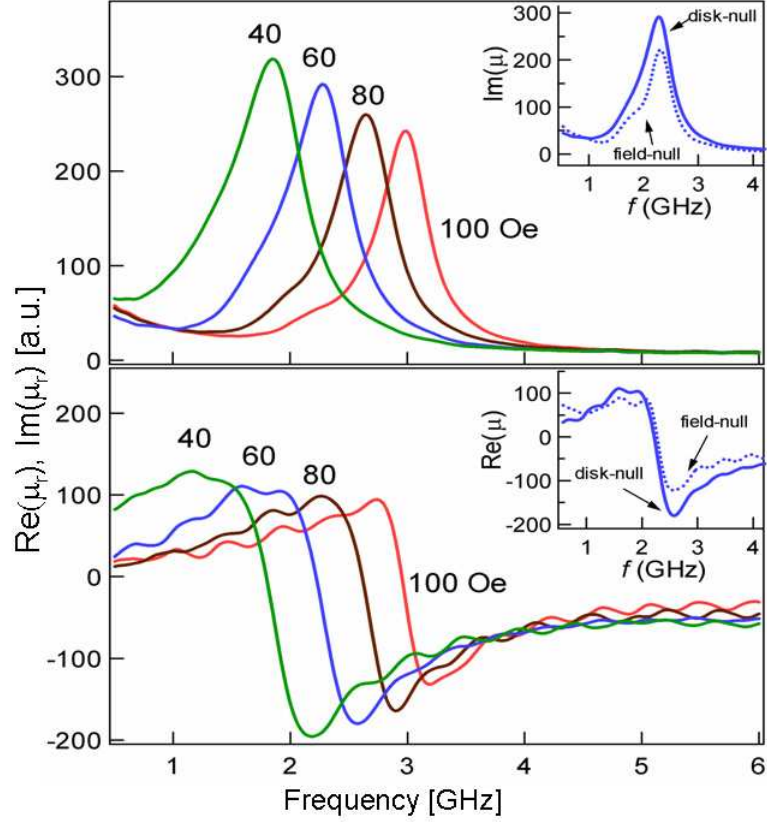


Figure 4.9: FMR for the SUL of perpendicular disk1. (top) Imaginary part of permeability vs frequency at various applied fields, $H_{DC} \parallel EA$; (bottom) Real part of permeability. Insets: comparison of background-subtraction methods. [80].

$f_{FMR}^2(H_{DC})$ has been plotted in Fig.4.10 for disk1 and disk2 (inset) for the two field orientations $H_{DC} \parallel EA$, $H_{DC} \perp EA$ together with the theoretical linear dependence (solid lines).

From the linear fits, the anisotropy field H_K can be determined from the intercepts by taking the difference of the data for the two field orientations in order to compensate for the field offset in each trace. The resulting anisotropy field for disk1, $H_K \approx 7$ Oe, and disk2, $H_K \approx 31$ Oe, are close to values obtained from MOKE (for disk1: $H_K \approx 10$ Oe while for disk2: $H_K \approx 30$ Oe). The gyromagnetic ratio

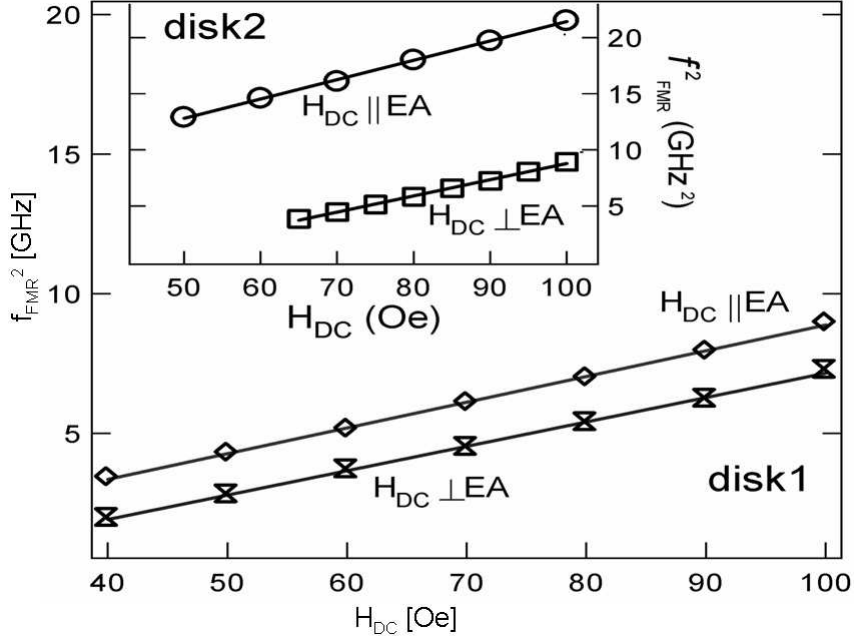


Figure 4.10: Field dependence of the resonance frequency f_{FMR} and theoretical fit for disk1. Inset: results for disk2 [80].

$|\gamma/2\pi|$ has been calculated by using the slope and the VSM measurement of $4\pi M_S$. The resulting values ($|\gamma/2\pi| = 2.86$ MHz/Oe for disk1, $|\gamma/2\pi| = 2.96$ MHz/Oe for disk 2) are in reasonable agreement with values reported in the literature and the free-electron value ($|\gamma/2\pi| = 2.8$ MHz/Oe).

4.6 Conclusions and future work

A versatile technique for the high-frequency characterization of perpendicular media directly on disk has been demonstrated. The novel non-contact local microwave probe has high sensitivity and allows FMR measurements by using a commercial vector network analyzer. Due to the local nature and the high sensitivity of the measurements, a wide variety of materials and sample geometries can be

characterized. From measurements of the microwave reflection coefficient in permalloy films several quantities have been successfully extracted: the FMR frequency, the gyromagnetic ratio, the anisotropy field, damping parameter, and the exchange constant. Additionally, perpendicular media have been investigated where the FMR frequency, anisotropy field, and saturation magnetization have been evaluated, all in good agreement with independent measurements. The measurements on perpendicular media have shown that the proposed technique gives access to quantities that cannot be effectively measured on a disk due to sample-size constraints with microwave resonating techniques, modest signal-to-noise ratio with MOKE and the difficulty to generate the necessary radial (easy-axis) or circumferential (hard-axis) fields with magnetometers.

It was shown that the proposed technique has sensitivity comparable to that of well-established methods. The microwave probe can be further optimized for higher sensitivity and spatial resolution as well as for larger bandwidth. By using smaller coaxial transmission line and by defining the field-enhancing feature of the probe (the Cu micro-loop) with Focused-Ion-Beam (FIB), higher signal-to-noise ratio and improved spatial resolution can be achieved. Additionally, by reducing the length of the coaxial transmission line from the connector to the probe, one can "push" the associated geometrical resonances to higher frequencies allowing the exploration of magnetization dynamics beyond 6 GHz.

In order to investigate the media layer, high DC external fields are required (> 1 T); at present, fields of this magnitude are outside the range of the experimental set up. A more advanced mathematical treatment would be necessary to interpret

data acquired on the media layer due to its high anisotropy field: Kittel equation must be replaced with a more accurate one and the skin depth effects must be taken into account at high frequencies.

Chapter 5

Scalar measurements of the microwave nonlinear response of high- T_c superconductors

quod est inferius est sicut quod est superius;
et quod est superius est sicut quod est inferius, ad
perpetranda miracula rei unius[†].

The Plate of the Emerald Table

Kunrath, H. *Amphitheatrum SapientiæÆternæ*,

Hanau, 1609

5.1 Introduction and motivation

The two ingredients required for the presence of macroscopic superconducting properties (the absence of DC resistance, the Meissner effect, etc.) are electron pairing and the existence of long-range phase coherence among the electron pairs. The energy scales governing these processes are the electron-electron binding energy and the phase stiffness of the order parameter which depends on the density of paired electrons n_S . The competition between the energies associated with Cooper pair unbinding, phase unlocking and thermal fluctuations determines the temperature where the onset of macroscopic superconducting properties occurs (the critical tem-

[†]that which is above is from that which is below, and that which is below is from that which is above, working the miracles of one. *Translated by Sir Isaac Newton*

perature T_c) [6, 81]. For the case of conventional superconductors the energy scales characterizing the two superconductivity ingredients are similar and therefore the loss of long-range phase coherence among Cooper pairs is accompanied by depairing, the two effects being almost indistinguishable.

The situation in high- T_c superconductors is different because these materials are doped insulators and consequently they have smaller carrier densities than the conventional superconductors. In underdoped high- T_c superconductors, the energy associated with the phase stiffness is lower compared to that in the optimally-doped ones (due to the reduced density of paired charge carriers n_S) and simultaneously the binding energy Δ_p is higher [81, 5]. For this reason, in underdoped cuprates the macroscopic superconducting properties disappear at lower T_c as the doping level is reduced but the electron pairing mechanism is thought to be active up to higher temperatures (up to 100 K above the critical temperature [81]). In this context, some authors have suggested that preformed Cooper pairs above T_c might be responsible for the large Nernst effect observed in hole-doped cuprates [11, 9]. If the existence of short-coherence-range evanescent Cooper pairs above T_c is associated with the pseudogap, the aforementioned behavior is consistent with the phase diagram of cuprates. In the language of the phenomenological Time-Dependent Ginzburgh-Landau (TDGL) theory the lifetime of Cooper pairs in the normal state τ_0 in underdoped materials is expected to be higher than that in the optimally-doped ones [11]. Signatures of the enhanced τ_0 detected in experiments on underdoped materials could be considered good support for the above picture.

This chapter providing experimental data, theoretical interpretations and nu-

merical estimates of relevant quantities are an attempt to fill this gap. First, a more complete model of nonlinear effects at T_c is provided. By implementing this model, microwave harmonic data ($P_{3f}(T)$) acquired on YBCO thin films with a wide range of doping can be interpreted. Second, from the model a fundamental constant of the TDGL theory is extracted: the order parameter relaxation time for the $k = 0$ mode, which is interpreted as the lifetime of fluctuation Cooper pairs τ_0 above the critical temperature T_c [29].

The chapter is organized as follows: In section §5.2 the samples used for this study are described and experimental data are provided. In section §5.3 the traditional model of inductive nonlinearities in the superconducting state is briefly reviewed. The model of electric field-dependent conductivity of a layered material [29] is introduced and re-formulated in a fashion similar to that of inductive nonlinearities below T_c . Section §5.4 contains the analysis of the microwave harmonic data and provides numerical estimates for the doping-dependent lifetime of Cooper pairs in the normal state τ_0 . Section §5.5 presents an analysis of the doping dependence of τ_0 and section §5.6 summarizes the main conclusions of this analysis.

5.2 Experimental procedure and sample description

The experimental set-up employed for the scalar harmonic measurements has been presented in detail in section §3.4. The samples are c-axis oriented $\text{YBa}_2\text{Cu}_3\text{O}_{7-\delta}$ (YBCO) thin films deposited on SrTiO_3 and NdGaO_3 substrates by pulsed laser deposition PLD with thicknesses in the range from 90 to 200 nm (see Table 5.1). The

Table 5.1: Sample properties: film thickness d_0 , critical temperature T_c^{AC} and spread δT_c^{AC} as determined from AC susceptibility measurements, the corresponding doping level $7 - \delta$, in- and out-of-plane coherence length $\xi_{ab}(0)$, $\xi_c(0)$ and the interpolated doping-dependent resistivity parameters \bar{a} , \bar{b} , $T^\#$. To reproduce $\rho(T, 0)$ for samples MCS4 and MCS1 a variable range hopping term $\rho_1 \exp[(T_0/T)^{1/4}]$ has been included with $T_0 = 10^5$ K and $\rho_1 = 0.41 \mu\Omega\text{cm}$ as described in [82].

Sample	d_0 nm	T_c^{AC} [K]	δT_c^{AC} [K]	$7 - \delta$	$\xi_{ab}(0)$ [Å]	$\xi_c(0)$ [Å]	\bar{a} a[$\mu\Omega\text{cmK}^{-1}$]	\bar{b} b[$\mu\Omega\text{cm}$]	$T^\#$ [K]
MCS4	95	54.15	1.7	6.52	29.0	0.47	5.47	-554.3	175.0
MCS1	132	63.1	1.3	6.68	28.0	0.42	4.14	-326.42	497.0
MCS50	96	74.2	1.3	6.76	26.5	0.55	2.135	-61.58	683.76
MCS2	185	83.96	1.3	6.81	23.0	0.72	1.36	-6.77	574.0
MCS3	130	90.5	0.7	6.84	18.0	0.86	0.97	1.24	441.06

oxygen content of the samples has been modified by annealing in various oxygen pressures and at different temperatures [83, 84] resulting in critical temperatures T_c^{AC} in the range of 52 to 90 K as observed in AC susceptibility measurements (see Table 5.1).

In Table 5.1 a description of the five samples used for this study is given. Film thicknesses have been estimated from the PLD deposition conditions and the critical temperature T_c^{AC} and the spread δT_c^{AC} from AC susceptibility measurements. Based on the critical temperature T_c^{AC} the doping level $7 - \delta$ has been approximately calculated by using the experimental data of Carrington *et al.*, which have been

acquired on thin films and single crystals [85] (see Fig.5.1a). As is shown later in this chapter, the doping level $7 - \delta$ and the other quantities given in Table 5.1 are ingredients required for numerical estimations.

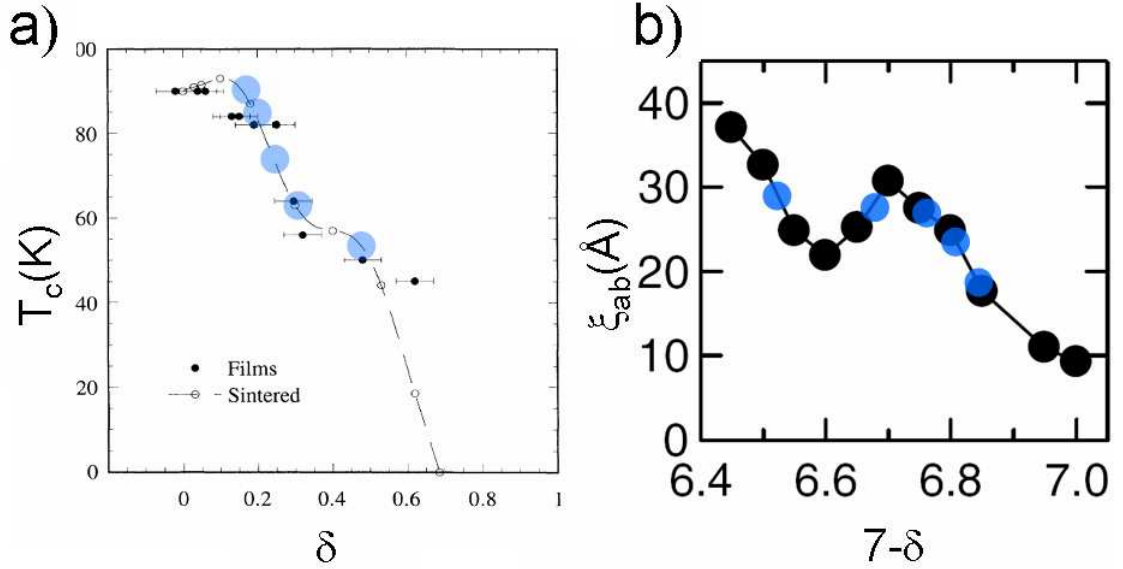


Figure 5.1: Experimental data used to evaluate the doping level $7 - \delta$ and the zero-temperature in-plane coherence length $\xi_{ab}(0)$ for the samples discussed in this chapter. a) Doping dependence of the critical temperature T_c from the Hall effect and resistivity measurements (reproduced from Ref.[85]). b) Doping dependence of the in-plane coherence length ξ_{ab} from magnetoresistance data of Ando *et al.*, (reproduced from Ref.[86]). The semi-transparent blue dots correspond to the samples used in the experiments discussed in this chapter.

By using the doping level $7 - \delta$ deduced previously, one can use the experimental data of Ando and Segawa [86] to obtain the doping dependence of the in-plane coherence length $\xi_{ab}(0)$ (see Fig.5.1b). In addition, the theoretical fit of Leridon and co-workers allows one to reproduce numerically the temperature dependence of the

in-plane zero-field DC conductivity $\sigma(T, 0)$ in the vicinity of the critical temperature T_c for various levels of oxygen doping [82]:

$$\sigma(T, 0) = \frac{1}{\bar{a}T + \bar{b}} + \frac{e_0^2}{16\hbar\xi_c(0)\sqrt{2\epsilon_0 \sinh(2\epsilon/\epsilon_0)}} \quad (5.1)$$

where the coefficients \bar{a} and \bar{b} govern the temperature dependence of the mean-field component (the first term in Eq.5.1) while $\epsilon_0 = \ln(T^\# / T_c)$, $T^\#$ and $\xi_c(0)$ determine the strength of the superconducting fluctuations (the second term in Eq.5.1). $T^\#$ is a temperature scale introduced in [82] to describe the upper temperature limit of the superconducting fluctuations, $\xi_c(0)$ represents the zero-temperature out-of-plane coherence length, $\epsilon = \ln(T/T_c)$, e_0 is the electron charge and \hbar is Planck's reduced constant. The doping-dependent coherence length $\xi_c(0)$ and the other parameters (\bar{a} , \bar{b} and $T^\#$) required to reproduce the temperature dependence of the zero-electric-field DC conductivity $\sigma(T, 0)$ have been estimated by interpolating the parameters published by Leridon and co-workers for YBCO [82].

The experiment consists in controlling the temperature in the cryostat and monitoring the reflected power carried by the third-order harmonic signal $P_{3f}(T)$ with the spectrum analyzer. A set of experimental $P_{3f}(T)$ data is shown in Fig. 5.2 for an underdoped YBCO thin film with $T_c^{AC} \approx 63$ K. Similar sets of data acquired on samples with various doping levels are shown in Fig. 5.3. The first observation is the presence of the peak of $P_{3f}(T)$ which spans over a significant power range (~ 45 dB dynamic range for the data in Fig. 5.2) when the temperature is swept through T_c^{AC} .

The second observation is that the shape of the $P_{3f}(T)$ peak is doping-dependent:

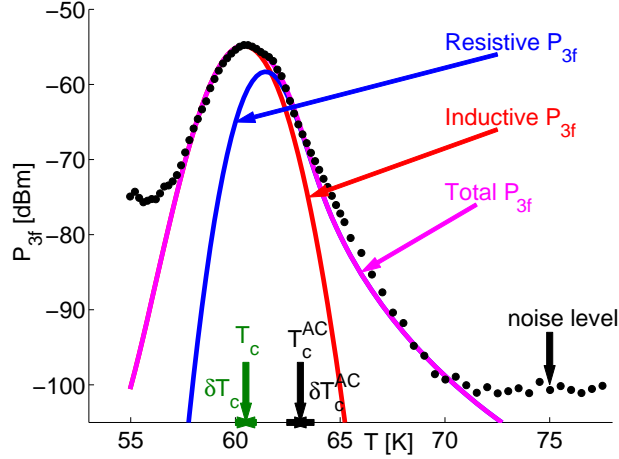


Figure 5.2: Experimental data and numerical fit for an underdoped $\text{YBa}_2\text{Cu}_3\text{O}_{6.84}$ thin film with fit central $T_c = 60.5$ K (see Table 5.1). The experimental data ($\bullet\bullet$) and the calculated inductive ($-$), resistive ($-$) and total ($-$) nonlinear response are shown. The harmonic resistive contribution is required in order to reproduce the temperature dependence of $P_{3f}(T)$ in the pseudo-gap region. T_c^{AC} and δT_c^{AC} together with their counterparts estimated from the numerical fit are shown for comparison.

in optimally-doped samples ($T_c^{AC} \approx 90$ K) the $P_{3f}(T)$ peak drops abruptly into the noise level as soon as T_c^{AC} is slightly exceeded (see Fig. 5.3b), while in underdoped samples there is a persistence of the harmonic response at temperatures above T_c^{AC} , suggesting that some of the features of the superconducting state are preserved in the pseudogap phase. The most obvious continuation of the harmonic power $P_{3f}(T)$ into the pseudogap phase is exhibited by the data shown in Fig. 5.2.

Experiments have been carried out for several microwave input power levels ranging from +6 to +12 dBm and at various locations of the sample with consistent

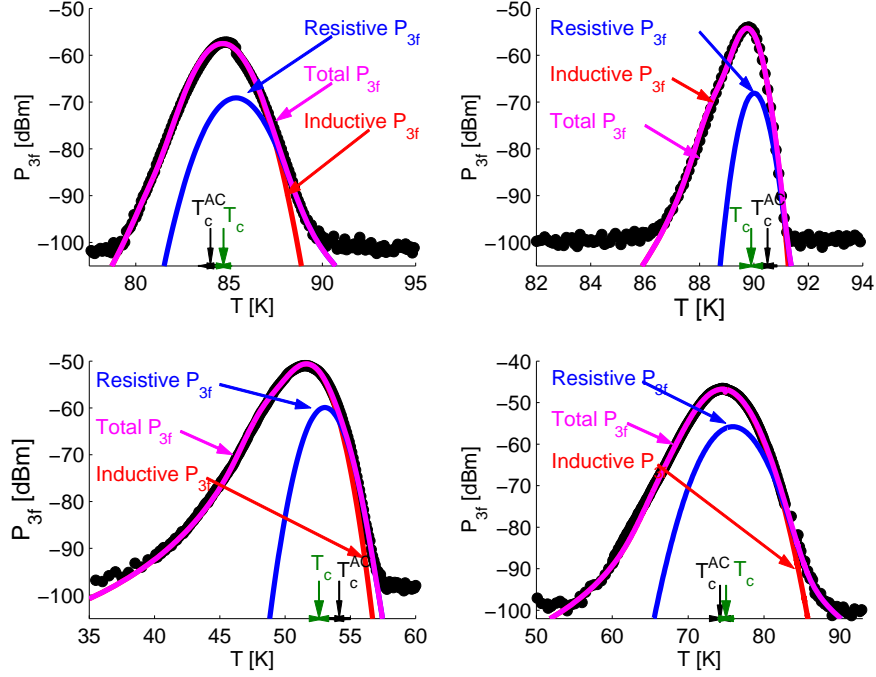


Figure 5.3: Experimental data ($\bullet\bullet$) and numerical fit for the $\text{YBa}_2\text{Cu}_3\text{O}_{7-\delta}$ thin films from Table 5.1 with various doping. The calculated inductive (—), resistive (—) and total (—) nonlinear response are shown. The near-optimally doped sample, $T_c^{AC} \approx 90$ K, requires no resistive nonlinear contribution to obtain a good fit for the measured harmonic power. T_c^{AC} and δT_c^{AC} together with their counterparts estimated from the numerical fit are shown for comparison.

results. The power dependence $P_{3f} \sim P_{input}^3$ observed at all temperatures[†] agrees with the predictions of the model (given in the next section) and suggests that the superconducting sample is in the weakly-nonlinear regime. The probe does not cause a significant local heating of the sample, as confirmed by sets of data acquired with the same input frequency but various power levels (from +6 to +12 dBm) which

[†]For the experimental set-up used in this study and the microwave power levels employed here, the relation $P_{3f} \sim P_{input}^3$ has been extensively investigated and confirmed by S. C. Lee in Ref.[45].

exhibit no shift of the $P_{3f}(T)$ peak at lower temperatures for higher input power levels, as would be expected if the probe were heating locally the sample.

In Fig. 5.2 and Fig. 5.3 the experimental data is accompanied by theoretical curves calculated using a model of the nonlinear behavior in superconductors. This model is presented in detail in the next section and the evaluations of the theoretical curves require the sample parameters given in Table. 5.1.

5.3 Theoretical model of the microwave nonlinear response at T_c

The interest in the microwave nonlinear behavior of superconductors has been renewed after the discovery of the high- T_c materials and is driven by its twofold aim: the investigation of the fundamental physics governing the superconducting state and the optimization of high- T_c superconducting microwave filters used in the wireless industry.

The theoretical work on superconducting filters (Dahm & Scalapino, [26]) shows that under certain specific conditions, an inductive nonlinear source dominates the overall nonlinear behavior: the suppression of the superfluid density by the external field. Following this line of thought, microwave harmonic data acquired on YBCO thin films in the vicinity of T_c have been interpreted by implementing a Ginzburg-Landau-like GL model (see section §2.3.2) and the corresponding nonlinear effects have been considered mainly inductive in nature [45]. The experimental evidence suggested that such a picture is accurate in optimally-doped cuprate thin films [45]. However, in underdoped samples the measured harmonic response

$P_{3f}(T)$ does not turn off at the independently determined T_c as expected from the GL model, but exhibits a tail extending significantly above T_c in the pseudogap regime (see Fig. 5.2). An additional nonlinear source has to be considered in the normal state in order to model the continuation of microwave harmonic response above T_c .

The first step in understanding the temperature- and doping dependence of the microwave nonlinear effects at T_c is to treat separately the two temperature regimes, below and above T_c . The theoretical model presented in this chapter considers that in the superconducting state the inductive nonlinearities described by the nonlinear Meissner effect dominate the overall response. At T_c this inductive mechanism shuts off and it is replaced by a current-dependent normal-state resistivity that generates the harmonic effects observed above T_c .

5.3.1 Inductive nonlinear response below T_c

The modeling of the harmonic data has been done by using the phenomenological formalism outlined in section §2.3.2, where a temperature-dependent characteristic nonlinear current density scale, $J_{NL}(T)$, is introduced in order to quantify the suppression of the superfluid density n_S and the enhancement of the penetration depth $\lambda^2(T, J)$ by the current density J :

$$\frac{n_S(T, J)}{n_S(T, 0)} = \frac{\lambda^2(T, 0)}{\lambda^2(T, J)} \approx 1 - \left(\frac{J}{J_{NL}(T)} \right)^2, \quad J \ll J_{NL}(T) \quad (5.2)$$

where $J_{NL}(T)$ has been evaluated by using a Ginzburg-Landau approach: $J_{NL}(T) = J_c(1 - t^2)(1 - t^4)^{1/2}$ and J_c is the zero-temperature critical current density. The em-

pirical two-fluid model has been employed to model the zero-current magnetic penetration depth: $\lambda(T, 0) = \lambda_0(1 - t^4)^{-1/2}$. As shown in previous works on microwave nonlinear effects [26, 41, 42, 43, 44], the field(current)-dependent penetration depth given in Eq.(5.2) leads to third-order harmonic generation; the corresponding P_{3f} is inductive in nature since it originates from a current-dependent kinetic inductance.

The limitations of this picture have been discussed in §2.3.2 (DC treatment, not valid very close to T_c due to the vanishing $J_{NL}(T_c)$, no fluctuation effects included, etc.) become more obvious as one notices that the linear-response penetration depth $\lambda(T, 0)$ diverges at T_c while the phenomenological characteristic nonlinear current density scale $J_{NL}(T)$ vanishes. One way to circumvent these mathematical difficulties is to introduce finite phenomenological cut-off values $\lambda(T_c)$ and $J_{NL}(T_c)$ as was done by Lee and co-workers [44]. The cut-off parameters are motivated by the inadequacy of the model arbitrarily close to T_c where the phenomenological description of the Nonlinear Meissner Effect breaks down due to the violation of the condition $J \ll J_{NL}(T)$ in Eq.5.2. Additionally, very close to T_c the critical superconducting fluctuations are active and the order parameter fails to follow adiabatically the external microwave excitation.

The mathematical model starting with Eq.5.2 and leading to the corresponding reactive (inductive) power $P_{3f}(T)$ measured by the spectrum analyzer has been presented in detail in [45]: the total inductance of the sample is evaluated as the ratio of the electromagnetic energy stored in magnetic fields and currents and the square of the total current induced in the sample. From the current-dependent penetration depth one can isolate the current-dependent kinetic inductance and evaluate the

associated voltage and microwave power. In the limit of samples thinner than the zero-temperature penetration depth ($d_0 \ll \lambda(T = 0K)$), as is the case for the data presented in this chapter, the harmonic power due to the current-dependent kinetic inductance is [45]:

$$P_{3f}(T) = \left(\frac{\omega \mu_0 \lambda^2(T)}{4d_0^3 J_{NL}^2(T)} \right)^2 \cdot \frac{\Gamma^2}{2Z_0} \quad (5.3)$$

where Γ is the figure of merit describing the sensitivity of the experimental set-up to nonlinearities and it was defined and evaluated numerically in section §3.3.

5.3.2 Resistive nonlinear response above T_c

A nonlinear source acting at and above T_c that may explain the observed high-temperature tail of the harmonic data $P_{3f}(T)$ is the electric field-dependent conductivity $\sigma(T, E)$. There is clear evidence that the microwave conductivity ($\tilde{\sigma} = \sigma_1 - i\sigma_2$) of under-doped and optimally-doped YBCO above T_c is primarily real ($\sigma_1 \gg \sigma_2$) [15]. Hence a contribution from the nonlinear component of σ_2 above T_c was not considered in this model.

The effect of fluctuations on the nonlinear response of superconductors has been discussed in section §2.3.2. For a layered superconductor (e.g. cuprates), a theoretical model for the electric field-dependent conductivity has been proposed by Mishonov and co-workers [29]. Within this model, the effect of Gaussian fluctuations leads to an E^2 correction to the zero-field Lawrence-Doniach conductivity [87], and describes the destruction of fluctuation Cooper pairs by the applied electric field

[29]:

$$\sigma(T, E) = \sigma(T, 0) - \mathcal{A}(T)E^2 + \dots, T > T_c \quad (5.4)$$

where the coefficient $\mathcal{A}(T)$ determining the strength of the nonlinear resistive effects was evaluated for a layered superconductor by using the TDGL formalism [29] and is discussed later in this subsection.

According to Eq.(5.4), for strong enough electric fields and within the appropriate temperature range, nonlinear effects in the real part of the conductivity become significant. The magnitude of the electric field required to generate nonlinear effects can be estimated by re-writing Eq.(5.4) in terms of a characteristic nonlinear electric field scale E_{NL} (in the isotropic case other authors call it $\widetilde{E}_0(\epsilon)$, the characteristic depairing electric field [28, 88, 89]) which vanishes at T_c due to the divergence of the correction coefficient $\mathcal{A}(T)$:

$$\frac{\sigma(T, E)}{\sigma(T, 0)} \approx 1 - \left(\frac{E}{E_{NL}(T)} \right)^2 + \dots, E \ll E_{NL} \quad (5.5)$$

with $E_{NL}(T) = (\sigma(T, 0)/\mathcal{A}(T))^{1/2}$. For the described experimental configuration the magnitude of the electric field E generated by the loop probe in the plane of the sample was evaluated numerically [59] and compared with the theoretical temperature-dependent $E_{NL}(T)$: the ratio $E/E_{NL}(T)$ is smaller than unity for $T > 0.5K + T_c$, so Eq.(5.5) can be re-formulated in terms of the electric field-dependent resistivity:

$$\frac{\rho(T, E)}{\rho(T, 0)} \approx \frac{1}{1 - \mathcal{A}(T)\rho(T, 0)E^2} \approx 1 + \mathcal{A}(T)\rho(T, 0)E^2 + \dots \quad (5.6)$$

For the above range of temperatures the higher-order terms can be neglected in the expansion (5.6). Additionally, if the electric field is approximated by its

linear regime value ($J = \sigma(T, 0)E - \mathcal{A}(T)E^3 + \dots \approx \sigma(T, 0)E$) the resistivity can be written in terms of the current density J in a fashion similar to Eq.(5.2) which described the nonlinear effects due to the suppression of the superfluid density:

$$\frac{\rho(T, J)}{\rho(T, 0)} \approx 1 + \left(\frac{J}{J_{NL\rho}(T)} \right)^2, J \ll J_{NL\rho}(T) \quad (5.7)$$

Similar to the nonlinear current density scale $J_{NL}(T)$ from Eq.5.2 to characterize the inductive nonlinear effects below T_c , a nonlinear current density scale $J_{NL\rho}(T)$ has been introduced in Eq.5.7 in order to quantify the strength of the resistive nonlinear effects in the normal state. For small electric fields ($E \ll E_{NL}$), $J_{NL\rho}(T)$ can be estimated as:

$$J_{NL\rho}(T) = [\mathcal{A}(T)\rho^3(T, 0)]^{-1/2} \quad (5.8)$$

The current-dependent resistivity defined by Eq.(5.7) generates the tail of $P_{3f}(T)$ above T_c as observed in harmonic measurements of underdoped YBCO thin films and is resistive in nature. The effect of the current density J is to break the fluctuation Cooper pairs persisting above T_c (equivalent to the effect of the electric field on conductivity in Eq.(5.4)) and to increase the resistivity in the normal state.

The coefficient $\mathcal{A}(T)$ has been evaluated for a layered superconductor by Mishonov and co-workers [29]:

$$\mathcal{A}(T) = \frac{4k_B T e_0^4 [\xi_{ab}(0)\tau_0]^3}{\pi \hbar^4 s \xi_{ab}(0)} \cdot \frac{\epsilon^3 + \frac{3}{2}r\epsilon^2 + \frac{9}{8}r^2\epsilon + \frac{5}{16}r^3}{(\epsilon(\epsilon + r))^{7/2}} \quad (5.9)$$

where $\xi_{ab}(0)$ and $\xi_c(0)$ represent the zero-temperature in- and out-of-plane coherence lengths, and r represents the anisotropy coefficient ($r = (2\xi_c(0)/s)^2$, where s is the interlayer spacing).

The essential ingredient of the field-dependent conductivity model is τ_0 , representing the time scale for the lifetime of fluctuation Cooper pairs in the normal state $\tau^G(\epsilon) = \tau_0/\epsilon$ in the formalism of Gaussian fluctuations [29]. If the Cooper pairs persist above T_c , τ_0 must be very small as suggested by the absence of macroscopic superconducting properties above T_c . The Cooper pair lifetime τ_0 can be estimated within the framework of BCS theory [29]:

$$\tau_0^{BCS} = \frac{\pi}{16} \cdot \frac{\hbar}{k_B T_c} \quad (5.10)$$

For a superconductor with $T_c = 90$ K as is the case for near optimally-doped YBCO thin films, $\tau_0^{BCS} \approx 1.05 \cdot 10^{-13}$ s. Equation (5.10) shows that the product $\tau_0^{BCS} \cdot T_c$ is a material-independent universal constant that can be used to check the estimates of τ_0 from our experimental data.

Similar to the calculation of the inductive harmonic power $P_{3f}(T < T_c)$ in a lumped-element approach [45], for the resistive component of $P_{3f}(T > T_c)$ the sample total electrical resistance is written as the ratio between the dissipated power and the square of the total current induced in the sample $I_0 = \int \int J dS$:

$$R = \int_{SL} \frac{\int \int J^2 \rho dS}{(\int \int J dS)^2} dy \quad (5.11)$$

where the y integration is evaluated for the sample length (SL) and $dS = dx dz$ represents the infinitesimal surface element in the cross-section direction with respect to the microwave screening current (in the XOZ plane, see Fig.3.1 in section §3.2).

By plugging the current-dependent resistivity, Eq.(5.7) one can split the above equation into a linear and a nonlinear component characterized by the nonlinear

current density scale $J_{NL\rho}(T)$:

$$R = \int_{SL} \frac{\int (J^2 \cdot \rho(T, 0) + \frac{J^4}{J_{NL\rho}^2(T)} \rho(T, 0)) dS}{(\int \int J dS)^2} dy \quad (5.12)$$

The first term represents the current-independent ohmic resistance R_0 , while the second one represents the current-dependent component of resistance $\Delta R I_0^2$:

$$R = \int_{SL} \frac{\int J^2 \cdot \rho(T, 0) dS}{(\int J dS)^2} dy + \int_{SL} \frac{\int \frac{J^4}{J_{NL\rho}^2(T)} \rho(T, 0) dS}{(\int J dS)^2} dy \quad (5.13)$$

Thus, the total electrical resistance reads:

$$R(I_0) = R_0 + \Delta R \cdot I_0^2 \quad (5.14)$$

with

$$\Delta R = \frac{1}{I_0^2} \cdot \frac{\rho(T, 0)}{J_{NL\rho}^2(T)} \cdot \int_{SL} \frac{\int \int J^4 dS}{(\int \int J dS)^2} dy \quad (5.15)$$

If an AC current $I(t) = I_0 \cos \omega t$ is applied to the current-dependent resistance $R(I)$ the resulting voltage is[†]:

$$V(t) = R_0 I_0 \cos \omega t + \frac{1}{3} \left(\Delta R \frac{3}{4} I_0^3 \cos \omega t + \Delta R \frac{1}{4} I_0^3 \cos 3\omega t \right) \quad (5.16)$$

since

$$\cos^3 \omega t = \frac{3}{4} \cos \omega t + \frac{1}{4} \cos 3\omega t \quad (5.17)$$

The first two terms in Eq.5.16 represent the voltage at the fundamental frequency while the third term represents the third-order harmonic of the voltage. It is the third term in Eq.(5.16) that is responsible for the generation of $P_{3f}(T > T_c)$, a quantity that is measured with the nonlinear near-field microwave microscope.

[†]For a current-dependent resistor $R(I) = R_0 + \Delta R I_0^2$ the associated voltage is $V = \int R(I) dI$

Eq.(5.16) shows that the presence of the 3rd order harmonic has an impact on the voltage at the fundamental frequency. Similarly, if a 5th order harmonic voltage is considered (originating from a I_0^4 term in Eq.5.14), there will be corrections both in the voltage at the fundamental frequency as well as in that at the 3rd order harmonic. However, experimentally it is observed that $P_{3f} \sim P_{input}^3$ at all temperatures, suggesting that the sample is in the weakly-nonlinear regime. In a strongly-nonlinear regime the scaling relation $P_{3f} \sim P_{input}^3$ is violated and additionally, the harmonics generate intermodulation distortion products (IMD) as discussed in section §2.3.1 (for example, f and $3f$ would generate $3f \pm f$). The measurements presented here are all in the weakly-nonlinear regime, as confirmed by the scaling $P_{3f} \sim P_{input}^3$ valid at all temperatures (see footnote on page 102). The third-order harmonic power generated at the sample surface is:

$$P_{3f}(T > T_c) = \frac{|U_{3f}(T)|^2}{2Z_0} = \frac{1}{2Z_0} \left(\frac{1}{9 \cdot 16} \Delta R^2 I_0^6 \right) \quad (5.18)$$

where Z_0 is the characteristic impedance of the transmission line. By using the expression for ΔR given by eq.(5.15), $P_{3f}(T)$ can be obtained:

$$P_{3f}(T > T_c) = \frac{1}{2Z_0} \cdot \frac{1}{16} \cdot \frac{1}{I_0^4} \cdot \frac{\rho^2(T, 0)}{J_{NL\rho}^4(T)} \cdot \left[\int_{SL} \frac{\int \int J^4 dS}{(\int \int J dS)^2} dy \right]^2 \cdot I_0^6 \quad (5.19)$$

Since the sample thickness d_0 is much smaller than the normal metal microwave skin depth depth of the sample in the normal state, the current density J is uniform within the sample thickness. As a consequence, the integrals involving the current density J can be simplified:

$$\int \int J^4 dS = \int \frac{K^4}{d_0^4} d_0 dx \quad (5.20)$$

$$I_0 = \int \int J dS = \int \frac{K_y}{d_0} d_0 dx = \int K_y dx \quad (5.21)$$

The new expression for $P_{3f}(T > T_c)$ is:

$$P_{3f}(T > T_c) = \frac{1}{2Z_0} \cdot \frac{1}{9 \cdot 16} \cdot \frac{\rho^2(T, 0)}{J_{NL\rho}^4(T)} \cdot \frac{1}{d_0^6} \cdot \left[\int_{SL} \frac{\int K^4 dx}{\int K_y dx} dy \right]^2 \quad (5.22)$$

Similar to the formalism developed for the superconducting state, a figure of merit Γ_ρ is defined in order to characterize the sensitivity of the probe and sample to nonlinearities above T_c (see also section §3.3):

$$\Gamma_\rho = \int_{SL} \frac{\int_{-x_0}^{x_0} K^4 dx}{\int_{-x_0}^{x_0} K_y dx} dy = \frac{\int \int K^4 dx dy}{\int_{-x_0}^{x_0} K_y dx} \quad (5.23)$$

To obtain this equation, one has to notice that the total current induced in the sample by the probe is $I_0 = \int \int J dS = \int K_y dx$. The integral $\int K_y dx$ is the same if evaluated in every $y = \text{constant}$ plane since there is no source of electric charge and the current density is divergence-free; thus it behaves like a constant in the integrand and can be taken outside the integral. The third-order harmonic power $P_{3f}(T > T_c)$ becomes:

$$P_{3f}(T > T_c) = \frac{1}{288Z_0} \cdot \frac{\rho^2(T, 0)}{J_{NL\rho}^4(T)} \cdot \frac{1}{d_0^6} \cdot \Gamma_\rho^2 \quad (5.24)$$

This expression can be compared to that of the third-order harmonic power $P_{3f}(T < T_c)$ originating from the current dependence of the penetration depth below T_c :

$$P_{3f}(T < T_c) = \frac{1}{32Z_0} \cdot \frac{\omega^2 \mu_0^2 \lambda^4(T, 0)}{j_{NL}^4(T)} \cdot \frac{1}{d_0^6} \cdot \Gamma^2 \quad (5.25)$$

Both figures of merit Γ and Γ_ρ computed numerically with CST Microwave Studio [59] vary as $P_{input}^{3/2}$ and consequently, the above equation for the harmonic

power predicts a dependence $P_{3f} \sim P_{input}^3$ which was observed experimentally for all the samples and over the entire temperature range.

It has to be noted that the resistive and inductive harmonic power, given by Eq.5.24 and Eq.5.25 exhibit significantly different frequency dependences: in a first approximation, neglecting the frequency dependence of the figures of merit Γ_ρ and Γ , the inductive harmonic power $P_{3f}(T < T_c)$ increases quadratically in ω while the resistive harmonic power $P_{3f}(T > T_c)$ is constant with frequency which suggests a possible avenue for separating the two contributions to the total measured $P_{3f}(T)$. The frequency dependence has been investigated with a vector network analyzer with harmonic detection capabilities (operating in the frequency offset mode, VNA-FOM) as described in the next chapter. Due to the small frequency range ($f = 6.45 - 6.55$ GHz) imposed by the instrumentation[†] the results of the measurements were inconclusive.

The above treatment of the current-dependent resistivity above T_c has several limitations. First, the model, as originally formulated by Mishonov and co-workers [29], is essentially a DC treatment that describes the time-averaged effect of the fluctuating nonzero GL order parameter $\langle |\Psi|^2 \rangle$ associated with the Cooper pairs on the electrical conductivity. Thus, the model is valid only for those temperatures

[†]The experimental set-up is described in detail in section §3.5. The circuit element that mostly limits the bandwidth is a band-pass filter with optimal transmission at 19.5 GHz and 3 GHz FWHM inserted in the reference path and designed to suppress all microwave power except for that at frequency $3f$, where $f \sim 6.5$ GHz. In addition, there is the frequency dependence of the harmonic output of the comb generator from the reference path as well as the effect of the other filters from the circuit that made the data interpretation cumbersome.

where the dynamics of the Cooper pairs is faster than that associated with the time scale of the probing electromagnetic field ($\tau(\epsilon) < 1/f, f = 6.5$ GHz). As is shown in the next section, this condition is valid in the temperature range used in the numerical fit, but violated for very small ϵ (in very close proximity to T_c). Second, very close to T_c ($\epsilon < 2 \cdot 10^{-2}$ in optimally-doped YBCO thin films [90]) critical fluctuations are thought to dominate the electromagnetic response of superconductors. The above treatment includes only the effect of Gaussian fluctuations on the field-dependent conductivity in the normal state and therefore very close to T_c the dependence $\tau^G(\epsilon) = \tau_0/\epsilon$ could be replaced with a temperature dependence more appropriate for a regime characterized by critical fluctuations. Due to these approximations, the nonlinear current density scale defined previously, $J_{NL\rho}(T)$, vanishes at T_c as is the case of $J_{NL}(T)$. Thus, the mathematical divergence of $P_{3f}(T)$ has been eliminated by introducing a phenomenological cut-off parameter $J_{NL\rho}(T_c)$.

The expressions for the third-order harmonic power in the case of inductive and resistive nonlinearities are valid for ideal, uniform samples which have the same T_c at every location (mathematically this would correspond to a delta-Dirac $\delta(T_c)$ distribution of T_c s). In order to employ the $P_{3f}(T)$ equations and to estimate the realistic harmonic response of a sample, it is necessary to convolve these expressions with a probability density function that mimics the inhomogeneous nature of the sample. Within an effective medium approximation [91], the local critical temperature is a random variable with a Gaussian distribution centered on $\overline{T_c}$ and a spread δT_c , $\mathbb{G}(\overline{T_c}, \delta T_c)$. Both inductive and resistive components of the measured $P_{3f}(T < T_c, T > T_c)$ have been smeared out with the same Gaussian kernel defined

by the adjustable parameters \overline{T}_c and δT_c .

The disadvantage arising from the non-ideal probe-to-sample coupling is compensated somewhat by using microwave amplifiers with a gain $G \approx 52$ dB (as measured with a vector network analyzer at frequency $3f$ [45]). Since the inductive and resistive harmonic powers are in quadrature, the total power, measured with the spectrum analyzer reads:

$$|P_{3f}(T)| = G \cdot k^2 \cdot \sqrt{\left(\int P_{3f}(T < T_c) \mathbb{G}(\overline{T}_c, \delta T_c) dT_c \right)^2 + \left(\int P_{3f}(T > T_c) \mathbb{G}(\overline{T}_c, \delta T_c) dT_c \right)^2} \quad (5.26)$$

where k is the probe-to-sample electromagnetic coupling coefficient[†] and the integrals are evaluated over a temperature range centered on \overline{T}_c with width $20\delta T_c$. This fitting expression represents a generalization of that employed by Lee [45] and it has been implemented in Mathematica.

Despite the apparent complexity, the numerical fit is reliable due to some features of the expression (5.26): on the increasing side of the $P_{3f}(T)$ peak (in the superconducting state), the inductive harmonic power dominates since $P_{3f}(T > T_c) = 0$. This allows one to neglect the second term in Eq.(5.26) and perform the fit by using a pure inductive harmonic power, as was done previously by Lee [45]. On the decreasing side of the $P_{3f}(T)$ peak (in the pseudogap state), the resistive harmonic power dominates since $P_{3f}(T < T_c) = 0$ and consequently, one fits the other side of the $P_{3f}(T)$ peak with a pure resistive harmonic component. This is the rationale behind the plots from Figs.5.2 and 5.3 where theoretical curves for the

[†]quantity defined and evaluated in section §3.3

individual inductive, resistive and total power are shown.

5.4 Data analysis

Several YBCO thin films with characteristics given in Table.5.1 have been investigated by using the nonlinear microwave near-field microscope. Harmonic data $P_{3f}(T)$ have been numerically fit by using the model presented in the previous section. Despite a relatively significant range of doping levels the fit is very accurate over a large dynamical range of harmonic power $P_{3f}(T)$ (about 45 dB). From the numerical fit several parameters of the samples have been extracted: the critical depairing current density J_c from the inductive harmonic power in the superconducting state $P_{3f}(T > T_c)$ and the Cooper pair lifetime τ_0 in the pseudogap state.

In a first step of data processing the harmonic data $P_{3f}(T)$ have been fit by using a pure inductive nonlinear mechanism as was done by Lee [45]. In near optimally-doped samples only the inductive component is required to successfully reproduce the trend of P_{3f} over the entire temperature range as illustrated in Fig. 5.3b where data acquired with an optimally-doped YBCO sample ($T_c \approx 90$ K) is shown. In underdoped YBCO samples it was observed that by simply adjusting the parameters of the Gaussian distribution ($\overline{T_c}$ and δT_c) the inductive component alone cannot reproduce the measured temperature dependence of P_{3f} below and above T_c due to the asymmetry of the $P_{3f}(T)$ peak (see Fig.5.2 for the most obvious case). For this reason, in a second data processing step, both the inductive and the resistive nonlinear mechanisms and their associated harmonic power have been considered in

order to reproduce the entire temperature dependence of P_{3f} for all doping levels. Therefore, the theoretical resistive, inductive and total $P_{3f}(T)$ are plotted separately in Fig.5.2 and 5.3.

The theoretical inductive component $P_{3f}(T < T_c)$ has several adjustable parameters: $J_c(0)$ and the cut-off phenomenological parameters $\lambda(T_c)$ and $J_{NL}(T_c)$ (see Table.5.2). Additionally, to model the inhomogeneous nature of the samples, the parameters of the Gaussian distribution ($\overline{T_c}$ and δT_c) have been determined from the inductive component $P_{3f}(T < T_c)$ and used also for the resistive component $P_{3f}(T > T_c)$. The Cooper pair lifetime above T_c , τ_0 , is the *only* fit parameter for the resistive contribution, $P_{3f}(T > T_c)$, since the cut-off parameter $J_{NL\rho}(T_c) = 3 \cdot 10^9$ A/m² was fixed for all samples (see Table.5.2).

Despite the fact that the inductive component alone gives a good numerical fit of the harmonic data on optimally-doped samples (see Fig.5.3b, for $T_c \approx 90$ K), a small resistive contribution has been added to the inductive component in order to obtain an estimate of the upper limit for the magnitude of the resistive effects. Thus, harmonic data $P_{3f}(T)$ acquired on optimally-doped YBCO samples suggest that the Gaussian fluctuations in the normal state play a minor role in the microwave nonlinear response.

As mentioned previously, in underdoped YBCO samples the inductive component alone cannot reproduce the measured temperature dependence of P_{3f} below and above T_c . The tail of P_{3f} extending into the normal state can be explained only by introducing the nonlinear mechanism associated with the current-dependent resistivity. In Fig.5.2 data are shown together with the calculated curves representing

the inductive and the resistive contributions as well as the total harmonic power. For the underdoped samples the resistive component has a contribution comparable to the inductive one and the extracted values for the lifetime of fluctuation Cooper pairs τ_0 depart significantly from the theoretical values predicted by Eq.(5.10) as will be discussed in the next section.

5.5 Discussion

Since this study is focused on the electrodynamics of the Cooper pairs above the critical temperature, a detailed discussion of the evaluated lifetime τ_0 and its doping dependence is given in this section. For the investigated samples the estimates for τ_0 follow a consistent trend with doping (see Fig.5.4): departures from the optimal doping level lead to higher τ_0 suggesting that in underdoped cuprates the fluctuating GL order parameter $\langle |\Psi|^2 \rangle$ is nonzero in a significant range of temperatures above T_c .

The comparison between the universal value $\tau_0^{BCS} \cdot T_c$ (see Eq.(5.10)) and the ones calculated with the experimental τ_0^{exp} and T_c is shown in Fig. 5.4. Based on this comparison it can be concluded that underdoped cuprates do not behave in a BCS-like fashion, being characterized by unusually high lifetimes of the fluctuation Cooper pairs τ_0 . For the case of the optimally-doped YBCO thin films the product $\tau_0^{exp} \cdot T_c$ seems to deviate very little from the universal value. However, it must be noted that the fit of the resistive part covers about 1 K above the mean-field T_c and it is possible that critical fluctuations are dominant in this temperature range and

Sample	T_c [K]	δT_c [K]	λ_0 [nm]	$\lambda(T_c)$ [μm]	$J_c(0)$ [A/m ²]	$\frac{J_{NL}(T_c)}{J_c(0)}$	τ_0 [ps]
MCS4	52.6	0.9	286	0.95	$1.4 \cdot 10^{10}$	0.075	0.226
MCS1	60.5	1.0	254	3.6	$8.8 \cdot 10^{10}$	0.019	0.16
MCS50	75.0	2.2	222	1.6	$1.3 \cdot 10^{10}$	0.07	0.124
MCS2	84.7	0.9	189	5.3	$6.9 \cdot 10^{10}$	0.02	0.095
MCS3	89.9	0.3	120	1.5	$15 \cdot 10^{10}$	0.007	0.0214

Table 5.2: Fit parameters for the nonlinear resistive component $P_{3f}(T)$ in a series of $YBa_2Cu_3O_{7-\delta}$ thin film samples. For all samples the interlayer separation was considered $s = 4.3 \text{ \AA}$. The cutoff value $J_{NL\rho}(T_c) = 3 \cdot 10^9 \text{ A/m}^2$ is the same for all samples.

consequently the proposed model, and in particular the $\tau^G(\epsilon) \sim 1/\epsilon$ dependence, might not be valid. This is suggested by microwave measurements performed by Booth *et al.*, [90] where it was shown that the above Gaussian approximation for $\tau^G(\epsilon)$ is not accurate for $\epsilon < 2 \cdot 10^{-2}$ in optimally-doped YBCO thin films. For the case of the underdoped samples the fit of the resistive part involves a 5-15 K temperature interval above T_c and therefore, the model of Gaussian fluctuation-driven conductivity should be applicable.

The doping dependence of the τ_0 estimates resembles that of the pseudogap temperature T^* as given by the phase diagram of cuprates [92]. The hole concentration in the Cu_2O planes p has been evaluated by using the empirical law $T_c/T_c^{optimal} = 1 - 82.6(p - 0.16)^2$ as in Ref. [4] and the doping-dependent pseudogap temperature T^* was calculated with $T^* = 805(1 - p/0.19)K$ according to Tallon *et*

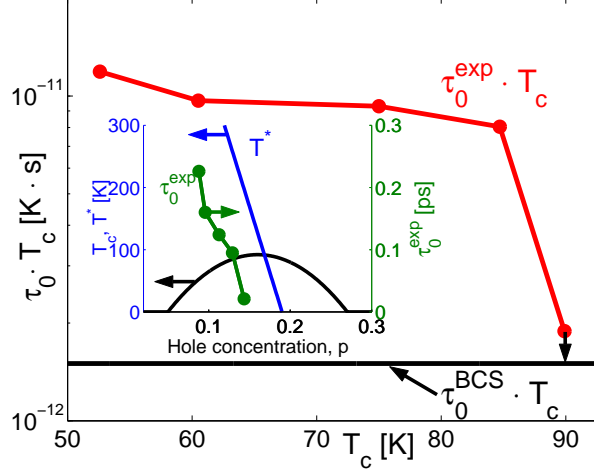


Figure 5.4: The product $\tau_0 \cdot T_c$ obtained from experimental evaluations of the Cooper pair lifetime $\tau_0^{exp} \cdot T_c$ (-●-) and the theoretical value $\tau_0^{BCS} \cdot T_c$ (-) provided by Eq.5.10. Inset: the temperature-doping phase diagram of cuprates and the doping dependence of T_c (-), T^* (-) and τ_0^{exp} (-●-).

al. [92]. In the inset of Fig. 5.4 the doping dependence of the critical temperature T_c , pseudogap temperature T^* and τ_0 is represented. At optimal doping T^* almost coincides with the critical temperature T_c ; similarly, τ_0^{exp} is very close to the BCS value. As the doping level is decreased the values of T^* increase and so do our evaluations of τ_0^{exp} with respect to their BCS counterparts.

Based on estimates for E_0 extracted from experimental measurements on $\text{Bi}_2\text{Sr}_2\text{Ca}_{n-1}\text{Cu}_n\text{O}_{2n+4+x}$ ($n=1,2$) thin films some authors [88] have proposed a reduction of the characteristic depairing electric field E_0 from its theoretical value ($E_0 = 16\sqrt{3}k_B T_c / (\pi e_0 \xi_0)$). Smaller effective values of E_0 result also due to the smearing of the transition as shown by numerical simulations of Seto *et al.*, [89]. In our model, E_{NL} depends on τ_0 and consequently is an adjustable parameter in the

numerical fit. This approach follows Ref. [29] and is in agreement with Ref. [28] where E_0 was defined in terms of τ_0 ($E_0 = \hbar/(2e\xi_0\tau_0)$) and the relaxation rate of the order parameter Γ_0 ($E_0 = \sqrt{12}\Gamma_0/(em\xi^3)$ with ξ the mean-field correlation length), respectively. Our estimates for τ_0^{exp} in underdoped YBCO thin films are about one order of magnitude higher than their theoretical BCS counterparts τ_0^{BCS} and lead to values of E_0 lower than the expected ones.

The parameters extracted from the fit and the maximum current density induced in the sample ($\sim 10^4$ A/cm²) computed with the electromagnetic solver have been used to estimate the sensitivity of the experimental set-up for changes in conductivity due to the current density J : $\Delta\sigma(T, J)/\sigma(T, 0) = 1 - \sigma(T, J)/\sigma(T, 0)$. For the temperatures where the measured harmonic response $P_{3f}(T)$ reaches the noise-floor, an estimate for the ultimate sensitivity of the experiment is $\Delta\sigma(T, J)/\sigma(T, 0) \approx 10^{-4}$.

The theoretical model of the electric field-dependent conductivity in layered superconductors [29] used here to explain the harmonic effects above T_c was formulated for the DC case and consequently it captures the time-averaged effect of the fluctuation Cooper pairs on conductivity. Evaluating the $\tau^G(\epsilon) = \tau_0/\epsilon$ dependence to T_c shows that in the measurements reported here the decay of the fluctuation Cooper pairs is fast with respect to the probing electromagnetic field ($f=6.5$ GHz) for $T > T_c + 0.3$ K. This suggests that the model is applicable for the temperature range considered in the numerical fit of the normal state harmonic microwave response.

5.6 Conclusions

In summary, this chapter presents a unified model for the microwave nonlinear response of cuprate superconductors which describes accurately the temperature dependence of the third-order harmonic power $P_{3f}(T)$ in a large dynamic range (~ 45 dB), below and above the critical temperature. Within the new model, the nonlinear Meissner effect is active in the superconducting state and leads to inductive harmonic effects $P_{3f}(T < T_c)$, while in the normal state the E^2 correction to the zero-field fluctuation conductivity is responsible for resistive harmonic effects $P_{3f}(T > T_c)$. Both nonlinear effects are described by nonlinear current scale densities which quantify their strength within the appropriate temperature domains. The third-order harmonic signals P_{3f} originating from the field(current)-dependent superfluid density ($T < T_c$) and resistivity ($T > T_c$) are in quadrature and can, in principle, be measured with a large-signal vector network analyzer. In the next chapter, similar YBCO thin films have been investigated with a vector network analyzer with harmonic capabilities which provides an additional piece of information: the phase of the third-order harmonic voltage with respect to the excitation signal. This requires a more sophisticated estimate of the 3^{rd} harmonic voltage $U_{3f}(T)$ going beyond the simple approximation of Eq.5.26.

The proposed model and the harmonic data allows one to obtain estimates for the lifetime of Cooper pairs in the normal state τ_0 which show significant departures from the BCS predictions especially for the case of underdoped samples. The observed consistent trend of τ_0 with the doping level suggests that τ_0 might be

(cor)related with the pseudogap temperature T^* .

Chapter 6

Vector measurements of the nonlinear response of high- T_c superconductors

Door meten tot weten. †

Heike Kammerlingh Onnes' motto

6.1 Introduction and motivation

Scalar harmonic data acquired on YBCO thin films with various oxygen doping levels have been presented and interpreted in the previous chapter. The harmonic behavior of the cuprate samples has been modeled in a somewhat artificial fashion in the sense that the critical temperature T_c was used as a sharp border between a pure inductive regime, below T_c , and a pure resistive one, above T_c . Additionally, the formalism developed in the previous chapter is a DC treatment since the following frequency-dependent effects have not been considered:

1. in the superconducting state the penetration depth λ has been approximated with the London value λ_L . Essentially, the electrodynamics of the normal fluid together with possible nonlinear effects have been neglected and the frequency that marks the crossover from Meissner screening to skin depth screening, Ω_1 ,

†By measurements to knowledge

was assumed infinite;

2. in the superconducting state the relaxation time scale governing the dynamics of the order parameter, Ω_0^{-1} , was considered zero. In this picture the order parameter adiabatically follows the external field up to arbitrarily high frequencies;
3. in the normal state, the dependence of the real part of conductivity on the electric field was described within a DC theoretical treatment.

The approach from the previous chapter serves as a first approximation: under the influence of a high-frequency field that suppresses the superfluid (as the nonlinear Meissner effect describes), the normal fluid is enhanced, participates in the diamagnetic screening process and could, in principle, generate nonlinear effects detectable in a phase-sensitive experiment.

The crucial experimental improvement that made possible a deeper level of analysis was the replacement of the spectrum analyzer with a vector network analyzer with harmonic detection capabilities. This way, a new piece of information, in addition to the harmonic power P_{3f} , was accessible: the phase of the harmonic voltage U_{3f} generated by the superconducting sample.

First, in section §6.2 the experimental procedure is described in detail due to the novelty of the microwave phase-sensitive harmonic technique and analogies with harmonic measurements with the spectrum analyzer are made. The samples investigated by means of phase-sensitive harmonic detection are described in section §6.2, and examples of raw and processed experimental data are shown. A novel theoretic-

cal model of the near-field microwave microscope is presented in section §6.3 which links the measured quantity, the complex-valued harmonic voltage, to the physical quantities describing the linear and nonlinear electrodynamics of the superconducting sample. It is shown that the mathematical expression for the harmonic power from the previous chapter, describing nonlinear effects in the superconducting state can be recovered from the new model in the limit of low temperatures. A discussion of the data and model and their agreement follows in section §6.4.

6.2 Experimental procedure, samples and data

Experimental procedure A measurement consists in exciting the superconducting sample with a single-tone microwave signal at frequency f generated from the VNA's port 1, and tuning the receiver on port 2 in a narrow frequency range (1 or 2 Hz) centered on the harmonic frequency of interest, $3f$, in this case (see Fig.3.5). This procedure is similar to the one performed with the spectrum analyzer, where one acquires traces representing the absolute power incident on the input port (in dBm units) vs. frequency. The VNA in the frequency offset mode (VNA-FOM) outputs a string of complex numbers (trace) representing the $U_{3f}^{sample}/U_{3f}^{ref}$ ratio evaluated at the frequency points scanned by the receiver. At each temperature a trace is acquired and is stored on the acquisition PC for further processing.

Examples of such traces are shown in Fig.6.1 where a YBCO thin film, called XUH157, has been probed with an incident microwave signal with frequency $f = 6.49$ GHz and power of 5 dBm. The VNA receiver settings were selected for the

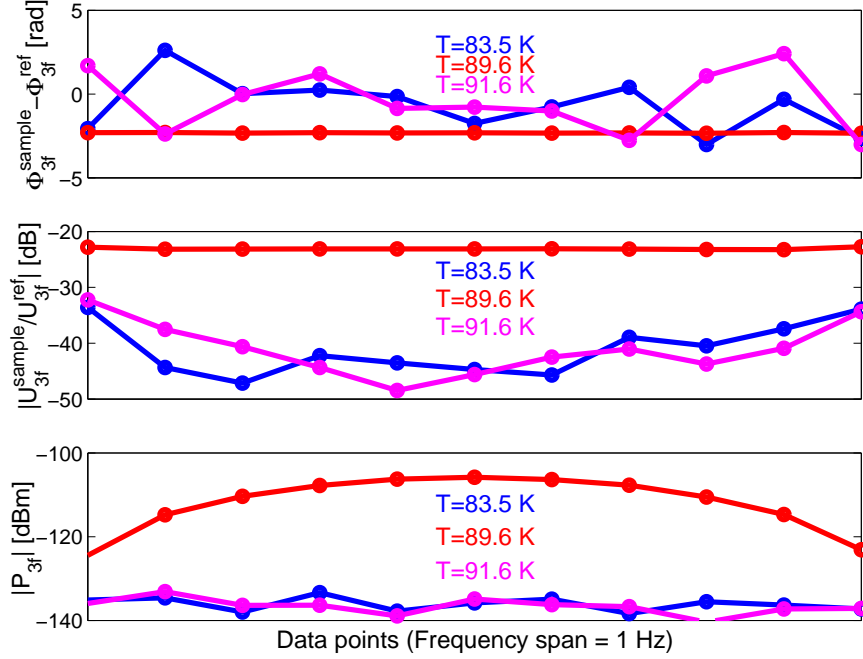


Figure 6.1: Examples of VNA-FOM traces acquired on a YBCO thin film (XUH157) in a frequency range centered on $3f = 19.47$ [GHz]. Top and middle plot: the phase and magnitude of $U_{3f}^{sample}/U_{3f}^{ref}$ acquired in a phase-sensitive measurement; bottom plot: absolute harmonic power data $P_{3f}(T)$ of the sample.

maximum signal-to-noise ratio in a reasonable acquisition time: the frequency range scanned by the receiver on port 2 was 1 Hz with 11 frequency sampling points and an IF bandwidth of 1 Hz. A small IF bandwidth ensures a low background noise but requires a large acquisition time, and for this reason the frequency range scanned by the VNA receiver has been chosen to be 1 Hz.

Similar to the measurements on a spectrum analyzer, on the VNA-FOM a number of frequency sweeps, or averages (8 for the data plotted in Fig.6.1) were performed on the VNA to increase the signal-to-noise ratio before transferring the trace to the acquisition PC. As opposed to frequency-dependent traces on a scalar

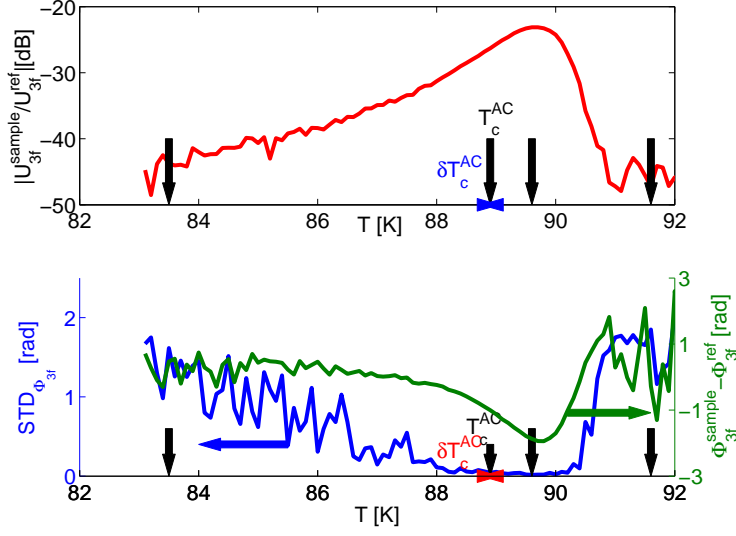


Figure 6.2: Phase-sensitive harmonic data acquired on a YBCO thin film (XUH157). Top graph: temperature-dependent magnitude. Bottom graph: temperature-dependent phase (green line) and the standard deviation of the 11-point traces acquired at each temperature (blue line). Black arrows: the temperatures where the traces from Fig.6.1 have been acquired.

spectrum analyzer, those on the VNA contain complex numbers, and the averaging procedure does not lead to a meaningful output if the data points to be averaged are scattered about the origin in the polar plot of the harmonic voltage. For this reason, the data points from the traces acquired at $T=83.5$ K and $T=91.6$ K, outside the range of the good signal-to-noise ratio, exhibit a large scatter in phase and magnitude, as shown in Fig.6.1. To quantify the data spread, the standard deviation of the phase data $STD_{\Phi_{3f}}$ from traces acquired at each temperature are plotted in Fig.6.2 (blue curve, bottom graph). These data show that $STD_{\Phi_{3f}}$ is very small only in the temperature range where the magnitude is above the noise floor (evaluated

to be ~ -135 to -145 dBm) and thus the phase data are meaningful.

After power calibration the VNA can be used as a spectrum analyzer to measure the absolute harmonic power (in units of dBm). Such traces acquired at three different temperatures are shown in Fig.6.1, bottom graph. Due to the narrow frequency range selected for the measurement (1 Hz), only the top of the $|P_{3f}(\omega)|$ peak is captured. At $T=83.5$ K and $T=91.6$ K, below and above T_c respectively, the harmonic signal produced by the sample $|P_{3f}|$ is not measurable, being obscured by the internal noise of the VNA[†].

In the phase-sensitive VNA-FOM traces acquired at temperatures of 83.5 K and 91.6 K, below and above T_c respectively, the harmonic signal produced by the sample $|U_{3f}^{sample}(T)|$ is very small (see Fig.6.1, bottom plot) and when ratioed to the reference signal $|U_{3f}^{ref}|$ results in noisy data, as seen in the magnitude and phase traces in Fig.6.1 top and bottom plots. At temperatures where the magnitude of the nonlinear effects is significant (for this particular sample, at $T = 89.6$ K) the $|U_{3f}^{sample}(T)/U_{3f}^{ref}|$ traces are smooth and higher in magnitude, while $STD_{\Phi_{3f}}$ is very small.

In order to examine the temperature dependence of the ratioed phase $\Phi_{3f}^{sample}(T) - \Phi_{3f}^{ref}$ and magnitude $|U_{3f}(T)^{sample}/U_{3f}^{ref}|$, several points from the center of the traces (Fig.6.1) acquired at each temperature are selected (typically three or five points), averaged, and the resulting complex number is assigned to the sample temperature during the VNA-FOM acquisition. The temperature-dependent magnitude and

[†]The VNA internal noise can be estimated by running a measurement without any device connected to port 2 which results in a noise floor on the order of -135 to -145 dBm

phase of the ratioed harmonic voltage $U_{3f}(T)^{sample}/U_{3f}^{ref}$ are plotted in Fig.6.2 top and bottom graph respectively. To check the robustness of the above-mentioned averaging procedure, temperature-dependent phase and magnitude obtained by using 1, 3 and 5 central trace points in the average have been compared and their agreement is good at temperatures where the signal-to-noise ratio is high (see Fig.6.2), or equivalently, where the traces are smooth (see Fig.6.1).

In chapter 3 it was shown that the ratioed harmonic voltage measured by the VNA-FOM $U_{3f}(T)^{sample}/U_{3f}^{ref}$ can be used reliably to investigate the temperature-dependent behavior of nonlinear effects in the sample since the reference path operates at constant room temperature. For this reason, in the following, the harmonic voltage measured by VNA-FOM is simply labeled $U_{3f}(T)$ and is given in relative units dB.

Samples The VNA-FOM has been used to measure the power- and temperature-dependence of the harmonic behavior of several YBCO thin films with various levels of doping. The samples' characteristics are given in Table.6.1. After PLD deposition and thermal annealing[†] to precisely adjust the oxygen content [83, 84], the critical temperature T_c^{AC} , and the width of the transition, δT_c^{AC} , have been estimated from AC magnetic susceptibility measurements. Despite their small thickness (~ 50 nm) the sample superconducting quality is very good as revealed by the narrow peaks of the temperature-dependent imaginary part of the magnetic susceptibility whose full-half width maximum δT_c^{AC} are given in Table. 6.1.

[†]The samples have been prepared by Hua Xu, PhD student in the Department of Physics, University of Maryland, College Park, MD, also working with Prof. Steven M. Anlage.

Table 6.1: Sample properties: critical temperature T_c^{AC} and transition width δT_c^{AC} determined from AC susceptibility measurements, the doping level $7 - \delta$ estimated from T_c^{AC} , the difference between the temperatures where the extreme values of the harmonic phase and magnitude occur, $\Delta T_{M,m}$, and the sample substrate.

Sample	T_c^{AC} [K]	δT_c^{AC} [K]	$7 - \delta$	$\Delta T_{M,m}$ [K]	Substrate
XUH157	88.9	0.3	6.84	-0.2	NdGaO ₃
XUH163	86.6	1.0	6.82	-0.5	NdGaO ₃
STO055	62.0	0.55	6.69	-0.6	SrTiO ₃
STO039	52.0	1.1	6.53	-1.0	SrTiO ₃

The samples have been measured by using various input frequencies (6.45 to 6.55 GHz) and power levels (0 to 9 dBm). In addition, sets of data have been acquired on the same sample with the microwave probe placed at several locations above the sample, all with consistent results.

Power dependence Sets of data measured with the probe at the same location above the sample (called STO039) and with several microwave input power levels (8, 6 and 4 dBm) are shown in Fig.6.3. The quantities plotted in Fig.6.3 are ratioed with respect to the reference voltage incident on the VNA's **Ref In** and consequently their power dependence contains intrinsically the power dependence of the sample and that of the comb generator. For this reason the heights of the ratioed magnitudes acquired with 6 and 4 dBm input power have been offset to overlap the ratioed magnitude acquired with 8 dBm, considered here as the reference. The vertical offsets, -2 and -2.7 dB, for the magnitude curves at 6 dBm and

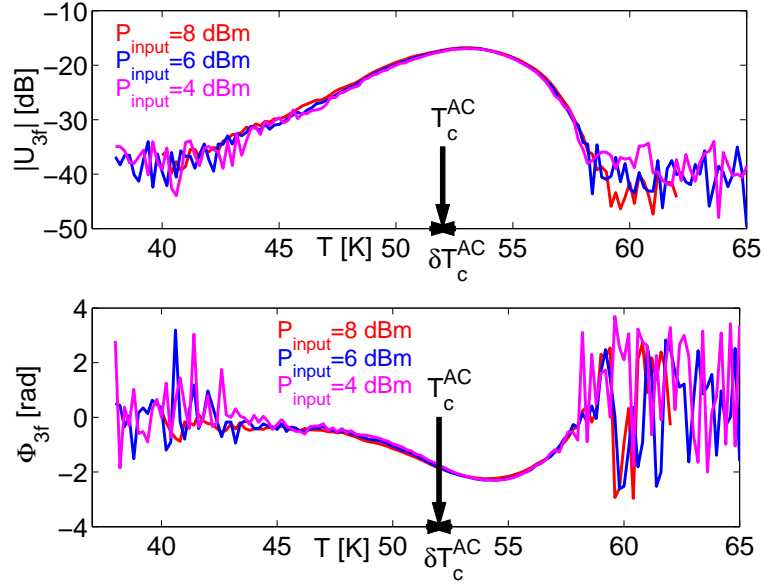


Figure 6.3: Ratioed magnitude and phase of harmonic voltage $U_{3f}(T)$ acquired on a YBCO thin film (STO039) for several values of input power (8, 6 and 4 dBm). The red curve measured with 8 dBm has been considered as reference for both the magnitude and the phase and the other curves, measured for 6 and 4 dBm have been offset by a factor of -2 and -2.7 dB, respectively for magnitude and $+0.07\pi$ and $+0.23\pi$, respectively for phase to obtain a good overlap and examine power-dependent effects.

4 dBm, respectively seem to suggest that lower microwave input power results in higher peaks of ratioed $|U_{3f}^{sample}(T)/U_{3f}^{ref}|$. This fact can be explained as the combined effect of the decrease of the harmonic voltage from the sample $|U_{3f}^{sample}(T)|^\dagger$

[†]Harmonic power measurements performed with the spectrum analyzer on similar YBCO samples and reported in the previous chapter show that the reflected harmonic power from the superconducting sample scales as $|P_{3f}^{sample}| \sim |P_{input}|^3$. Consequently, the scaling in terms of harmonic voltage is $|U_{3f}^{sample}| \sim |U_{input}|^3$.

and that from the reference path $|U_{3f}^{ref}|^\ddagger$. In reality, experimental data from Fig.6.3 show that the temperature range with good signal-to-noise ratio shrinks gradually as the input power is lowered. This suggests that in order to acquire useful data in a larger temperature range, one has to use high input power levels.

The phase data acquired with the various input power levels has also been offset, with the $\Phi_{3f}^{sample}(T) - \Phi_{3f}^{ref}$ acquired at 8 dBm input power serving as reference for the plot. The curves acquired with 6 and 4 dBm have been shifted vertically by an amount of $+0.07\pi$ and $+0.23\pi$, respectively. Since the phase relationship between the input and the harmonic output of the comb generator is unknown, it is impossible to disentangle the contributions of the sample and that of the comb generator in the VNA-FOM measured relative phase. However, as mentioned in Chapter 3, the temperature dependence of the ratioed phase can be entirely attributed to that of the sample $\Phi_{3f}^{sample}(T)$.

The very good overlap of the magnitude and phase data after offsetting the curves at 6 and 4 dBm suggests that the microwave probe does not induce a significant amount of heat in the sample surface since for higher power levels (6 and 8 dBm) there is no obvious shift of the temperature dependences $|U_{3f}(T)|$ and $\Phi_{3f}(T)$ to lower temperatures as would be expected if the sample were heated by the probe.

Common features in the experimental data The first observation regarding all the measured data is that the magnitude of the harmonic voltage exhibits

[‡]The comb generator is being employed outside of its normal operation regime, which is 2 GHz and 0 dBm input. For the measurements reported here, it was used at roughly 6.5 GHz and -14 to -20 dBm, and its input-to-harmonic output relationship is unknown.

a peak, as seen previously in scalar measurements, which occurs at a temperature slightly higher than T_c^{AC} . A novel feature comes from the phase data where a minimum can be noticed at an even higher temperature. The difference of the two temperatures where the extreme values of magnitude and phase occur, $\Delta T_{M,m}$, is doping-dependent: in samples with doping close to the optimal one, $\Delta T_{M,m}$, is small (a few tenths of a Kelvin) but increases as the oxygen content of the thin films is reduced (see $\Delta T_{M,m}$ in Table 6.1). Temperature-dependent data acquired with various input power levels (see for example Fig 6.3) show that $\Delta T_{M,m}$ is power-independent.

The temperature- and doping-dependent harmonic magnitude and phase of $U_{3f}(T)$, as well as their extreme values occurring at different temperatures, could be used as a reliable test for a theory of nonlinear effects in cuprates.

6.3 Analytical treatment of the microwave nonlinear microscope

The objective is to understand quantitatively the features of the measured harmonic voltage (see Fig.6.3), and its general features. For this reason, a finite-frequency modeling of the nonlinear near-field microwave microscope is presented in this section. Traditional models of nonlinear microwave response of superconductors rely on a lumped-element transmission-line approximation. This section presents a new strictly field-based approach that assigns the nonlinearity to fundamental quantities, namely the complex conductivity.

The analytical calculation involves three major steps: first the vector potential created by the loop probe is evaluated at the sample surface followed by the

introduction of nonlinear effects in the real and imaginary parts of the complex conductivity. In the second step, by using a nonlinear generalization of the constitutive London equation for superconductors, the current induced in the sample is evaluated and its harmonic component is identified. In the third step, the vector potential generated by the harmonic current from the sample and its corresponding induced harmonic voltage is calculated at the location of the probe.

The modeling of the nonlinear near-field microwave microscope relies on general electromagnetic theory, and is not restricted to a particular nonlinear mechanism or to the superconducting state. It can be extended, in principle, to any nonlinear physics characteristic of the sample. In the limit of weakly-nonlinear effects, as is revealed by the measured data, and in order to preserve a high level of generality, the nonlinear effects are introduced as phenomenological corrections to the real and imaginary parts of the low-power, linear-response complex conductivity of the sample $\tilde{\sigma} = \sigma_1 - i\sigma_2$. It is shown that the measured harmonic voltage U_{3f} is a complex-valued function that depends on conductivity and the correction coefficients A_1 and A_2 , which quantify the strength of the nonlinear effects in σ_1 and σ_2 , respectively and have units of vector potential.

In order to evaluate the temperature-dependent harmonic voltage $U_{3f}(T)$, one needs a theoretical framework that provides expressions for A_1 and A_2 . In the literature, these quantities have been evaluated analytically only in the particular case of low temperatures $T < T_c$, where $A_1 \rightarrow \infty$ (indicating very small nonlinear effects in σ_1) and A_2 is related to the critical field [93]. In order to model the microwave harmonic response of superconductors, it is necessary to obtain general

expressions for the temperature-dependent nonlinear vector potential scales A_1 and A_2 . Because these scales have never been calculated in the literature, and the difficulty of the problem, the present analysis is restricted to a semi-quantitative level (see also Appendix A for a GL treatment of the $A_{1,2}$ temperature dependence).

In principle any electromagnetics problem can be approached by using the Maxwell equations (or equivalently the wave equations for fields E and H or field potentials A and Φ) and the constitutive relations for the medium under investigation (here, the superconducting thin film). The generalization of the linear-response constitutive relations to the nonlinear case can be obtained from GL, TDGL or BCS.

The Ginzburg-Landau theory provides the appropriate equations for modeling the nonlinear effects especially at temperatures close to T_c where the measurements take place. Since in the Ginzburg-Landau equations the unknowns are the order parameter Ψ and the vector potential A , it is natural to approach the electromagnetic problem in terms of solving the GL equations self-consistently for the vector potential A and the order parameter Ψ . Such an approach can be implemented analytically to model the nonlinear microwave microscope only for some simplified geometries when the dimensionality of the problem can be reduced and the mathematical difficulties associated with solving the partial differential equations for the fields/potentials circumvented.

This section presents analytical results for the simplified geometry shown in Fig. 6.4 in the London gauge ($\nabla \cdot A_f = 0$ with the boundary condition that the probing vector potential at frequency f , A_f , has no component normal to the surface $A_{f\perp} = 0$) [93]. In this treatment the sample has thickness d_0 (smaller than the zero-

temperature penetration depth, $d_0 \ll \lambda_0$) and it extends infinitely in the zOy plane of the Cartesian frame. The assumption of infinite extent in the horizontal plane is accurate since the excitation provided by the microwave probe is very localized and located far from the edges of the thin film. The source of microwave excitation at frequency f is a current wire parallel to the z axis located at $y = 0$ and $x = a$ whose current density is modeled by using the δ Dirac distribution: $j_f^{ext}(x, y) = I_f \delta(x - a) \delta(y)$, as discussed in section §3.3.

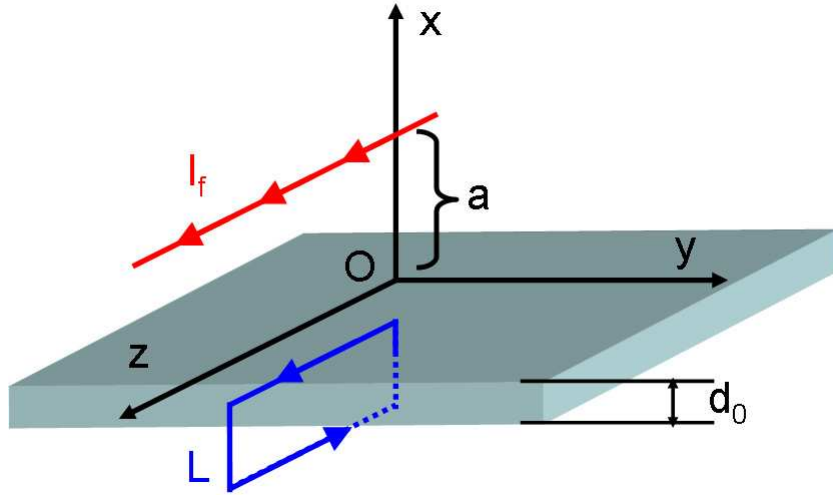


Figure 6.4: Schematic of the model of the near-field microwave microscope: an infinitely thin wire placed at height a above a superconducting slab of thickness d_0 . L is a closed integration contour with the horizontal lines in the top/bottom surfaces of the sample.

Strictly speaking one should solve the wave equation for the vector potential A , which includes a time derivative term $c^{-2} \partial A^2 / \partial^2 t$ (c is the phase velocity in free space), above the superconducting plane. However, since all geometrical dimensions characterizing the system are smaller than the wavelength at microwave frequencies,

the time derivative term can be ignored since the associated time retardation effects are not relevant for the small length scales involved in the problem.

In the subspace $x > 0$, above the superconducting slab, the time-independent version of the wave equation for the vector potential A_f reads:

$$\nabla^2 A_f = -\mu_0 j_f^{ext}, \quad x > 0 \quad (6.1)$$

where the source of A_f is the external current distribution j_f^{ext} . Inside the superconducting slab there is a distribution of screening currents j_{film} , while below the superconducting slab there is assumed to be no current distribution:

$$\nabla^2 A_f = -\mu_0 j_{film}, \quad -d_0 < x < 0 \quad (6.2)$$

$$\nabla^2 A_f = 0, \quad x < -d_0 \quad (6.3)$$

These three elliptic equations must be solved and their solutions and their derivatives with respect to x must be matched at the two boundaries $x = 0$ and $x = -d_0$. An alternative procedure is to "concatenate" the three equations for the three distinct space regions into a single equation as proposed in [93].

Inside the superconducting slab the spatial variation of the vector potential A_f in the x direction is governed by the length scale determined by the inverse of the wave vector introduced in Chapter 2 $|\gamma^{-1}|$ ($\gamma^2 = \lambda^{-2} + 2i\delta_{sk}^{-2}$ which at low temperature $T < T_c$ is governed by the penetration depth λ while in the normal state by the skin depth δ_{sk}). Since the slab is thinner than the penetration depth at $T=0$ K, λ_0 , it can be assumed that A_f and j_{film} do not vary with x . Thus, the Maxwell equation $\nabla \times B = \mu_0 j_{film}$ can be integrated along the closed contour L

having one side above and the opposite one below the superconducting film (see Fig. 6.4):

$$B_{above} - B_{below} = \mu_0 K \quad (6.4)$$

where $B_{above,below}$ represents the magnetic field immediately above and below the superconducting slab, respectively, and $K = d_0 j_{film}$ is the sheet screening current (surface current in units of A/m) flowing through the superconducting slab. Since j_{film} and A_f are related through Eq.(6.2) and $\nabla^2 A_f = \gamma^2 A_f$ (finite-frequency generalization of the London equation, see Chapter 2), Eq.(6.4) can be written:

$$B_{above} - B_{below} = -d_0 \gamma^2 A_f \quad (6.5)$$

Since the fields and currents are uniform within the thickness of the superconducting slab, one can replace the slab with a two-dimensional current sheet and the above three equations for the vector potential (6.1,6.3,6.5) can be written in a closed-form for the entire space[†] [93]:

$$-\nabla^2 A_f(x, y) + \lambda_{eff}^{-1} A_f(x, y) \delta(x) = \mu_0 I_f \delta(x - a) \delta(y) \quad (6.6)$$

where $\lambda_{eff} = 1/(d_0 \gamma^2)$ represents a generalized effective penetration depth.

A similar mathematical approach has been employed to study the electrodynamics of the mixed state in thin superconducting films in the presence of a magnetic field perpendicular to the sample [94].

The propagation constant γ depends on the real and imaginary parts of conductivity (see Eq.(2.11)) which in the general case depend on the external field. In

[†]The author acknowledges useful conversations with Dr. Anatoly Utkin from the Institute of Physics of Microstructures of the Russian Academy of Sciences, Nizhny Novgorod, Russia.

a phenomenological framework, one can assume that nonlinearities can be parameterized as:

$$\sigma_1(T, A) = \sigma_1 \left(1 + \frac{A_f^2}{A_1^2} \right) \quad (6.7)$$

and

$$\sigma_2(T, A) = \sigma_2 \left(1 - \frac{A_f^2}{A_2^2} \right) \quad (6.8)$$

where the nonlinear vector potential scales $A_{1,2}$ have been introduced to quantify the nonlinear effects in the two components (real and imaginary) of the conductivity. These corrections are valid when the excitation A_f is much smaller in magnitude than the nonlinear vector potential scales $A_{1,2}$ ($A_f \ll A_{1,2}$), similar to the phenomenological description of the nonlinear effects from Chapter 5. The approximate equations 6.7,6.8 are not valid at temperatures very close to T_c , where $A_{1,2} \rightarrow 0$. The two equations have been written with the goal of describing **intrinsic** nonlinear effects only: the superfluid density n_S is suppressed by the microwave excitation (i.e. converted into normal fluid), leading to a reduced σ_2 and an enhanced σ_1 . Other nonlinear mechanisms associated with vortex motion, weak links, etc. have been neglected here but can be considered by choosing suitable $A_{1,2}$. If the field dependence of the complex conductivity (as quantified by Eq.6.7,6.8) is taken into account, the propagation constant γ also becomes field-dependent and the equation for the vector potential A_f (6.6) turns into a nonlinear elliptic equation which can not be solved analytically.

Outline of the calculation:

To circumvent the issue of obtaining analytical solutions for a nonlinear elliptic

equation, the problem is solved in three steps, as schematically shown in Fig.6.5: first the nonlinear effects introduced phenomenologically through equations (6.7) and (6.8) are neglected (which corresponds to $A_{1,2} \rightarrow \infty$) and the vector potential A_f and current distribution j_{film} are found by integrating Eq.6.6. It is shown that the current density j_{film} evaluated in the first step of the calculations (in the linear approximation) is mathematically identical to the current distribution induced in a *perfectly* conducting plane by a current distribution $I_f \delta(x - a) \delta(y)$.

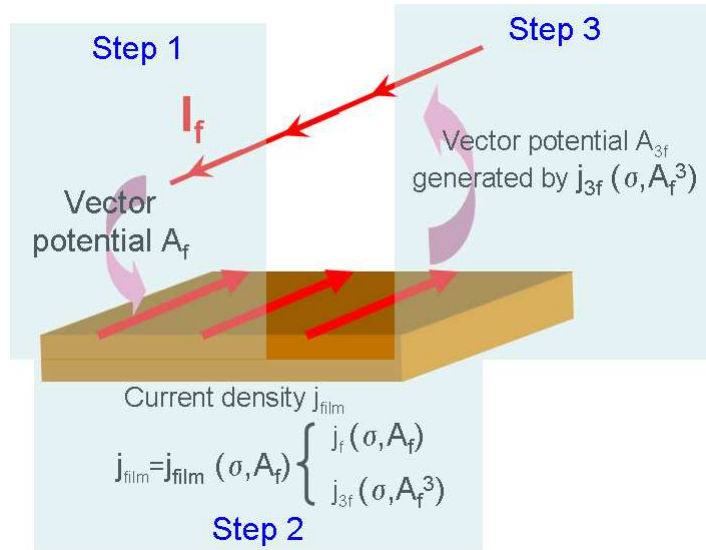


Figure 6.5: Steps in the calculation of the third-order harmonic magnetic vector potential at the location of the emitting/receiving antenna (current wire).

In the second step, a nonlinear generalization of the London equation relating the vector potential and the current density is introduced in order to calculate the current density in the sample at frequency $3f$ originating from the quadratic terms in the equations (6.7) and (6.8). The third step consists in using the reciprocity principle from electromagnetism [95]: the vector potential A_{3f} (whose source is the

current density in the film at frequency $3f$) is evaluated at the location of the wire and from A_{3f} the voltage induced in the wire at frequency $3f$ is obtained.

The full 3D numerical modeling of the microwave nonlinear microscope outlined in Chapter 4 was done in a similar fashion: first, in the linear approximation, the superconducting slab is replaced by a *perfectly* conducting two-dimensional sheet and the current distribution j_{film} produced by the excitation of the loop is evaluated accordingly. In the second step the nonlinear effects are introduced phenomenologically and the voltage induced in the pick-up antenna is evaluated at frequency $3f$.

Step 1: Calculation of the vector potential A_f generated by the excitation current

The partial differential equation for the vector potential (Eq.6.6) can be solved by transforming it into an algebraic equation through the Fourier transform, following the procedure from Ref.[93]:

$$(k_x^2 + k_y^2)A_f(k_x, k_y) + \lambda_{eff}^{-1}A_f(k_y) = \mu_0 I_f \exp(ik_x a) \quad (6.9)$$

This equation can be solved for $A_f(k_x, k_y)$ and integrated with respect to k_x to obtain $A_f(k_y)$:

$$A_f(k_y) = \int_{-\infty}^{+\infty} dk_x \frac{\mu_0 I_f \exp(ik_x a) - \lambda_{eff}^{-1}A_f(k_y)}{k_x^2 + k_y^2} \quad (6.10)$$

The integrals can be evaluated by using the method of complex functions or by using an appropriate software package (Mathematica, for example):

$$A_f(k_y) = \frac{\mu_0 I_f \exp(-|k_y|a)}{2} \frac{1}{|k_y|} - \frac{A_f(k_y)}{2\lambda_{eff}|k_y|} \quad (6.11)$$

which can be solved for $A_f(k_y)$:

$$A_f(k_y) = \mu_0 I_f \frac{\lambda_{eff} \exp(-|k_y|a)}{1 + 2\lambda_{eff}|k_y|} \quad (6.12)$$

This expression must be transformed back into direct space by means of an inverse Fourier transform. However, since there are complications arising from the denominator in Eq.(6.12), it is more convenient to restrict the range of temperatures so that $\lambda \ll a$ (the formalism will not be valid very close to T_c where the penetration depth λ diverges and the perfect screening property of the superconducting film is compromised). In this approximation, the vector potential generated by the current wire reads:

$$A_f(k_y) \approx \mu_0 I_f \lambda_{eff} \exp(-|k_y|a) \quad (6.13)$$

This equation can be inverse Fourier transformed easily and leads to:

$$A_f(y) = -\frac{\mu_0 I_f a}{\pi d_0 (a^2 + y^2)} \cdot \frac{1}{\lambda^{-2} + 2i\delta_{sk}^{-2}} \quad (6.14)$$

where it was taken into account that $\lambda_{eff} = (d_0 \gamma^2)^{-1}$. The corresponding screening current density can be evaluated from the vector potential, but it is not used later since in this formalism the nonlinearity is driven by the vector potential A_f , not the current density j_{film} as in other treatments. It is interesting to note that the screening current distribution $j_{film}(y)$ is mathematically identical to that calculated for a current wire placed above a *perfectly* conducting plane.

Step 2: Calculation of the current density induced in the superconducting film j_{film} and its nonlinear component

The starting point for the analysis of the nonlinear response is phenomenological: the conductivity $\sigma_{1,2}$ depends on the magnetic vector potential A_f and consequently, the relationship between current density j_{film} and the probing field is nonlinear. Usually, in the literature on the nonlinear Meissner effect, it is considered that σ_2 depends on the magnetic field (or induced current density) due to the suppression of the order parameter by the external field. However, taking the vector potential A_f as the perturbing factor simplifies significantly the present mathematical treatment.

In the local London theory the screening superfluid current density j_S depends linearly on the vector potential A_f . At finite frequencies it is not only the superfluid that screens out the external field but also the normal fluid, so the total screening current reads:

$$j_{film} = j_S + j_n = (\sigma_1 - i\sigma_2)E = -\omega(i\sigma_1 + \sigma_2)A_f \quad (6.15)$$

where it was assumed that $E = -\partial A_f / \partial t$ and $A_f \sim \exp(+i\omega t)$ with $\omega = 2\pi f$. Since the real part of conductivity leads to skin depth effects (δ_{sk}) while the imaginary part leads to Meissner screening (λ), one can replace the conductivities $\sigma_{1,2}$ to obtain a finite-frequency generalization of the London constitutive relationship:

$$j_{film} = j_S + j_n = -\frac{1}{\mu_0} \left(\frac{1}{\lambda^2} + \frac{2i}{\delta_{sk}^2} \right) A_f \quad (6.16)$$

In this equation, if the skin depth effects are neglected ($\delta_{sk} \rightarrow \infty$), the London equation is recovered. In order to describe the nonlinear effects in both the real and imaginary parts of conductivity, the low-field conductivities $\sigma_{1,2}$ are replaced

by their nonlinear phenomenological approximations as quantified by equations 6.7 and 6.8. The nonlinear current-to-vector potential relationship can be written as:

$$j_{film} = -\omega\sigma_2 \left(1 - \frac{A_f^2}{A_2^2}\right) A_f - i\omega\sigma_1 \left(1 + \frac{A_f^2}{A_1^2}\right) A_f \quad (6.17)$$

or can be expressed in the more familiar form in terms of the low-power (linear response) length scales λ and δ_{sk} :

$$j_{film} = -\frac{1}{\mu_0\lambda^2} \left(1 - \frac{A_f^2}{A_2^2}\right) A_f - \frac{2i}{\mu_0\delta_{sk}^2} \left(1 + \frac{A_f^2}{A_1^2}\right) A_f \quad (6.18)$$

In the limiting case of neglecting the real part of conductivity and its associated nonlinear effects, one recovers the expression for nonlinear current density used in [93] (with the notation $A_2 = A_c$). The above expression shows that the current density contains a component at frequency f and another component at frequency $3f$ which represents the source of the measured harmonic power at frequency $3f$. The nonlinear component at frequency $3f$ in the total current density j , j^{3f} , can be separated from the A_f^3 terms (real and imaginary) by considering the time dependence $A_f \sim \cos(\omega t)$ and using the trigonometric relation $\cos^3 \omega t = (\cos 3\omega t + 3 \cos \omega t)/4$:

$$j^{3f} = \frac{1}{4\mu_0} \left(\frac{1}{\lambda^2 A_2^2} - \frac{2i}{\delta_{sk}^2 A_1^2} \right) A_f^3 = \frac{\omega}{4} \left(\frac{\sigma_2}{A_2^2} - i \frac{\sigma_1}{A_1^2} \right) A_f^3 \quad (6.19)$$

The total current density at frequency $3f$ in the film can be evaluated by plugging the expression for the vector potential $A_f(y)$ from equation 6.14.

Step 3: Calculation of the induced voltage U_{3f}

This current distribution located on the plane at $x = 0$ and having a $3f$ time variation generates a vector potential A_{3f} in the entire space and induces a voltage in the wire that provided the microwave excitation at the fundamental frequency.

In order to evaluate the induced voltage at the tripled frequency U_{3f} one has to calculate the vector potential at the location of the pick-up antenna (wire). This is accomplished by using the reciprocity theorem from electromagnetism [95] where a current with frequency $3f$ flowing through the wire $j_{3f}^{ext} = I_{3f}\delta(x-a)\delta(y)$ generates the magnetic vector potential on the sample surface given by Eq.(6.14) with the appropriate substitution $f \rightarrow 3f$. Equivalently, a current distribution j^{3f} in the sample given by Eq.(6.19) generates a vector potential $A^{3f}(x, y, z)$ in the entire space. The equivalence principle is written as:

$$\int dV j_{3f}^{ext}(x, y, z) A^{3f}(x, y, z) = \int dV j^{3f}(x, y, z) A_{3f}(x, y, z) \quad (6.20)$$

with the integrals evaluated over the entire space. Since all the $z = \text{constant}$ planes contain the same field and current configuration due to the symmetry of the problem, it will be sufficient to integrate over x and y :

$$\begin{aligned} & \int_{-\infty}^{+\infty} \int_{-\infty}^{+\infty} dx dy I_{3f} \delta(x-a) \delta(y) \cdot A^{3f}(x, y) = \quad (6.21) \\ = & \int_{-\infty}^{+\infty} \int_{-\infty}^{+\infty} dx dy \frac{d_0 \delta(x)}{4\mu_0} \left(\frac{1}{\lambda^2 A_2^2} - \frac{2i}{\delta_{sk}^2(f) A_1^2} \right) \left(-\frac{\mu_0 I_f a}{\pi d_0 (a^2 + y^2)} \cdot \frac{1}{\lambda^{-2} + 2i\delta_{sk}^{-2}(f)} \right)^3 \cdot \\ & \cdot \left(-\frac{\mu_0 I_{3f} a}{\pi d_0 (a^2 + y^2)} \cdot \frac{1}{\lambda^{-2} + 2i\delta_{sk}^{-2}(3f)} \right) \end{aligned}$$

where $\delta_{sk}(f)$ and $\delta_{sk}(3f)$ represent the skin depth evaluated at frequency f and $3f$ respectively. These two length scales do not differ significantly, however, to maintain mathematical consistency they will be treated separately in the following. By using the filtering properties of the Dirac delta function one obtains:

$$\begin{aligned} A^{3f}(a, 0) = & \frac{d_0}{4\mu_0} \left(\frac{1}{\lambda^2 A_2^2} - \frac{2i}{\delta_{sk}^2(f) A_1^2} \right) \left(\frac{\mu_0 a I_f}{\pi d_0 (\lambda^{-2} + 2i\delta_{sk}^{-2}(f))} \right)^3 \cdot \quad (6.22) \\ & \cdot \frac{\mu_0 a}{\pi d_0 (\lambda^{-2} + 2i\delta_{sk}^{-2}(3f))} \int_{-\infty}^{+\infty} \frac{1}{(a^2 + y^2)^4} dy \end{aligned}$$

The final result after integration is the expression for the vector potential at the wire, generated by the $3f$ current distribution located in the plane at $x = 0$:

$$A^{3f}(a, 0) = \frac{5}{64} \left(\frac{\mu_0 I_f}{\pi d_0 a} \right)^3 \left(\frac{1}{\lambda^2 A_2^2} - \frac{2i}{\delta_{sk}^2(f) A_1^2} \right) \left(\frac{1}{\lambda^{-2} + 2i\delta_{sk}^{-2}(f)} \right)^3 \frac{1}{\lambda^{-2} + 2i\delta_{sk}^{-2}(3f)} \quad (6.23)$$

The electric field induced in the wire at frequency $3f$, $E_{3f} = -\partial A^{3f}(a, 0)/\partial t$, is used to evaluate the voltage induced in a probe of length l_0 :

$$U_{3f}(a, 0) = \frac{15\omega l_0}{64} \left(\frac{\mu_0 I_f}{\pi d_0 a} \right)^3 \left(\frac{i}{\lambda^2 A_2^2} + \frac{2}{\delta_{sk}^2(f) A_1^2} \right) \left(\frac{1}{\lambda^{-2} + 2i\delta_{sk}^{-2}(f)} \right)^3 \frac{1}{\lambda^{-2} + 2i\delta_{sk}^{-2}(3f)} \quad (6.24)$$

and the final expression for the induced voltage in terms of length scales can be written:

$$U_{3f}(a, 0) = \frac{15\omega l_0}{64} \cdot \left(\frac{\mu_0 I_f}{\pi d_0 a} \right)^3 \cdot \frac{\lambda^6}{A_1^2} \cdot \left[\frac{2\lambda^2}{\delta_{sk}^2(f)} + i\frac{A_1^2}{A_2^2} \right] \cdot \left[1 + i\frac{2\lambda^2}{\delta_{sk}^2(f)} \right]^{-3} \cdot \left[1 + i\frac{2\lambda^2}{\delta_{sk}^2(3f)} \right]^{-1} \quad (6.25)$$

In terms of conductivities, the induced voltage reads:

$$U_{3f}(a, 0) = \frac{15\omega l_0}{64} \cdot \left(\frac{I_f}{\pi d_0 a \omega} \right)^3 \cdot \frac{1}{\sigma_2^3 A_1^2} \cdot \left[\frac{\sigma_1}{\sigma_2} + i\frac{A_1^2}{A_2^2} \right] \cdot \left[1 + i\frac{\sigma_1}{\sigma_2} \right]^{-4} \quad (6.26)$$

The equations 6.25 and 6.26 have been deduced in an analytical, *field-based* approach as opposed to the model from Chapter 5 and most of the models from the literature where lumped-element approximations are used.

6.4 Discussion and Conclusions

The final equations deduced from the model of the nonlinear near-field microwave microscope for the harmonic voltage, Eq.6.25 and 6.26, show that $U_{3f}(T)$

measured by the sensing wire has a real and an imaginary component. Several dependences must be noted:

1. $|U_{3f}|$ scales with the excitation current as I_f^3 , leading to $|U_{3f}| \sim |U_f|^3$ and similar for power levels $|P_{3f}| \sim |P_f|^3$, in agreement with measurements of power dependence performed with the spectrum analyzer;
2. $|U_{3f}|$ depends on the sample thickness d_0 as $|U_{3f}| \sim d_0^{-3}$ and consequently, the harmonic power $|P_{3f}| \sim d_0^{-6}$, in agreement with the model presented in Chapter 5, suggesting that in order to boost the magnitude of the measured $|U_{3f}|$ or $|P_{3f}|$ thin samples must be used. For this reason, the thinnest samples that can be grown by PLD while maintaining good superconducting qualities, have been used. The dependence on sample thickness could not be checked quantitatively in an experiment since samples of different thickness often have different properties (for example the zero-temperature penetration depth λ_0). In addition, the quality of the samples is not perfectly reproducible from one PLD fabrication process to another. However, qualitatively, it was observed experimentally that thicker samples give a rather small $|P_{3f}|^\dagger$.
3. $|U_{3f}|$ depends on the geometrical separation of probe-to-sample a as $|U_{3f}| \sim a^{-3}$. The probe height with respect to the sample, a , plays a role in the figures of merit Γ and Γ_ρ and the probe-to-sample electromagnetic coupling k

[†]For comparison, a 500 nm thick YBCO film (from Theva, Germany) gives a $|P_{3f}|$ peak about 20 dB above the noise floor, whereas a YBCO 50 nm thick film (XUH163) gives about 40-45 dB measured with the same probe and input power.

introduced and evaluated in Chapter 3. The dependence $|U_{3f}| \sim a^{-3}$ could not be checked experimentally with the current set-up since the vertical resolution of the micrometer controlling the probe-to-sample height is too large and once the probe is not in physical contact with the Teflon sheet, the $|U_{3f}|$ signal is quickly reduced to the noise floor.

Harmonic phase at low temperature: The limiting case of low temperatures $T < T_c$, when the contribution from the normal fluid to the linear response is small ($\lambda/\delta_{sk}(f, 3f) \ll 1$), is worth examining. The expression for the induced voltage Eq.(6.25) can be expanded in a power series in $\lambda/\delta_{sk}(f, 3f) \rightarrow 0$ and the resulting nonlinear response is[†]:

$$U_{3f}^{T \ll T_c}(a, 0) \approx \frac{15\omega l_0}{64} \cdot \left(\frac{\mu_0 I_f}{\pi d_0 a} \right)^3 \cdot \frac{\lambda^6}{A_1^2} \cdot \left[i \frac{A_1^2}{A_2^2} + 2 \left(4 \frac{A_1^2}{A_2^2} + 1 \right) \frac{\lambda^2}{\delta_{sk}^2} - 8i \left(5 \frac{A_1^2}{A_2^2} + 2 \right) \frac{\lambda^4}{\delta_{sk}^4} + \dots \right] \quad (6.27)$$

If only the first term in the above expansion is considered (in the limit of low temperature where the Meissner screening dominates), one obtains a pure inductive response that depends only on the σ_2 nonlinearity, characterized by the nonlinear vector potential scale A_2 :

$$U_{3f}^{T \ll T_c}(a, 0) \approx \frac{15\omega l_0}{64} \cdot \left(\frac{\mu_0 I_f}{\pi d_0 a} \right)^3 \cdot \frac{i\lambda^6}{A_2^2} \quad (6.28)$$

This description of nonlinear response below T_c (see Eq.6.28) is consistent with almost all outstanding treatments of the superconductor nonlinear response [26, 42, 43, 45, 93].

[†]This evaluation was done for the simplifying approximation $\delta_{sk} = \delta_{sk}(f) \approx \delta_{sk}(3f)$

As temperature is increased the ratio λ/δ_{sk} increases and the power expansion of the induced voltage (Eq.6.27) shows that an in-phase component starts to become significant (the second term in square brackets in the expansion) while the out-of-phase component (represented by the first and the third terms in the expansion) is gradually reduced. This prediction (see Eq.6.27) is consistent with the data shown in Fig.6.2 and 6.3, which show that the phase angle rotates clockwise from $\pi/2$ as T_c is approached from below.

Relationship with the previous model: One of the questions that must be addressed at this stage is whether the present formalism that takes into account the effect of the normal fluid on the nonlinear electrodynamics of the superconducting thin films and the nonlinear effects in both the real and imaginary parts of conductivity, can be reduced to the formalism presented in the previous chapter. There, at temperatures below T_c , only the electrodynamics of the superfluid was taken into account: in the language of the model presented here, this is equivalent to enforcing the conditions $\sigma_1 = 0$, $A_1 = \infty$ and $A_2(T) = A_c(T)$, which models the absence of normal fluid and its corresponding nonlinear effects. The harmonic voltage $U_{3f}(T)$ is imaginary, as shown previously when only the first term in the power expansion of $U_{3f}(T)$ was considered in Eq.6.28.

The next step is to cast Eq.6.28 in terms of the nonlinear current density scale $J_{NL}(T)$, used in Chapter 5 to describe the strength of the nonlinear effects. By using the London linear vector potential-current density constitutive equation $J = -A_f/(\mu_0\lambda^2)$, the vector potential is $A_f = -\mu_0\lambda^2 J$. Similarly the nonlinear vector potential scale A_2 can be written in terms of the nonlinear current density

scale introduced in the previous chapter J_{NL} , $A_2 = -\mu_0\lambda^2 J_{NL}$. Thus, the harmonic voltage in terms of J_{NL} reads:

$$|U_{3f}(T)| = \frac{15\mu_0\omega l_0}{32} \left(\frac{I_f}{\pi a d_0} \right)^3 \cdot \frac{\lambda^2}{J_{NL}^2} \quad (6.29)$$

In the previous chapter the power of the third harmonic P_{3f} (see Eq.5.25) was evaluated as $P_{3f} = |U_{3f}|^2/(2Z_0)$ where Z_0 is the characteristic impedance of the coaxial transmission line. In the model from the previous chapter U_{3f} reads:

$$|U_{3f}(T)| = \frac{\mu_0\omega}{4d_0^3} \cdot \frac{\lambda^2}{J_{NL}^2} \cdot \Gamma \quad (6.30)$$

where Γ is the figure of merit characterizing the ability of the microwave probe to induce and to pick up the harmonic response at frequency $3f$. It has to be noted that both expressions for U_{3f} have identical dependencies on the penetration depth λ , nonlinear current scale density J_{NL} , sample thickness d_0 and angular frequency ω . This allows one to identify, from the equivalence of the two formulations, the figure of merit Γ evaluated numerically in the previous chapter in terms of the quantities used in the analytical model of this chapter:

$$\Gamma = \frac{15}{(2\pi)^3} \cdot \frac{I_f^3 l_0}{a^3} \quad (6.31)$$

The units of Γ are $A^3 \cdot m^{-2}$, in agreement with those from Chapter 5.

This limiting case shows that in the limit of low temperatures, where Meissner screening dominates, the model from Chapter 5 is recovered and an equivalence could be established between the figure of merit Γ evaluated numerically for a realistic probe and the geometric distances characterizing the probe-and-sample setup, the probe's height a and length l_0 .

Experimental data and the model: The equation for the harmonic voltage written in terms of conductivity (Eq.6.26) includes the ratios σ_1/σ_2 , A_1^2/A_2^2 , and A_1 , σ_2 whose temperature dependence must be known in order to model the experimental magnitude and phase. Before making any assumptions about a theoretical model for these dependences, it is simpler to restrict the discussion to the phase of the harmonic voltage, which depends only on the ratios σ_1/σ_2 and A_1^2/A_2^2 :

$$U_{3f}(a, 0) \sim \left[\frac{\sigma_1}{\sigma_2} + i \frac{A_1^2}{A_2^2} \right] \cdot \left[1 + i \frac{\sigma_1}{\sigma_2} \right]^{-4} \quad (6.32)$$

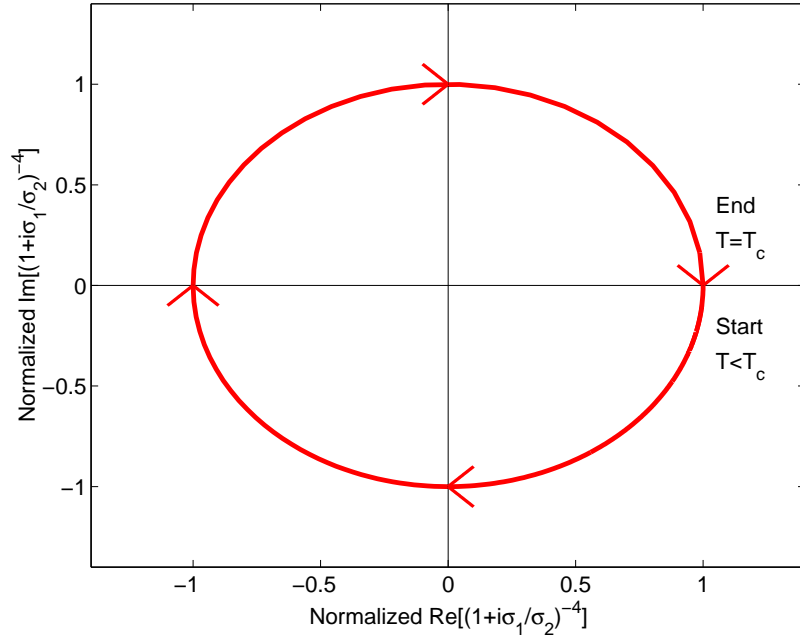


Figure 6.6: The argument of the complex function $(1 + i\sigma_1/\sigma_2)^{-4}$ for the generic model-free temperature dependence of σ_1/σ_2 as the normalized temperature t is varied between 0.8 and 1.

The behavior of the harmonic voltage in the complex plane is governed by the second term in Eq.6.32 due to its 4^{th} power, which is advantageous for a simple analysis since, for superconductors, the ratio of conductivities σ_1/σ_2 has a simple

generic behavior that, in a mean-field approximation, is zero in the superconducting state and diverges at T_c . Consequently, the temperature dependence of the complex argument of the last term $(1 + i\sigma_1/\sigma_2)^{-4}$ can be "guessed": at low temperatures where $\sigma_1 \ll \sigma_2$ the argument of this term is 0. As temperature is increased toward T_c , the argument will execute a full 360 degrees clockwise rotation in the complex plane, as shown in Fig.6.6.

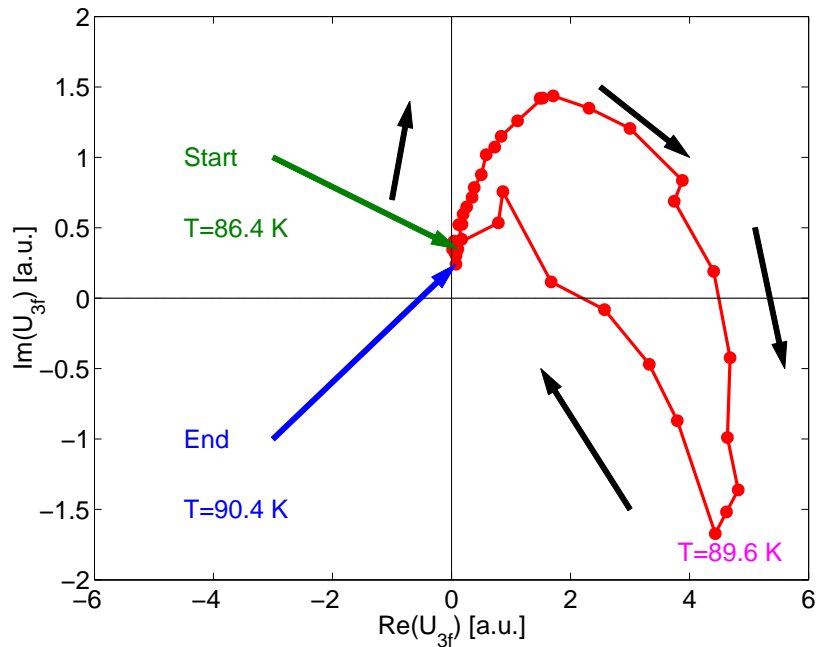


Figure 6.7: Temperature-dependent phase-sensitive harmonic data acquired on a YBCO (XUH157) thin film represented in the complex plane. The arrows indicate the evolution of the complex data as temperature increases from Start($T=86.4$ K) to End($T=90.4$ K). Only the noise-free data are represented here in arbitrary units.

The experimental data shown in Fig.6.2 (see section §6.2) as temperature-dependent magnitude and phase, have been represented in the complex plane as $\text{Re}(U_{3f})$ vs. $\text{Im}(U_{3f})$ in Fig.6.7, after offsetting the phase data to enforce the con-

dition $\Phi_{3f} \approx \pi/2$ at the lowest temperature where the signal-to-noise ratio is good. The experimental data exhibit a non-monotonous behavior of the phase, decreasing from $\pi/2$ at low temperatures (T=68.4 K) until it reaches the minimum (T=89.6 K), then increasing back. This is a general feature of the data acquired with all sample from Table 6.1.

The behavior of data in the complex plane at low temperature, where the phase starts at $\pi/2$ and evolves toward 0, can be accounted for by Eq.6.32 if one assumes that $\sigma_1/\sigma_2 \ll A_1^2/A_2^2$. This is a reasonable assumption and in Appendix A it is shown that within a Drude conductivity formalism:

$$\frac{A_1^2}{A_2^2} = \frac{\sigma_1}{\sigma_2} \cdot \frac{1}{\omega\tau_{qp}} \quad (6.33)$$

where $\omega\tau_{qp} \sim 10^{-3}$ for cuprates at microwave frequencies (τ_{qp} is the quasiparticle scattering time) [15]. Thus, at low temperatures and in conditions of equilibrium between the superfluid and normal fluid, the first term of Eq.6.32 dominates the overall behavior of the harmonic voltage, giving a total phase of $\pi/2$. This is in agreement with the observation that in the conditions of Meissner screening $\lambda/\delta_{sk} \ll 1$, the harmonic voltage is purely imaginary, being dictated by the σ_2 nonlinearity only (see Eq.6.28).

Within the model presented here, the non-monotonous behavior of $U_{3f}(T)$ in the complex plane and the presence of a minimum of phase, suggests that the first complex term in Eq.6.32 should "slow down" the clockwise evolution imposed by the second one and at the temperature where $\Phi_{3f}(T)$ reaches a minimum, (see for example Fig.6.2) it should "reverse" the motion counterclockwise. The first term in

Eq.6.32 cannot compensate and reverse the clockwise rotation of the data, mainly because of the exponent 4 of the second term and its monotonous behavior with temperature in the complex plane.

Consequently, it can be concluded that the model, as formulated, cannot describe the evolution of the phase over the entire temperature range. This is not surprising since the nonlinear effects in $\sigma_{1,2}$, quantified by the nonlinear vector potential scales $A_{1,2}$, have been introduced in a phenomenological fashion (see Eq.6.7 and 6.8)[†] which is invalid at temperatures too close to T_c . Thus, the model could give an estimate of the temperature where the higher-order terms in the power expansion of $\sigma_{1,2}(T, A_f)$, become important.

Additionally, at T_c , other effects may come into play: fluctuations which are detectable in linear-response microwave measurements as a peak of $\sigma_1(T)$, vortex motion, the finite relaxation time of the superconducting order parameter, the possible impact of the cross over from Meissner to skin depth screening on the nonlinear behavior, etc.

To summarize, the model presented in this Chapter has a series of limitations:

1. The microwave loop probe was replaced by a straight current wire and the magnetic vector potential A_f was evaluated in the approximation of a perfectly conducting sample. The problem associated with the field generated by the coaxial loop probe was reduced to the 1D problem of a straight current wire;

[†]Equations 6.7 and 6.8 take into account only the first two terms in an infinite power expansion of $\sigma_{1,2}(T, A_f)$ in $A_f/A_{1,2}$, where the terms $A_f^2/A_{1,2}^2$ are responsible for the third-order harmonic generation effects.

2. The nonlinear elliptic differential equation governing the magnetic vector potential should have been solved self-consistently; but to circumvent the mathematical difficulties, the problem was broken into three steps, where in the first one the nonlinear effects have been neglected;
3. Anisotropy effects in the in-plane conductivity were not considered. Additionally, since the description is phenomenological, the microscopic details (symmetry of the order parameter, shape of the Fermi surface, effects due to the quasiparticles at the nodes of the order parameter, etc.) have been neglected;
4. The nonlinear effects in $\sigma_{1,2}$ have been introduced in a phenomenological fashion by means of nonlinear vector potential scales $A_{1,2}$ and their description is not valid very close to T_c ;
5. The relaxation time of the order parameter was assumed infinitely small, i.e. the order parameter oscillates in phase with the external field. This assumption is valid up to temperatures very close to T_c^\dagger where the present model is invalid anyway due to the phenomenological description of the nonlinear effects in $\sigma_{1,2}$;
6. No extrinsic nonlinear effects were considered (vortex motion, weak links, defects, etc.);

Despite its limitations, the model presented in this chapter offers a qualitative picture of the temperature-dependent harmonic phase $\Phi_{3f}(T)$ at temperatures not

[†]See, for example section §2.3.2 for an estimate of the temperature where these effects become significant.

too close to T_c . The interplay of inductive and resistive nonlinear effects comes naturally in the model, being an improvement with respect to previous models from the literature, which treat the two types of effects separately and incoherently. The mathematical approach is field-based as opposed to lumped-element-based and this allows the introduction of the nonlinear effects as deviations of conductivity from its linear-response values. Unfortunately, due to the lack of theoretical predictions for $A_{1,2}(T)$, the model can only provide a semi-quantitative picture in a limited range of temperatures. However in this range it is in agreement with experimental data.

Chapter 7

Conclusions and future work

The spider weaves the curtains in the palace of the Caesars. †

7.1 Summary

Our nowadays "obsession" with *smaller, faster, more reliable* and *less expensive* cannot be sustained without the availability of investigation tools that have local capabilities. To satisfy this need, various instruments with high spatial resolution have been designed and some of them are already in the inventory of companies and research organizations.

The near-field microwave microscope with magnetic sensitivity has been proposed in 1960's; since then, its range of implementation has widened significantly: only in this dissertation two main projects are presented where *magnetic* materials of interest for the magnetic storage industry and *superconducting* thin films employed in high- T_c superconducting microwave filters are investigated.

The linear near-field microwave microscope proved to be an invaluable tool for the investigation of thin films employed in media for perpendicular magnetic record-

†Attributed to Sultan Mehmed II as he entered the famous St. Sophia cathedral after the fall of Constantinople in 1453.

ing. This is a complicated task for the existing instruments: MOKE microscopy due to its low penetration depth resulting in low signal-to-noise ratio and magnetometers due to the difficulty to generate the necessary radial and circumferential fields.

The nonlinear near-field microwave microscope demonstrated its ability to investigate the fundamental physics of the superconducting state. Its new version with phase-sensitive harmonic detection provides additional information which was not previously accessible and thus, can be used to further test the available theoretical models of cuprates. In the dissertation it is shown that the phase-sensitive abilities allow one to disentangle various types of nonlinear behavior.

7.2 Future work

The linear near-field microwave microscope, presented in Chapter 4 proved to be a powerful tool for the investigation of magnetization dynamics in the soft underlayer of the media employed in perpendicular recording. Three directions of improvement have been identified:

First, the signal-to-noise ratio and the spatial resolution can be enhanced by fabricating more advanced microwave probes with focused-ion beam lithography. Additionally, an accurate positioning tool is necessary to control the probe-to-sample geometrical separation.

Second, in order to investigate the storage layer of the perpendicular media, high DC magnetic fields are required in order to saturate the sample. For this reason, effort must be focused in the direction of designing electromagnets that can

generate high fields (> 1 T) uniform over length scales comparable to those of the microwave probe and integrate them in the current experimental set-up.

Third, the frequency range should be expanded above 25 GHz in order to gain access to the region where the signatures of magnetization dynamics from the storage layer occur.

These efforts have been initiated during the summer of 2006 when I was a summer intern at Seagate Research in Pittsburgh, PA and this project is continued by Nadjib Benatmane under the supervision of Dr. Thomas W. Clinton.

The nonlinear near-field microwave microscopes employed for the investigation of nonlinear effects in cuprate thin films has gone through a series of improvements which culminated with the implementation of a vector network analyzer with harmonic detection capabilities. This major improvement prompted the need for a more advanced model to account for the temperature-dependent harmonic voltage, and especially for the harmonic phase. Most notably, the phase has not been considered in previous models due to the lack of experimental data. In addition, several new types of microwave probes have been designed, fabricated and tested: a thin film probe, various versions of coaxial probes and a novel probe built with an inductive writer from a hard disk drive.

The most important improvement to the current version of the nonlinear microscope is to enhance its overall sensitivity by using a more advanced probe and a more precise positioning system. This would give access to a larger temperature range where nonlinear effects are measurable, especially in underdoped cuprates in the pseudogap regime.

A more advanced microwave circuit could allow the experimenter to vary the input power in a larger range, thus, examining in more detail power-dependent effects. Such effects would be interesting in an artificial grain boundary where theoretical work provides predictions for the power-dependent resistive- and inductive-like nonlinearities.

Obviously, the experimental work with the phase-sensitive nonlinear microscope must go in parallel with a more advanced theoretical model. In the absence of a microscopic approach, the Time-Dependent Ginzburg-Landau theory could be used to deduce the temperature dependence of the two nonlinear vector potential scales $A_{1,2}$ introduced in Chapter 6 to characterize nonlinear effects below and above T_c .

In Chapter 6 it was shown that the nonlinear response, U_{3f} , depends significantly on the low-power, linear response conductivity. Thus, an avenue toward a deeper understanding of the harmonic data is to perform linear-response measurements and extract the quantity of interest, microwave conductivity, which can later be used to "decode" the nonlinear data. Ideally, such a measurement would be performed with the same instrument, only by modifying the room temperature microwave circuit.

7.3 Conclusions

The near-field microwave microscope has been implemented successfully in its linear- and nonlinear response versions to investigate magnetic and superconducting

thin films. The experimental work has been complemented by models, both analytic and numeric that link the measured quantities (complex-valued reflection coefficient and harmonic voltage) with parameters of the samples (anisotropy field, exchange constant, critical current density, lifetime of Cooper pairs in the normal state, penetration depth, etc.). From the experimental data the material characteristics have been extracted and in some cases, compared with independent measurements with good agreement. The range of implementation for the two types of microscopes can be expanded further to investigate new materials and to elucidate the physics of cuprate superconductors.

Appendix A

Temperature dependence of the nonlinear vector potential scales

The model presented in Chapter 6 allows the evaluation of the nonlinear response $U_{3f}(T)$ if the temperature dependence of the nonlinear potential scales $A_{1,2}$ describing the nonlinear effects in the complex conductivity $\tilde{\sigma}$ are known. The model allows one to describe various types of nonlinear mechanisms in superconductors: the nonlinear Meissner effect at low temperature and at T_c , Andreev Bound States, nonlinear effects due to vortex motion, etc. In order to accomplish this goal, one has to evaluate the temperature dependence of the nonlinear vector potential scales $A_{1,2}$ appropriate for the nonlinear mechanism under investigation and that of the low-power, linear-response complex conductivity $\tilde{\sigma}$. To reproduce the microwave harmonic data acquired on cuprate thin films as temperature is swept through T_c one has to derive analytically the temperature dependences for the nonlinear vector potential scales $A_{1,2}$ both in the superconducting and in the normal state.

Ideally, the nonlinear vector potential scales $A_{1,2}$ should be evaluated by using a microscopic theory for cuprates, describing both the superconducting and the normal state. Due to the unavailability of such a theoretical framework, phenomenological approaches remain the only possibility to tackle this problem.

For the superconducting state, the Time-Dependent Ginzburg-Landau (TDGL) would be the most appropriate phenomenological approach, but it poses certain mathematical difficulties. For this reason, the static Ginzburg-Landau theory, valid close to T_c , will be used here since it gives a glimpse into the physics of the nonlinear electrodynamics of superconductors. The major drawback of this approach is that

GL is essentially a zero-frequency theory and some effects related to the finite relaxation time of the order parameter, τ_Δ , are lost. However, in the superconducting state and at microwave frequencies, the order parameter adiabatically follows the external field up to temperatures very close to T_c (see [24, 17]), where its relaxation time becomes comparable to the timescale of the probing signal ($\omega\tau_\Delta \sim 1$). Consequently, the static GL approach is valid in the investigated temperature range except for a very narrow interval at T_c [†].

In the Ginzburg-Landau theory the case of a superconducting film with uniform current density within the thickness can be treated as a one-dimensional problem where the film extends infinitely in the horizontal plane (XOY) with a uniform magnetic field applied on one side. The GL equations for this case, as written in the original GL paper [19], in dimensionless quantities read:

$$\frac{1}{\kappa^2} \cdot \frac{d^2\varphi}{d\xi^2} = -(1 - a^2)\varphi + \varphi^3 \quad (\text{A.1})$$

$$\frac{d^2a}{d\xi^2} = \varphi^2 a \quad (\text{A.2})$$

where $a = A/(\sqrt{2}\mu_0 H_c \lambda)$, $\varphi = (\lambda/\lambda_0)\Psi$, $\xi = z/\lambda$ and κ is the GL parameter. H_c is the critical field, λ and λ_0 are the temperature-dependent penetration depth and its zero-temperature value, respectively. Ψ is the GL order parameter quantifying the "strength" of superconductivity and is related to ratio of the superfluid density n_s to the total carrier density n .

For cuprates $\kappa \approx 100$; in the limiting case of $\kappa \rightarrow \infty$, the above equations can

[†]See for example, section §2.3.2 of this thesis for an estimate of the temperature where GL breaks down in YBCO at microwave frequencies according to the data of Ref.[24]

be solved analytically. The first equation becomes:

$$\varphi^2 = 1 - a^2 \quad (\text{A.3})$$

and shows that the magnetic field a suppresses the order parameter. This equation can be translated back into physical quantities:

$$|\Psi(T, A)|^2 = |\Psi(T, 0)|^2 \left[1 - \left(\frac{A}{\sqrt{2}\mu_0 H_c \lambda} \right)^2 \right] \quad (\text{A.4})$$

where it was considered that the temperature-dependent superfluid density in the presence/absence of a vector potential A is related to the GL order parameter as $n_S(T, A/0) \sim |\Psi(T, A/0)|^2$. Eq.A.4 can be recast in a form to identify the nonlinear vector potential scale A_C that quantifies the suppression of the superfluid density:

$$n_S(T, A) = n_S(T, 0) \left[1 - \left(\frac{A}{A_c} \right)^2 \right] \quad (\text{A.5})$$

with $A_c(t) = \sqrt{2}\mu_0 H_c(t)\lambda(t)$ and $H_c(t)$ the temperature-dependent critical field which in the GL formalism is $H_c(t) = H_c(0)(1 - t^2)$. The dependence (A.5) is similar to the one used in the literature to describe the nonlinear Meissner effect where the perturbation is the magnetic field or the current density.

Once $A_c(t)$ has been determined by using the GL equations and extended to the finite-frequency case, the nonlinear vector potential scales A_1 and A_2 quantifying the strength of the nonlinear effects on conductivity can be evaluated by taking into account that suppression of the superfluid density n_S leads to enhancement of the normal fluid n_n since nominally one would expect $n_S + n_n = n$. One possible avenue to evaluate the temperature dependence of A_1 and A_2 is to use the Drude

conductivity:

$$\sigma_1(T, A) = \frac{n_n(T, A)}{m\omega} e^2 \mathfrak{F}(\omega\tau_{qp}) \quad (\text{A.6})$$

with $\mathfrak{F}(\omega\tau_{qp}) = \omega\tau_{qp}/(1 + (\omega\tau_{qp})^2)$. Next, it is assumed that the nonlinearity in σ_1 comes entirely as a result of the nonlinear superfluid density, and charge conservation, as in the microscopic treatment of Dahm & Scalapino [26]. With $n_n(T, A) = n - n_S(T, A)$ and $n_S(T, A)$ given by Eq. A.4 the real part of conductivity reads:

$$\begin{aligned} \sigma_1(T, A) &= \frac{n_n(T, 0)}{m\omega} e^2 \mathfrak{F}(\omega\tau_{qp}) + \frac{n_S(T, 0)}{m\omega} e^2 \mathfrak{F}(\omega\tau_{qp}) \frac{A^2}{A_c^2} = \\ &= \sigma_1(T, 0) \left[1 + \frac{1}{\sigma_1(T, 0)} \frac{n_S(T, 0)}{m\omega} e^2 \mathfrak{F}(\omega\tau_{qp}) \frac{A^2}{A_c^2} \right] \end{aligned} \quad (\text{A.7})$$

The goal of this calculation is to cast $\sigma_1(T, A)$ in the form:

$$\sigma_1(T, A) = \sigma_1(T, 0) \left[1 + \left(\frac{A}{A_1} \right)^2 \right] \quad (\text{A.8})$$

where A_1 can be written in terms of A_c deduced previously by using $\sigma_1(T, A) = n_n(T, A) e^2 \mathfrak{F}(\omega\tau_{qp}) / (m\omega)$:

$$A_1(T) = A_c(T) \sqrt{\sigma_1(T, 0) \frac{m\omega}{n_S(T, 0) e^2 \mathfrak{F}(\omega\tau_{qp})}} = A_c(T) \sqrt{\frac{n_n(T, 0)}{n_S(T, 0)}} \quad (\text{A.9})$$

Similar calculations can be carried out for $\sigma_2(T, A)$ by using the Drude conductivity where both the superfluid and the normal fluid are taken into account:

$$\sigma_2(T, A) = \frac{n_S(T, A)}{m\omega} e^2 + \frac{n_n(T, A)}{m\omega} e^2 \mathfrak{G}(\omega\tau_{qp}) \quad (\text{A.10})$$

with $\mathfrak{G}(\omega\tau_{qp}) = (\omega\tau_{qp})^2 / (1 + (\omega\tau_{qp})^2)$. Again, it is assumed that the main nonlinearity is in the superfluid density as was the case when A_1 was evaluated. The resulting

imaginary part of conductivity reads:

$$\begin{aligned} \sigma_2(T, A) &= \frac{n_S(T, 0)}{m\omega} e^2 - \frac{n_S(T, 0)}{m\omega} e^2 \frac{A^2}{A_c^2} + \\ &\frac{n_n(T, 0)}{m\omega} e^2 \mathfrak{G}(\omega\tau_{qp}) + \frac{n_S(T, 0)}{m\omega} e^2 \mathfrak{G}(\omega\tau_{qp}) \frac{A^2}{A_c^2} \end{aligned} \quad (\text{A.11})$$

In this equation the first and the third terms make $\sigma_2(T, 0)$:

$$\begin{aligned} \sigma_2(T, A) &= \sigma_2(T, 0) - \frac{n_S(T, 0)}{m\omega} e^2 \frac{A^2}{A_c^2} + \frac{n_S(T, 0)}{m\omega} e^2 \mathfrak{G}(\omega\tau_{qp}) \frac{A^2}{A_c^2} = \\ &= \sigma_2(T, 0) \left[1 - \frac{1}{\sigma_2(T, 0)} \left(\frac{n_S(T, 0)}{m\omega} e^2 - \frac{n_S(T, 0)}{m\omega} e^2 \mathfrak{G}(\omega\tau_{qp}) \right) \frac{A^2}{A_c^2} \right] \end{aligned} \quad (\text{A.12})$$

Finally, $\sigma_2(T, A)$ can be cast in the form:

$$\sigma_2(T, A) = \sigma_2(T, 0) \left[1 - \left(\frac{A}{A_2} \right)^2 \right] \quad (\text{A.13})$$

With the nonlinear vector potential scale A_2 quantifying the nonlinear effects in σ_2 given by:

$$A_2(T) = A_c(T) \sqrt{\sigma_2(T, 0) \frac{m\omega}{n_S(T, 0) e^2} \frac{1}{1 - \mathfrak{G}(\omega\tau_{qp})}} = A_c(T) \sqrt{\frac{1 + \mathfrak{G}(\omega\tau_{qp}) \frac{n_n(T, 0)}{n_S(T, 0)}}{1 - \mathfrak{G}(\omega\tau_{qp})}} \quad (\text{A.14})$$

The imaginary component of conductivity has been written by taking into account both the superfluid and the normal fluid contributions. If the normal fluid is neglected, as is typically done below T_c , the nonlinear vector potential scale A_2 can be obtained by formally replacing $\mathfrak{G}(\omega\tau_{qp}) \rightarrow 0$ and $A_2(t)$ is reduced to $A_c(t)$.

As shown previously, the A_1^2/A_2^2 ratio enters the evaluation of the U_{3f} induced voltage. By using Eq.A.9 and Eq.A.14 deduced in a Drude conductivity framework, the A_1^2/A_2^2 ratio can be expressed in terms of conductivity:

$$\frac{A_1^2}{A_2^2} = \frac{\sigma_1}{\sigma_2} \cdot \frac{1}{\omega\tau_{qp}} \quad (\text{A.15})$$

Appendix B

Attempts to create an absolute nonlinear phase reference

In a phase-sensitive harmonic measurement with the vector network analyzer in frequency-offset mode (VNA-FOM) only the relative harmonic phase can be measured, as discussed in Chapter 3. Ideally, one would like to have a sample whose harmonic response is known accurately for some well-defined temperatures, frequencies and/or microwave power levels (harmonic phase reference). The first step in the experimental procedure would be to measure the harmonic phase reference, then move the microwave probe above the superconducting sample and correct the measured harmonic phase by using information from the measurement of the harmonic phase reference.

Such a procedure could be successful if the harmonic phase reference provided a strong harmonic signal and if its harmonic microwave response could be modeled theoretically. In an attempt to define an absolute harmonic phase reference several samples have been investigated by using the experimental setup for scalar harmonic measurements (with the spectrum analyzer as detector, see section §3.4) to check whether nonlinear effects are measurable: SrTiO₃, GaAs, and a Si wafer. Since the microwave probe couples to the magnetic properties of the samples, the harmonic response of these dielectrics was too small to be detected by the experimental setup. These measurements were inconclusive and for this reason the adjustment of the measured harmonic phase has been done by using the prediction of the model from Chapter 6 at low temperatures where $\lambda/\delta_{sk} \rightarrow 0$ and $\Phi_{3f} \rightarrow \pi/2$.

Appendix C

The coaxial probe and the inductive writer used as a microwave probe

Several attempts have been made to boost the power of 3rd order harmonic effects by designing and building a novel type of microwave probe. One possibility is to deposit a gold thin-film on the cross sectional cut of a coaxial cable then pattern it into a narrow current path. This type of probe has been successfully employed for the measurements reported in Chapter 4, however its design is not robust enough for measurements at low temperatures (77 K and below). For the measurements reported in Chapter 6 the loop created by soldering the inner to the outer conductor has been polished to remove some material, bringing the microwave screening current located at the inner loop radius closer to the sample. This design provides a about 13 dB gain with respect to the coaxial probe used previously in our group [45], as discussed in this dissertation.

An alternative to the coaxial probe used for the near-field harmonic measurements described in this dissertation could be an inductive writer from a hard disk drive where the micro-coil used to read and write magnetic bits on the storage medium in a hard disk drive is used to generate highly-localized high-magnitude magnetic field and pick up the resulting harmonic response. Obviously, the inductive writer of a hard disk drive is not designed to operate at GHz frequencies and at cryogenic temperatures, however its high spatial resolution and high magnetic field could be utilized for near-field microwave harmonic measurements on superconductors.

Experiments with an inductive read/write head have been performed with the experimental set-up for scalar harmonic measurements described in section §3.4 on several samples. Below, in Fig.C.1, an example of such measurements is shown: the sample is a thick (≈ 500 nm) YBCO film fabricated by Theva, Germany, the probing frequency is 6.44 GHz and the microwave input power is -12 dBm. With a regular coaxial probe, a similar dynamic range (about 35 dB between the noise floor and the top of the $P_{3f}(T)$ peak) can be obtained by using $P_{input} = +12$ dBm microwave input power. If it is assumed that the scaling relation $P_{3f} \sim P_{input}^3$ is valid at all temperatures, it can be estimated that the inductive writer provides a $3 \times (12 - -12) = 72$ dB larger $P_{3f}(T)$ peak than the coaxial probe if the input power were + 12 dBm. This estimation suggests that the inductive writer provides an overall sensitivity of about 70 dB more than the coaxial probe.

A number of technical issues must be resolved in order to implement successfully the inductive writer as a near-field microwave antenna for the nonlinear microwave microscope. First the electrical wiring from the coaxial cable to the pins of the writer must be optimized for high frequencies. Second, due to the small dimensions of the writer gap, the distance between the magnetic head and the sample must be controlled very precisely (for the measurements reported here the writer was in contact with the sample). When the temperature dependence of harmonic effects is investigated, one has to make sure that the inductive writer does not alter significantly the local temperature of the sample due to its large thermal inertia; thus temperature ramps must be slow in order to ensure that the temperature read by the thermometer is not very different from that of the sample area where the

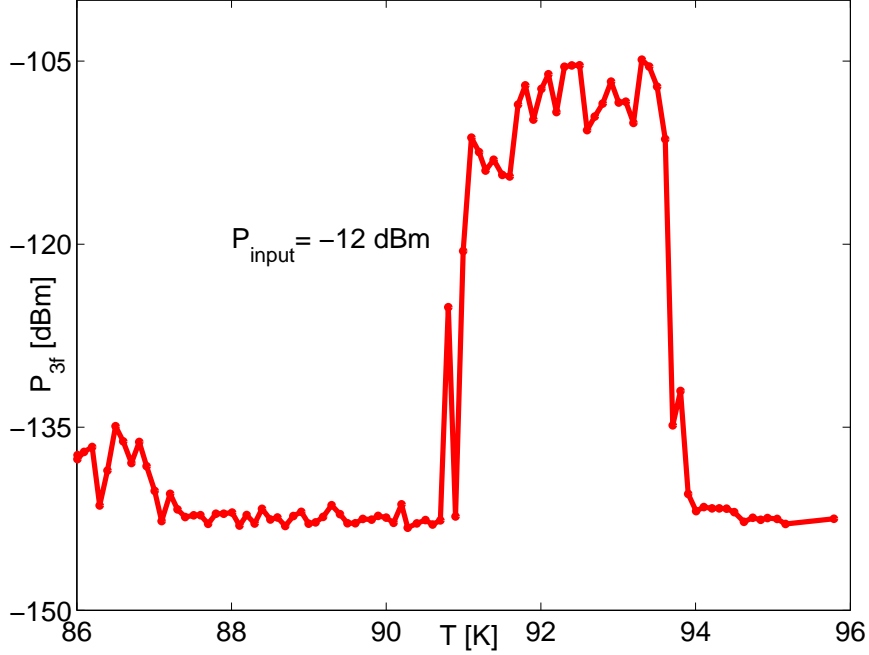


Figure C.1: Example of scalar harmonic data $P_{3f}(T)$ acquired with a superconducting sample with $T_c^{AC} \approx 91$ K and an inductive writer used as microwave probe with an input power $P_{input} = -12$ dBm at frequency $f \approx 6.4$ GHz.

nonlinear response is generated. This is not a serious issue for the coaxial probe since the sample is separated from the probe by a $12 \mu\text{m}$ thick teflon sheet acting as an electrical and thermal insulator. Additionally, the $P_{3f}(T)$ peak in Fig.C.1 exhibits a saturation-like or cut-off behavior which could be explained by considering the suppression of superconductivity close to T_c by the microwave probing field generated by the inductive writer. Also there is concern about the probe magnetic field that might induce vortices in the sample, thus masking intrinsic nonlinear effects.

Due to the complexity of the inductive writer, its implementation as a near-field microwave antenna for the study of nonlinear effects in superconductors requires further experimental investigation.

BIBLIOGRAPHY

- [1] P. W. Anderson, **The theory of superconductivity in the high- T_c cuprates**, Princeton Series in Physics, Princeton University Press, 1997.
- [2] J. R. Waldram, **Superconductivity of metals and cuprates**, Institute of Physics Publishing, (1996).
- [3] D. Manske, **Theory of Unconventional Superconductors. Cooper pairing mediated by spin excitations**, Springer Tracts in Modern Physics, New York, 2004.
- [4] J. L. Tallon, C. Bernhard, H. Shaked, R. L. Hitterman, and J. D. Jorgensen, **Generic superconducting phase behavior in high- T_c cuprates: T_c variation with hole concentration in $\text{YBa}_2\text{Cu}_3\text{O}_{7-\delta}$** , Phys. Rev. B **51**, 12911 (1995).
- [5] Ch. Renner, B. Revaz, J.-Y. Genoud, K. Kadowaki, and Ø. Fisher, **Pseudogap precursor of the superconducting gap in under- and overdoped $\text{Bi}_2\text{Sr}_4\text{CaCu}_2\text{O}_{8+\delta}$** , Phys. Rev. Lett. **80**, 149 (1998).
- [6] V. J. Emery, and S. A. Kivelson, **Importance of phase fluctuations in superconductors with small superfluid density**, Nature (London) **374**, 434 (1995).
- [7] G. Deutscher, **Coherence and single-particle excitations in the high-temperature superconductors**, Nature (London) **397**, 410 (1999).

- [8] I. Ussishkin, and S. L. Sondhi, **On the interpretation of the Nernst effect measurements in the cuprates**, Int. J. of Mod. Physics B **18**, 3315 (2004).
- [9] Y. Wang, L. Li, and N. P. Ong, **Nernst effect in high- T_c superconductors**, Phys. Rev. B **73**, 024510 (2006).
- [10] P. A. Lee, **High-temperature superconductors: Some vortices like it hot**, Nature (London) **406**, 467 (2000).
- [11] S. Tan, and K. Levin, **Nernst effect and anomalous transport in cuprates: a preformed-pair alternative to the vortex scenario**, Phys. Rev. B **69**, 064510 (2004).
- [12] J. Bardeen, L. N. Cooper, and J. R. Schrieffer, **Theory of superconductivity**, Phys. Rev. **108**, 1175 (1957)
- [13] L. N. Cooper, **Bound electron pairs in a degenerate Fermi gas**, Phys. Rev. **104**, 1189 (1956)
- [14] D. C. Mattis and J. Bardeen, **Theory of the anomalous skin effect in normal and superconducting metals**, Phys. Rev. **111**, 412 (1958).
- [15] See for example, M. R. Trunin, and A.A. Golubov, **In-Plane microwave response of high- T_c single crystals: experiment and theory**, in Spectroscopy of High- T_c Superconductors, edited by N. M. Plakida, (Taylor & Francis, 2003); M. R. Trunin, **Conductivity anisotropy and pseudogap in the microwave response of high- T_c superconductors**, Physics-Uspekhi **10**, 1017 (2005).

- [16] I. O. Kulik, **Nonlinear high-frequency properties of thin superconducting films**, Sov. Phys. JETP **30**, 329 (1970).
- [17] O. E-Wohlman, **Third-harmonic generation in dirty superconductors**, Phys. Rev. B **18**, 4762 (1978).
- [18] A. B. Pippard **Field variation of the superconducting penetration depth**, *Proc. Roy. Soc. A* **203**, 210, (1950)
- [19] L. D. Landau and V. L. Ginzburg, originally published in Russian in JETP 20, 1064 (1950); English translation in **Men of Physics: L. D. Landau**, vol. 1, edited by D. Ter Haar, Pergamon Press, Oxford, 1965.
- [20] R. H. Parmenter, **Nonlinear electrodynamics of superconductors with a very small coherence distance**, RCA Review **23**, 323 (1962).
- [21] J. Gittleman, B. Rosenblum, T. E. Seidel, and A. W. Wicklund, **Nonlinear reactance of superconducting films**, Phys. Rev. **137**, A527 (1965).
- [22] A. H. Nethercot, Jr., and J. von Gutfeld, **Nonlinear microwave effects and the switching speed of superconducting tin**, Phys. Rev. **131**, 576 (1963).
- [23] J. C. Amato and W. L. McLean, **Measurement of the Superconducting Order-Parameter Relaxation Time from Harmonic Generation**, Phys. Rev. Lett. **37**, 930 (1976).
- [24] G. I. Leviev, A. V. Rylyakov, and M. R. Trunin, **Relaxation time of the order parameter in YBaCuO single crystal**, JETP Lett. **50**, 88 (1989).

- [25] D. Xu, S. K. Yip, and J. A. Sauls, **Nonlinear Meissner Effect in unconventional superconductors**, Phys. Rev. B **51**, 16233 (1995); S. K. Yip, and J. A. Sauls, **Nonlinear Meissner Effect in CuO Superconductors**, Phys. Rev. Lett. **69**, 2264 (1992); D. Xu, S. K. Yip, and J. A. Sauls, **The Nonlinear Meissner Effect in Unconventional Superconductors**, cond-mat/9502110.
- [26] T. Dahm, and D. J. Scalapino, **Theory of intermodulation in a superconducting microstrip resonator**, J. Appl. Phys. **81**, 2002 (1997); T. Dahm, and D. J. Scalapino, **Nonlinear current response of a d-wave superfluid**, Phys. Rev. B **60**, 13125 (1999).
- [27] E. J. Nicol, and J. P. Carbotte, **Effect of gap suppression by superfluid current on the nonlinear microwave response of d-wave superconductors**, Phys. Rev. B **73**, 174510 (2006).
- [28] A. T. Dorsey, **Linear and nonlinear conductivity of a superconductor near T_c** , Phys. Rev. B **43**, 7575 (1991).
- [29] T. Mishonov, A. Posazhennikova, and J. Indekeu, **Fluctuation conductivity in superconductors in strong electric field**, Phys. Rev. B **65**, 064519 (2002).
- [30] I. Puica, and W. Lang, **Critical fluctuation conductivity in layered superconductors in a strong electric field**, Phys. Rev. B **68**, 054517 (2003).

- [31] G. Benz, S. Wunsch, T. A. Scherer, M. Neuhaus, and W. Jutzi, **Measured temperature dependence of the intermodulation product of coplanar waveguides with s- and d-wave superconductors**, Physica C **356**, 122 (2001).
- [32] D. E. Oates, S. -H. Park, and G. Koren, **Observation of the Nonlinear Meissner Effect in YBCO Thin Films: Evidence for a d-Wave Order Parameter in the Bulk of the Cuprate Superconductors**, Phys. Rev. Lett. **93**, 197001 (2004).
- [33] D. E. Oates, in Microwave Superconductivity, edited by H. Weinstock and M. Nisenoff, (NATO Science Series, 2001), p. 117.
- [34] Elisabeth Nicol (private communication).
- [35] J. Buan, B. P. Stojkovic, N. E. Israeloff, A. M. Goldman, C. C. Huang, and O. T. Valls, **Transverse magnetization study of the pairing state of the high- T_c Superconductor $\text{LuBa}_2\text{Cu}_3\text{O}_{7-\delta}$** , Phys. Rev. Lett. **72**, 2632 (1994).
- [36] A. Bhattacharya, I. Zutic, O. T Valls, and A. M. Goldman, **Angular dependence of the nonlinear transverse magnetic moment of $\text{YBa}_2\text{Cu}_3\text{O}_{6.95}$ in the Meissner state**, Phys. Rev. Lett. **82**, 3132 (1999).
- [37] C. P. Bidinosti, W. N. Hardy, D. A. Bonn, and R. Liang, **Magnetic field dependence of λ in $\text{YBa}_2\text{Cu}_3\text{O}_{6.95}$: Results as a function of temperature and field orientation**, Phys. Rev. Lett. **83**, 3277 (1999).

- [38] K. Halterman, O. T. Valls, and I. Zutic, **Has the nonlinear Meissner effect been observed ?**, cond-mat/0011021; K. Halterman, O. T. Valls, and I. Zutic, **Reanalysis of the magnetic field dependence of the penetration depth: Observation of the nonlinear Meissner effect**, Phys. Rev. B **63**, 180405 (2001).
- [39] M.-R. Li, P. J. Hirschfeld, and P. Wolfe, **Is the nonlinear Meissner effect observable ?**, Phys. Rev. Lett. **81**, 5640 (1998).
- [40] A. Carrington, R. W. Giannetta, J. T. Kim, and J. Giapintzakis **Absence of nonlinear Meissner effect in $\text{YBa}_2\text{Cu}_3\text{O}_{6.95}$** , Phys. Rev. B **59**, R14173 (1999).
- [41] J. C. Booth, L. R. Vale, and R. H. Ono, **On-wafer measurements of nonlinear effects in high temperature superconductors**, IEEE Trans. on Appl. Supercond. **11**, 1387 (2001).
- [42] J. C. Booth, S. A. Schima, and D. C. DeGroot, **Description of the nonlinear behavior of superconductors using a complex conductivity**, IEEE Trans. on Appl. Supercond. **13**, 315 (2003).
- [43] J. C. Booth, K. Leong, S. A. Schima, J. A. Jargon, D. C. DeGroot, and R. Schwall, **Phase-sensitive measurements of nonlinearity in high-temperature superconductor thin films**, IEEE Trans. on Appl. Supercond. **15**, 1000 (2005).

- [44] S.-C. Lee, M. Sullivan, G. R. Ruchti, S. M. Anlage, B. S. Palmer, B. Maiorov, and E. Osquiguil, **Doping-dependent nonlinear Meissner effect and spontaneous currents in high- T_c superconductors**, Phys. Rev. B **71**, 014507 (2005).
- [45] S.-C. Lee, **Measurements of doping-dependent microwave nonlinearities in high-temperature superconductors**, Ph.D. Dissertation, University of Maryland, (2004).
- [46] J. D. Jackson **Classical Electrodynamics**, (Willey, 1999).
- [47] L. P. Gor'kov and G. M. Eliashberg, **Generalization of the Ginzburg-Landau equations for non-stationary problems in the case of alloys with paramagnetic impurities**, Sov. Phys. JETP **27**, 328 (1968); G. M. Eliashberg, **Non-stationary equations for superconductors with low concentration of paramagnetic impurities**, Sov. Phys. JETP **28**, 1298 (1969).
- [48] T. B. Samoilova, **Non-linear microwave effects in thin superconducting films**, Supercond. Sci. Technol. **8**, 259 (1995).
- [49] H. Schmidt, **The onset of superconductivity in the time dependent Ginzburg-Landau theory**, Z. Physik. **216**, 336 (1968); H. Schmidt, **Fluctuations in superconductors below T_c** , Z. Physik. **232**, 443 (1969).
- [50] J. P. Hurault, **Nonlinear effects on the conductivity of a superconductor above its transition temperature**, Phys. Rev. **179**, 494 (1969).

- [51] A. Schmid, **Diamagnetic susceptibility at the transition to the superconducting state**, Phys. Rev. **180**, 527 (1969).
- [52] G. A. Thomas, and R. D. Parks, **Momentum depairing in the paraconductivity regime**, in *Superconductivity, Proceedings of the International Conference on the Science and Technology of Superconductivity*, edited by F. Chilton, (North-Holland, Amsterdam, 1971), p. 215.
- [53] K. Kajimura, N. Mikoshiba, and K. Yamaji, **Nonlinear electrical conductivity of superconducting films below the transition temperature**, Phys. Rev. B **4**, 209 (1970).
- [54] J. R. Tucker, B. I. Halperin, **Onset of superconductivity in one-dimensional systems**, Phys. Rev. B **3**, 3768 (1971).
- [55] T. Mishonov and E. Penev, **Thermodynamics of Gaussian fluctuations and paraconductivity in layered superconductors**, Int. J. of Mod. Phys. **14**(32), 1, (2000).
- [56] V. V. Kurin and A. A. Utkin **High-Frequency Nonlinear Response of Thin Superconducting Films with a Mixed d and s symmetry of the Order Parameter**, *J. of Exp. and Theor. Phys.* **100**, 576 (2005).
- [57] S-C. Lee, and S. M. Anlage, **Spatially-resolved nonlinearity measurements of $\text{YBa}_2\text{Cu}_3\text{O}_{7-\delta}$ bicrystal grain boundaries**, Appl. Phys. Lett. **82**, 1893 (2003).

- [58] S.C. Lee, C.P. Vlahacos, B.J. Feenstra, A. Schwartz, D.E. Steinhauer, F.C. Wellstood, and S.M. Anlage, **Magnetic permeability imaging of metals with a scanning near-field microwave microscope**, Appl. Phys. Lett. **77**, 4404 (2000).
- [59] CST-Microwave Studio, www.cst.com.
- [60] D.I. Mircea and T.W. Clinton, **A near-field microwave probe for local FMR characterization**, Intermag Conference, San Diego, 2006.
- [61] Ansoft High-Frequency Structure Simulator, www.ansoft.com.
- [62] See for example, Agilent Application Note 1408-1, **Mixer transmission measurements using the Frequency Converter application**; Agilent Application Note 1408-3, **Improving measurement and calibration accuracy using the Frequency Converter application**; Agilent Application Note 1408-1, **Amplifier swept-harmonic measurements**.
- [63] See, for example, B. Kuanr, R.E. Camley, and Z. Celinski, **Narrowing of the frequency-linewidth in structured magnetic strips: Experiment and theory**, Appl. Phys. Lett. **87**, 012502 (2005); J.P. Nibarger, R. Lopusnik, and T.J. Silva, **Damping as a function of pulsed field amplitude and bias field in thin film Permalloy**, Appl. Phys. Lett. **82**, 2112 (2003).
- [64] V. Korenivski, R.B. van Dover, P.M. Mankiewich, Z.-X. Ma, A.J. Becker, P.A. Polakos, and V.J. Fratello, **A method to measure the complex perme-**

- ability of thin films at ultra-high frequencies**, IEEE Trans. Mag. **32**, 4905 (1996).
- [65] Y. Ding, T.J. Klemmer, and T.M. Crawford, **A coplanar waveguide permeameter for studying high-frequency properties of soft magnetic materials**, J. Appl. Phys. **96**, 2969 (2004).
- [66] D.I. Mircea and T.W. Clinton, **A near-field microwave probe for local ferromagnetic resonance characterization**, Appl. Phys. Lett. **90**, 142504 (2007).
- [67] See http://www.ssm-inc.com/SSM_Press%20Release.htm
- [68] See, for example, Hewlett Packard Application Note 183, p. 39 (1978).
- [69] S. M. Anlage, V. V. Talanov, and A. R. Schwartz, **Principles of near-field microwave microscopy**, in *Scanning Probe Microscopy: Electrical and Electromechanical Phenomena at the Nanoscale*, edited by S. V. Kalinin and A. Gruverman (Springer-Verlag, New York, 2007), pages 215-253.
- [70] A.L. Sukstanskii and V. Korenivski, **Impedance and surface impedance of ferromagnetic multilayers: the role of exchange interaction**, J. Phys. D: Appl. Phys. **34**, 3337 (2001).
- [71] S. S. Kalarickal, P. Krivosik, M. Wu, C.E. Patton, M. L. Schneider, P. Kabos, T. J. Silva, and J. P. Nibarger, **FMR linewidth in metallic thin films: comparison of measurement techniques**, J. Appl. Phys. **99**, (2006).

- [72] M. Sparks, **Ferromagnetic Relaxation Theory**, (McGraw-Hill 1964).
- [73] C. Kittel, **On the theory of ferromagnetic resonance absorption**, Phys. Rev. **73**, 155 (1948).
- [74] B. Heinrich, J. F. Cochran, and R. Hasegawa, **FMR linebroadening in metals due to the two-magnon scattering**, J. Appl. Phys. **57**, 3690 (1985).
- [75] See for example, S. Y. An, P. Krivosik, M. A. Kraemer, H. M. Olson, A. V. Nazarov, and C. E. Patton, **High power ferromagnetic resonance and spin wave instability processes in permalloy thin films**, J. of Appl. Phys. **96**, 1572 (2001); T. J. Klemmer, K. A. Ellis, and B. van Dover, **Ferromagnetic resonance frequency of a thin Mo-permalloy film**, J. of Appl. Phys. **87**, 5846 (2000).
- [76] See, for example, M. Nisenoff and R.W. Terhune, **Standing spin wave mode spectra in thin permalloy films prepared in vacuum of 10^{-7} Torr**, J. Appl. Phys. **36**, 732 (1965); S.Y. An, P. Krivosik, M.A. Kraemer, H.M. Olson, A.V. Nazarov, and C.E. Patton, **High power ferromagnetic resonance and spin wave instability processes in permalloy thin films**, J. Appl. Phys. **96**, 1572 (2004).
- [77] See, for example, W. P. Jayasekara, J. A. Bain, and M. H. Kryder, High frequency initial permeability of NiFe and FeAl, IEEE Trans on Magn. **34**, 1998; E. P. Valstyn and H. B. Huang, **An extended, dynamic "Transmission-Line" model for thin-film heads**, IEEE Trans. On Magn. **29**, 3870 (1993).

- [78] M. H. Kryder, **Future Materials Research in Data Storage, NSF Workshop on Cyberinfrastructure for Materials Science**, August, 2006, available at http://www.mcc.uiuc.edu/nsf/ciw_2006/talks/Kryder.ppt
- [79] A. Taratorin, **Magnetic Recording Systems and Measurements**, Guzik Tech. Enterpr., (2004), available at http://www.guzik.com/solutions_chapter7.shtml
- [80] T. W. Clinton, Dragos I. Mircea, Nadjib Benatmane, N. J. Gokemeijer, Stella Wu, and S. D. Harkness IV, **A non-destructive, local FMR probe for on-disk media characterization**, Poster, 10th Joint MMM/Intermag Conference, Baltimore, 2007, accepted for publication in IEEE Trans. Mag.
- [81] J. Corson, R. Mallozzi, J. Orenstein, J. N. Eckstein, and I. Bozovic, **Vanishing of phase coherence in underdoped $\text{Bi}_2\text{Sr}_2\text{CaCu}_2\text{O}_{8+\delta}$** , Nature (London) **398**, 221 (1999).
- [82] B. Leridon, A. Defossez, J. Dumont, and J. Lesueur, **Conductivity of underdoped $\text{YBa}_2\text{Cu}_3\text{O}_{7-\delta}$: evidence for incoherent pair correlations in the pseudogap regime**, Phys. Rev. Lett. **87**, 197007 (2001).
- [83] E. Osquiguil, M. Maenhoudt, B. Wuyts, and Y. Bruynseraede Trunin, **Controlled preparation of oxygen deficient $\text{YBa}_2\text{Cu}_3\text{O}_x$ films**, Appl. Phys. Lett. **60**, 1627 (1992).

- [84] B. S. Palmer, H. D. Drew, R. A. Hughes, and J. S. Preston, **Percolative effects in oxygen-depleted $\text{YBa}_2\text{Cu}_3\text{O}_x$ wires**, Phys. Rev. B **70**, 184511 (2004).
- [85] A. Carrington, D. J. C. Walker, A. P. Mackenzie, and J. R. Cooper, **Hall effect and resistivity of oxygen-deficient $\text{YBa}_2\text{Cu}_3\text{O}_{7-\delta}$ thin films**, Phys. Rev. B **48**, 13051 (1993).
- [86] Y. Ando, and K. Segawa, **Magnetoresistance of untwinned $\text{YBa}_2\text{Cu}_3\text{O}_y$ single crystals in a wide range of doping: anomalous hole-doping dependence of the coherence length**, Phys. Rev. Lett. **88**, 167005 (2002).
- [87] W. E. Lawrence, and S. Doniach, **Theory of layer structure superconductors**, in *Proceedings of the Twelfth International Conference on Low-Temperature Physics*, Kyoto, Japan, 1970, edited by E. Kanda, (Keigatu, Tokyo, 1971).
- [88] L. Fruchter, I. Sfar, F. Bouquet, Z. Z. Li, and H. Raffy, **Nonlinear excess conductivity of $\text{Bi}_2\text{Sr}_c\text{Ca}_{n-1}\text{Cu}_n\text{O}_{2n+4+x}$ ($n = 1, 2$) thin films**, Phys. Rev. B **69**, 144511 (2004).
- [89] R. Seto, R. Botet, and H. Kuratsuji, **Excess conductivity in high- T_c superconducting films: role of smooth doping disorder**, Phys. Rev. B **73**, 012508 (2006).

- [90] J. C. Booth, D. H. Wu, S. B. Qadri, E. F. Skelton, M. S. Osofsky, A. Pique, and S. M. Anlage, **Large dynamical fluctuations in the microwave conductivity of $\text{YBa}_2\text{Cu}_3\text{O}_{7-\delta}$ above T_c** , Phys. Rev. Lett. **77**, 4438 (1996).
- [91] A. A. Golubov, M. R. Trunin, S. V. Shulga, D. Wehler, J. Dreibholz, G. Mueller, and H. Piel, **Microwave conductivity of $\text{YBa}_2\text{Cu}_3\text{O}_{6.9}$ single crystals near T_c** , Physica C **213**, 139 (1993).
- [92] J. L. Tallon, and J. W. Loram, **The doping dependence of T^* - what is the real high- T_c phase diagram ?**, Physica C **349**, 53 (2001).
- [93] A. Y. Aladyshkin, A. A. Andronov, E. E. Pestov, Y. N. Nozdrin, V. V. Kurin, A. M. Cucolo, R. Monaco, and M. Boffa, **Study of the nonlinear response of superconductors in the microwave band using a local technique**, Radiophys. and Quantum Electron. **46**, 109 (2003).
- [94] J. Pearl, **Current distribution in superconducting films carrying quantized fluxoids**, Appl. Phys. Lett. **5**, 65 (1964)
- [95] R. E. Collin, **Foundations for microwave engineering**, IEEE Press series on Electromagnetic Wave Theory, New York, 2001.

CURRICULUM VITÆ

Name: Dragos Iulian Mircea

Address: 2001 N Daniel. St., # 101, Arlington, VA, 22201

Title of Dissertation: Measurements of Doping-Dependent Microwave Nonlinear Response in Cuprate Superconductors

Date of Birth: July, 4, 1974

Place of Birth: Suceava, Romania

EDUCATION

PhD in Electrical Engineering, University of Maryland, College Park, MD, June 2007

MS in Physics, "Al. I. Cuza" University, Iassy, Romania, June 2000

BS in Physics, "Al. I. Cuza" University, Iassy, Romania, June 1998

RESEARCH EXPERIENCE:

Summer Intern June – August 2005, 2006
Seagate Research, Pittsburgh, PA

Research Assistant June 2003 – Present
Center for Superconductivity Research, University of Maryland, College Park, MD

Research Assistant Jan. 2001 – June 2003
Laboratory for Physical Sciences, University of Maryland, College Park, MD

Research Assistant Nov 1998 – Oct 1999
Institute for Spectrochemistry and Applied Spectroscopy, Dortmund, Germany

PATENTS, SCOLARSHIPS, AWARDS

US Patent 7,005,849 B2: C. Tse, Charles S. Krafft, I. D. Mayergoyz, D. I. Mircea "High-Speed Massive Data Imaging on a Spin-Stand", awarded "**2002 Invention of the Year Finalist**" in Physical Sciences by the Office of Technology Commercialization, University of Maryland.

University of Maryland Fellowship Jan 2001-Jan 2003.

European Union ERASMUS Scholarship at Institute for Spectrochemistry and Applied Spectroscopy I.S.A.S., Dortmund, Germany, 1998-1999. Awarded to top 5% graduate students at the Department of Physics, "Al. I. Cuza" University Iassy, Romania.

European Union TEMPUS Scholarship at Laboratoire de Physique des Gaz et des Plasmas L.P.G.P., Université de Paris XI, Paris, France, March-May 1997. Awarded to top 3% undergraduate students at the Department of Physics, "Al. I. Cuza" University Iassy, Romania.

Outstanding Senior Student in the Department of Physics, "Al. I. Cuza" University Iassy, Romania 1997. Awarded to top 4% undergraduate students.

PUBLICATIONS

D. I. Mircea, H. Xu, and S. M. Anlage, **Phase-sensitive microwave harmonic measurements in cuprate superconductors**, (in preparation)

D. I. Mircea, T. W. Clinton, **A near-field microwave probe for local ferromagnetic resonance characterization**, *Appl. Phys. Lett.* 90, 142504 (2007).

T. W. Clinton, D. I. Mircea, N. Benatmane, N. J. Gokemeijer, S. Wu, and S. D. Harkness IV, **A non-destructive, local FMR probe for on-disk media characterization**, *accepted for publication in IEEE Trans. Magn.*

D. I. Mircea, S-C Lee, M. C. Sullivan, B. S. Palmer, B. Maiorov, and S. M. Anlage, **Evidence for fluctuation-induced resistive microwave nonlinearities above T_c in underdoped cuprates**, *submitted to Phys. Rev. B*

C. Tse, I. D. Mayergoyz, D. I. Mircea, and C. Krafft, **High-speed massive imaging of hard disk data by using the spin-stand imaging technique**, *J. Appl. Phys.* 93, 6578, (2003)

I. D. Mayergoyz, C. Tse, D. I. Mircea, and C. Krafft, **Scaling of head response function in spin-stand imaging**, *J. Appl. Phys.* 93, 6581 (2003)

P. Andrei, M. Dimian, C. Krafft, I. D. Mayergoyz, D. I. Mircea, and R. Rojas, **Anisotropy characterization of garnet films by using vibrating sample magnetometer measurements**, *J. Appl. Phys.* 93, 7065 (2003)

I. D. Mayergoyz, C. Tse, C. Krafft, D. I. Mircea, and P. Andrei, **Extraction of the response function of GMR head for spin-stand imaging**, *IEEE Trans. Magn* 38, 2453 (2002)

C. Tse, D. I. Mircea, I. D. Mayergoyz, P. Andrei, and C. Krafft, **Spatial and vectorial characterization of thermal relaxation using the spin-stand imaging technique**, *J. Appl. Phys.* 91, 8846 (2002)

M. Göbel, J. D. Sunderkötter, D. I. Mircea, H. Jenett, and M. F. Stroosnijder, **Study of the high-temperature oxidation behavior of Ti and Ti_4Nb with SNMS using tracers**, *Surface and Interface Analysis* 29, 321 (2000)

RECENT CONFERENCE TALKS AND POSTERS

D. I. Mircea, N. Benatmane, N. J. Gokemeijer, T. W. Clinton, S. Wu, and S. D. Harkness IV, **Fabrication and demonstration of a near-field microwave probe for local FMR characterization**, poster at the 51th Joint InterMag-MMM Conference, Baltimore, 2007.

S-C Lee, D. I. Mircea, M. Sullivan, G. Ruchti, S. M. Anlage, B. Palmer, B. Maiorov, and E. Osquiguil, **Measurement of Localized Nonlinear Microwave Response of Superconductors**, Presentation at the APS March Meeting, Los Angeles, 2005.

D. I. Mircea, and S. M. Anlage, **Phase-sensitive measurements of harmonic response in high- T_c superconducting thin films by means of local microwave microscopy** Presentation at the APS March Meeting, Baltimore, 2006.